METAL–ORGANIC FRAMEWORK BASED NON-PRECIOUS METAL ELECTROCATALYSTS FOR THE OXYGEN REDUCTION REACTION

BY

TALHA AL-ZOUBI

DISSERTATION

Submitted in partial fulfillment of the requirements
for the degree of Doctor of Philosophy in Chemical Engineering
in the Graduate College of the
University of Illinois Urbana-Champaign, 2021

Urbana, Illinois

Doctoral Committee:

Professor Hong Yang, Chair
Associate Professor David W. Flaherty
Professor Paul J. A. Kenis
Professor Andrew A. Gewirth

ABSTRACT

Proton-exchange membrane fuel cells (PEMFCs) are devices capable of converting the chemical energy stored in hydrogen into electrical energy for several applications. Their high energy conversion efficiency and environmentally friendly emissions have designated them as viable candidates to replace fossil fuel-based technologies, particularly in transportation applications. However, the high cost associated with the platinum-based catalyst required to drive the sluggish kinetics of the cathodic oxygen reduction reaction (ORR) have rendered these devices impractical on a large scale. To address this, the development of non-platinum group metal (non-PGM) catalysts is a research area of great relevance.

This thesis serves to (1) address the mechanism surrounding non-PGM electrocatalysts and provide a method to understand the structure-property relationship, and (2) study strategies in the synthesis of non-PGM electrocatalyst for greater homogeneity in the as-made active structures.

The first part of this thesis work involves the use of the zeolitic imidazolate framework ZIF-8 as a model precursor to understand the role of temperature on the conversion of metal organic frameworks (MOFs) to an active catalyst. The experimental data together with the DFT calculations suggests that the proximity of carbon-encapsulated neighboring iron structures can play a role in activating surface carbon atoms leading to the cleavage of the OOH bond, a key step in the ORR.

In the second part of this thesis, the use of cadmium as a sacrificial metal instead of the widely-used zinc is presented. The use of cadmium allows for the synthesis of an active non-PGM electrocatalyst at a lower pyrolysis temperature, resulting in an abundance of single atom sites. Furthermore, at a higher pyrolysis temperature, the catalyst synthesized with cadmium as the

sacrificial metal exhibited noteworthy activity in both a three-electrode half-cell test and a membrane electrode assembly (MEA) study.

Lastly, a MOF immobilization strategy is introduced which involved the use of Ketjen black carbon as a support to effectively anchor the MOF precursors prior to thermal treatment. This would allow for a greater dispersion of the single atom metal sites and curb sintering during thermal treatment. It was demonstrated that there was an exclusive formation of single atom iron structures after the pyrolysis using this strategy.

The work in this thesis provides the basis for a fresh outlook on the current work in the area of non-PGM electrocatalysts for the cathodic ORR. Through this work we seek to expand on the understanding of these catalyst materials on a fundamental level and to propose strategies to design and develop highly active catalysts.

ACKNOWLEDGEMENTS

First, I would like to extend my gratitude to my thesis research advisor, Prof. Hong Yang. Not only was Prof. Yang a remarkable teacher, advisor, and guide, his unwavering patience and support throughout my graduate study allowed me to learn and develop as a scientist and contributing team member. As a member of Prof. Yang' research group, I have not only learned of the sacrifice and perseverance needed to conduct quality scientific work but also of the reward in witnessing the impact of scientific findings.

I would also like to thank Prof. Andrew A. Gewirth for the stimulating discussions and guidance on my projects; I was fortunate to have had the opportunity to work with a true expert in the field of electrochemical catalysis.

I also want to thank Prof. David W. Flaherty and Prof. Paul J. A. Kenis for being a part of my thesis committee and on having the opportunity to collaborate with their students. Their feedback and advice have been invaluable in my research.

I also want to take this opportunity to thank Dr. Jaemin Kim who at the time was a postdoctoral researcher in our group. His constructive criticism and engaging presence were greatly appreciated early on in my research.

I would like to also thank Yu Zhou, who was a visiting doctoral student in the Yang Group. His collaborative nature and tireless work ethic gave way to his contributions (material design, synthesis and electrochemical measurement) in Chapter 4 of this thesis.

I am grateful to Prof. Xi Yin (formerly a graduate student in the Yang Group and postdoc at Los Alamos National Laboratory) as his knowledge in the area of non-PGM electrocatalyst design was

instrumental in characterizing the performance of our materials and provided key insight in my research.

My colleagues from the Yang Group including Dr. Kai-Chieh Tsao, Dr. Pei-Chieh Shih, Yiliang Jiang, Wei Gao, Phalgun Madhusudan, Yanling Ma, Andrew N. Kuhn, Cheng Zhang, and Siying Yu are a brilliant group of scientists who have been supportive and provided a cooperative environment to conduct research. I am fortunate to have been a part of this group of individuals and to have shared in their successes.

Over the years I have made the acquaintance of several scientists from different groups at the University of Illinois whom I have had the opportunity to work with and learn from: Dr. Jason A. Varnell, Angela M. DiAscro, Anne M. Esposito, and Christopher Bandas-Rivera (Gewirth Group), Blanka Janicek (Huang Group), Zhongyao Zhang (Flaherty Group), Uzoma Nwabara (Kenis Group).

The University of Illinois campus is home to several facilities and staff scientists who help foster a cutting-edge research experience. I would like to extend my thanks Elizabeth D. Eves and Dr. Kiran Subedi from the SCS Microanalysis Laboratory, Dr. Richard T. Haasch (Materials Research Laboratory), Dr. Danielle L. Gray and Dr. Toby J. Woods (George L. Clark X-Ray Facility and 3M Materials Laboratory).

Aside from our inhouse expertise at Illinois, a portion of my work was contributed to by experts from different institutions including Prof. Charles E. Schulz (Knox College) who carried out all of the Mossbauer spectroscopy analyses, Dr. Chengjun Sun (Argonne National Laboratory) who assisted in X-ray absorption spectroscopy experiments at the Advanced Photon Source (APS), Dr. Piotr Zelenay (Los Alamos National Laboratory) who's leading expertise in non-PGM ORR electrocatalysts was an invaluable resource.

Lastly, I would like to acknowledge the support of my mother and father, their unconditional support gave me the confidence to further my educational goals, my grandparents and aunt, their belief in me gave me the courage to continue despite the numerous obstacles encountered along the path, my siblings, being the eldest in my family came with its fair share of perks and responsibilities and I hope to set an example for them, and my wife without whom this endeavor would have been a fruitless struggle.

TABLE OF CONTENTS

CHAPTER 1

INTRODUCTION

1.1 Introduction to oxygen reduction reaction

Oxygen reduction reaction (ORR) to convert oxygen into water is a central reaction notably in the domains of energy storage and conversion. Among the renewable energy technologies, hydrogen-powered fuel cells are set to take center stage to succeed transitional combustion engines in the future, specifically for transportation applications. The path towards commercialization of these technologies calls for improving the kinetics of the ORR through the development of highly active and cost-effective catalytic materials to enhance performance and drive down costs.[1]

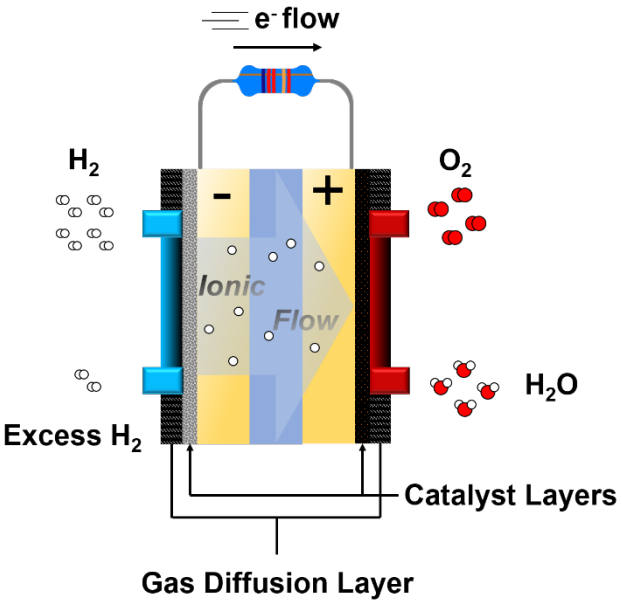

Figure 1.1 Schematic of a proton-exchange membrane fuel cell (PEMFC).

Figure 1.1 depicts a schematic of the layout for PEMFC. At the anode, hydrogen is oxidized into protons and electrons. The protons flow through a proton-conducting medium towards the cathode, while the electrons flow through an outer circuit. At the cathode, oxygen reacts with protons in the presence of electrons to form water. This flow of electrons generates the electricity required to provide power for different applications. Kinetically, the ORR is a sluggish reaction which requires a catalyst to improve the reaction rate by lowering the activation energy barrier. In this respect, there has been an extensive research activity to address this technical challenge. The development of electrocatalytically active materials has witnessed great progress in the past couple of decades.

The theoretical potential at which the electrochemical reduction of oxygen occurs through a $4e^-$ pathway at 25 °C and 1 atm is 1.23 V vs the reversible hydrogen electrode (RHE) is given in equation (1.1).

$$O_2 + 4H^+ + 4e^- \rightarrow 2H_2O \; E^\circ = 1.230\,\text{V} \qquad (1.1)$$

Ideally, in the absence of any kinetic barriers the ORR would be carried out spontaneously at this potential. However, given the natural limitations even in the presence of a catalyst this reaction occurs at a lower potential; the difference between the theoretical potential and actual potential is referred to as the overpotential.

Mechanistically, the ORR in acidic media can proceed through one of two common pathways. The "two-electron pathway" occurs in two steps (each with two electrons): in the first step, hydrogen peroxide (H_2O_2) is formed as the intermediate species, followed by its decomposition into water (H_2O).[2] This mechanism is less efficient for the overall power generation of the PEMFC and can lead to catalyst degradation through a process known as the Fenton reaction.[3, 4] Conversely, water molecules are directly formed through the "four-electron pathway".[5] The $4e^-$ pathway is preferred

for cathode electrocatalysts because of its high utilization of hydrogen and that it occurs at a higher potential.

Researchers have proposed pathways specific on metal surfaces as simple models to investigate the reaction kinetics of ORR.[6-9] The first is known as the dissociative mechanism[6, 10] shown in **Scheme 1.1** and, as the name suggests, is initiated by the cleavage of the oxygen bond upon adsorption onto the catalyst surface. This reaction is then followed by two successive steps where each adsorbed oxygen atom reacts with a proton and electron to from water which then desorbs from the catalyst surface. This mechanism follows the $4e^-$ pathway because four electrons are required for the desorption of a product and no H_2O_2 intermediate is formed during the process.

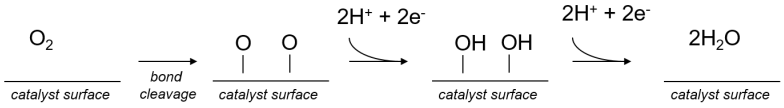

Scheme 1.1 The proposed *dissociative* ORR step-by-step mechanism on metal surfaces.

The second known as the associative mechanism[6, 10] illustrated in **Scheme 1.2** proceeds through an adsorption of the oxygen molecule on the catalyst surface followed by hydrogenation and a cleavage of the oxygen-oxygen bond. In contrast to the dissociative mechanism, during the associative mechanism the oxygen-oxygen bond cleavage occurs after the first hydrogenation step rather than upon adsorption onto the catalyst surface.

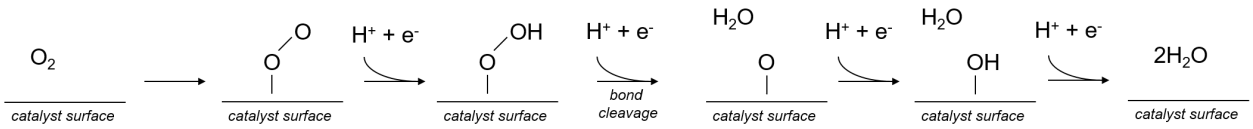

Scheme 1.2 The proposed *associative* ORR step-by-step mechanism on metal surfaces.

The differences between the associative and dissociative mechanisms affect the reaction barriers for ORR. The stabilization of reaction intermediates on catalyst sites influences these pathways which ultimately affects the measured reactivity of metal surfaces towards the ORR.[11] Characteristic descriptors are one such way to identify the properties that govern catalytic behavior. These reaction parameters can be investigated experimentally or computationally to determine the relevant descriptors which help guide research in this area. As shown in **Figure 1.2**, the binding energy values of O* (ΔE_O) and OH* (ΔE_{OH}) were used as descriptors to identify activity trends among transition metal catalysts.[6]

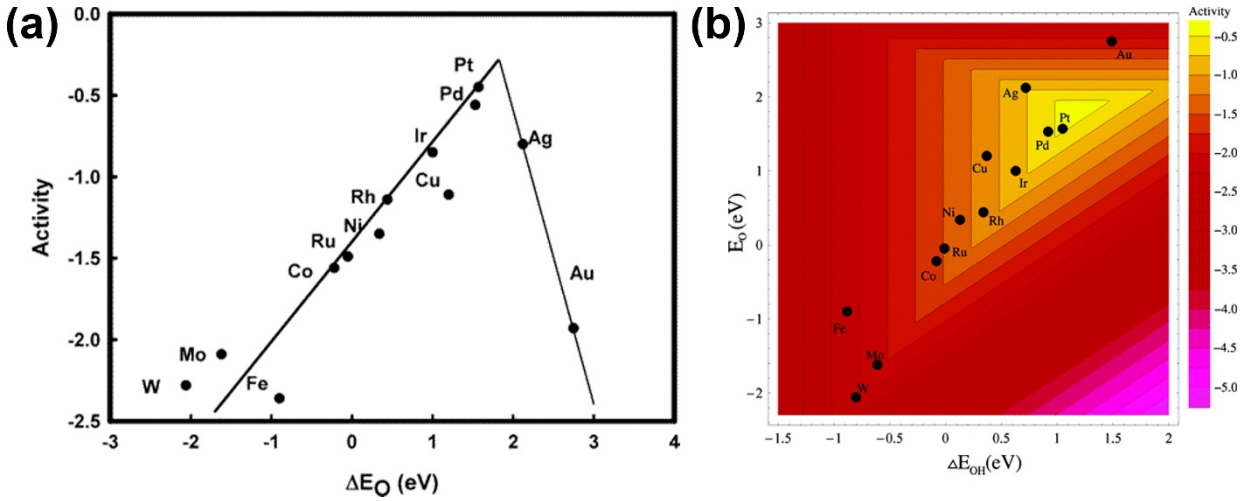

Figure 1.2 (a) Plot exhibiting the oxygen reduction activity of various metal catalysts as a function of the O binding energy.[6] (b) Plot exhibiting the oxygen reduction activity of various metal catalysts as a function of both the O and OH binding energy.[6]

In accordance with the Sabatier principle, metals with weak O* binding energy (e.g. gold) cannot effectively promote oxygen-oxygen bond scission thus favoring the partial reduction of oxygen to hydrogen peroxide. In contrast, metals with a strong affinity to oxygen (e.g. nickel, copper) would simply become oxidized leading to their deactivation.[10] Thus, the most active metals for electrochemical reduction of oxygen are characterized by their intermediate O* affinities, as demonstrated by the platinum metal. Near the theoretical potential of ORR, adsorbed O* increases in stability on the surface of platinum. By lowering the potential, this bond stability decreased, thus driving the reaction forward. These fundamental concepts also offer a theoretical basis for platinum-metal alloying to further influence the stability of intermediates and modify the reaction kinetics. It was found that the addition of a secondary subsurface layer of a non-noble metal such as nickel could lead to a down-shift of the d-band center of the platinum surface layer and result in a weakening of the binding of chemical species to the (111) surface; in addition, the subsurface

layer can modify the heat of reaction and activation energies of the different elementary reactions of the ORR on the (111) surface.[12]

1.2 State-of-the-art electrocatalysts for the oxygen reduction reaction

The search for materials to serve as cathode catalysts for the ORR has led to the identification of several key benchmarks that must be met.[13] The first is catalyst activity which is defined as the catalyst's ability to bind oxygen strongly enough such that the reaction can take place; however, if too strong, the catalyst will become oxidized and not be capable of catalyzing the reaction. The next criterion is the catalyst must be selective towards the formation of water rather than hydrogen peroxide which would entail promoting the $4e^-$ pathway. This implies a mechanistically robust catalyst which is tailored to favor a specific reaction pathway. The third is catalyst stability/resistivity; the operating environment of a PEMFC includes a low pH and the possibility of certain contaminants leading to an irreversible deactivation of a catalyst; a catalyst should be able to withstand harsh reaction conditions and perform effectively for long periods of time.

In this regard, precious metals, in particular platinum, have been shown to be prime candidates for PEMFC cathode catalysts for the ORR.[14, 15] However, given the high-cost of platinum and its susceptibility to deactivation through poisoning by carbon monoxide along with a desire to push the limits on catalytic performance researchers have looked at alloying platinum with transition metals as a means of addressing the stated issues.[16-18] This has led to the development of a number of such bimetallic catalysts including platinum-cobalt and platinum-nickel alloys among others.[19, 20]

In the same vein there has been a shift towards the complete elimination of precious metals through the development of non-precious group metal (non-PGM) electrocatalysts which has gained wider traction in recent years.[21-25]

1.3 Current developments in non-PGM electrocatalysts

Cobalt phthalocyanine was first found to catalyze the ORR and it was proposed that the active site consisted of the CoN_4 moieties within the catalyst.[26] This ushered in the development of a new class of electrocatalysts known as non-PGM electrocatalysts. Since then several nitrogen-doped carbon-derived electrocatalysts with iron, manganese or tin have been shown to be active towards the ORR.[23, 27, 28] Although promising, this category of catalysts presents its fair share of challenges that must be addressed by researchers as outlined below.

- Activity: Non-PGM electrocatalysts have not yet to outperform some of the best PGM-based electrocatalysts.

- Stability: Issues relating to the peroxide-induced Fenton reaction which leads to a destabilization of iron-based electrocatalysts can be mitigated by relying on alternative metals.[3] However, carbon oxidation at high potentials remains a challenge as this can potentially lead to a decomposition of active sites within the electrocatalyst.[29, 30]

- Clarity surrounding active structures: Non-PGM electrocatalysts are highly heterogenous containing multiple structures and including several different elements. This has led to ambiguity regarding which structures are active towards the ORR.

1.3.1 Chemical breakdown of non-PGM electrocatalysts

The chemical makeup of most non-PGM electrocatalysts consists of carbon, nitrogen, and an active metal, such as iron, cobalt, and manganese.[31] The structural and chemical properties of these catalyst materials play critical roles in the resulting activity and stability for the ORR. These parameters are largely determined by the synthetic pathway, often involving high temperature pyrolysis to generate the active moieties needed to facilitate the reaction. The synthetic protocol typically involves the mixing of different precursors either followed by pyrolysis under Ar or NH_3 to produce the final catalyst. The major component in non-PGM electrocatalysts is carbon followed by nitrogen with a transition metal with an atomic composition of <1 to 3 percent. As mentioned earlier, non-PGM electrocatalysts are highly heterogeneous and can contain bulk structures including metal nitrides, -carbides, -oxides, and reduced metal.[32-36] More importantly, they also host single-atom metal-nitrogen sites which have been asserted to be highly active towards the ORR. Structurally, these materials are high-surface area typically exceeding 300 m^2 g^{-1} based on the Brunauer-Emmet-Teller (BET) analysis and are often hydrophobic given the substantial amount of carbon. Differences in performance are related to the types of iron structures, local binding of nitrogen, crystallinity of carbon, and the physical properties of the material (porosity, active surface area).[25]

1.3.2 The influence of the metal center on non-PGM electrocatalysts

The question regarding the role of the metal in non-PGM electrocatalysts has been one of significance. Extensive research has been done around *metal-free* electrocatalysts which have been shown to be active towards the ORR under basic conditions.[2, 37] This has called into question the necessity of including a transition metal during the synthesis of non-PGM electrocatalysts. Reports

have asserted that while the addition of a metal precursor during synthesis is necessary to generate an active non-PGM electrocatalyst, its role is limited to catalyzing the formation of active structures.[38, 39] Yet, other reports have expressed the function of the metal as an integral part of the active structure of the electrocatalyst whether as a single-atom coordinated by nitrogen or in bulk structures.[23] This ambiguity has led to the use acid-washing treatments to selectively remove metal structures and compare the activity before and after; however, results are varied with some catalysts exhibiting an increase in activity following acid treatment while others exhibit a loss in activity.[40-44] What can be agreed upon is that the inclusion of the metal contributes to the activity observed in non-PGM electrocatalysts.

1.3.3 Characterization methods for non-PGM electrocatalysts

Given that carbon makes up the bulk of non-PGM electrocatalysts with a sparse amount of metal, material characterization of metal-nitrogen-carbon structures can be challenging. Morphologically, non-PGM electrocatalysts are overarchingly amorphous materials with a variety of heterogeneous structures ranging from atomic scale sites to microscale crystalline formations. This has rendered characterization using conventional techniques such as powder X-ray diffraction (PXRD) and transmission electron microscopy (TEM) inadequate in obtaining a thorough picture of the chemical and morphological structure of the material. Instead, researchers have turned to tools including scanning transmission electron microscopy (STEM), Mossbauer spectroscopy and Raman spectroscopy to elucidate the chemical, physical, and electronic properties of their catalysts. Below is a compilation of techniques used in investigating non-PGM electrocatalysts.

X-ray photoelectron spectroscopy (XPS): XPS operates on the principle of the photoelectric effect. An aluminum source emits monochromatic X-rays that impinge upon a sample in a vacuum

chamber. If the photon energy of the X-rays exceeds the binding energy of the valence electrons within the sample, the target electrons will become excited and leave with a kinetic energy in accordance with equation (1.2).

$$E_{\text{binding}} = E_{\text{photon}} - (E_{\text{kinetic}} + \phi) \qquad (1.2)$$

Here, E_{binding} refers to the binding energy of the electron of the element under investigation. E_{photon} is the energy of the impinging photon. E_{kinetic} is the kinetic energy of the emitted electron and ϕ refers to the work function which is dependent on the material surface. Given that XPS relies on emitted electrons reaching a detector, this limits its application to surface studies and makes it less effective for bulk material investigations.

In the case of non-PGM electrocatalysts, XPS is typically used to characterize the valence states of nitrogen.[45-49] This is especially useful in understand the kinds of nitrogen binding with carbon. Due to the relatively low amount of metal within the catalyst material, XPS becomes less effective in elucidating their valence states.

Mössbauer spectroscopy: Mössbauer spectroscopy is a powerful technique when examining *Mössbauer-active* elements (i.e. Fe) within chemical samples. The Mössbauer effect[50] relies upon the conservation of momentum. The species under study must be able absorb and emit gamma rays from a source without recoil. This requires that the elemental species of the sample be fixed within a lattice such that there is no loss of energy due to recoil upon absorption of the gamma rays. Experimentally, gamma-rays from a radioactive material are impinged upon a sample and the intensity of the reemitted gamma rays are measured by a detector. It is key that the atoms in the gamma ray-emitting source be of the same elemental isotope as the atoms in the absorbing sample; this places a limitation on which elements can be characterized using this technique. The energy

of the emitted gamma rays can be varied by accelerating the source which would lead to a Doppler effect. This technique is sensitive to the hyperfine interactions in the bonding environment of the iron species and can detect differences between them accurately. Differences in the energy between atoms in the emitting source and the atoms in the sample under investigation result in chemical shifts or isomeric shifts. These isomeric shifts are characteristic of certain species and can be used to fingerprint discern the presence of particular species based on prior data.

Given that iron is a Mössbauer-active element, this technique is widely used in investigating the chemical environments of iron-containing non-PGM electrocatalysts.[51] Using this method, several iron structures have been identified in non-PGM electrocatalysts, among them single-atom iron structures, iron -nitrides and carbides, and reduced iron structures of varying phases.[34, 44, 52-57]

Vibrating-sample magnetometry (VSM): An additional technique useful in distinguishing between the structures of iron based on their magnetic properties is VSM. A magnetic field is imposed upon a sample meanwhile the sample is fluctuated which induces a voltage. The induced voltage is measured using a pickup coil which corresponds to the magnetic moment of the material. Typically, experiments can involve a sweep of varying magnetic field strengths and measure the magnetizations induced in the material. In conjunction with Mössbauer spectroscopy, VSM reveals the presence of para- and ferromagnetic species within non-PGM electrocatalysts.[34]

Scanning transmission electron microscopy (STEM): Like all microcopy techniques, STEM gives visual information of the catalyst morphology and size. STEM uses operating voltages of typically 300 kV compared to the conventional TEM operating voltage of ~200 kV. The electron beam is focused and swept over a specific area rather than having the entire sample exposed to the electron beam. Additionally, the magnification and resolution allow atomic-level information such as

observing single-atom structures. This technique is usually coupled with electron-dispersive X-ray (EDX) and electron energy loss spectroscopy (EELS) to investigate elemental distribution throughout the material at the nanoscale.

Non-PGM electrocatalysts generally requires high-resolution images of single-atom metal structures with elemental analysis.[27, 58-62] The observation of these structures across a variety of different non-PGM electrocatalyst has led many researchers to conclude that these structures are active towards the ORR.

Raman spectroscopy: Despite composing the majority of non-PGM electrocatalysts, carbon remains the difficult to characterize. This in part due to its the pervading presence of carbon in air to the general tools being used in material investigation. This poses a challenge in deciphering the carbon in non-PGM electrocatalysts from the carbon deposited on the surface of materials otherwise known as adventitious carbon[63, 64] and renders surface sensitive techniques such as XPS ineffective.

Raman spectroscopy affords an alternative approach to investigating the carbon structure in non-PGM electrocatalysts by using inelastic light scattering. Monochromatic light from a laser is impinged upon the sample and interacts with the molecular vibrations causing the light to scatter which is then collected onto a detector. Differences between the impinging light and the reflected light result in a Raman shift which gives information on the properties of the material. Specific to non-PGM electrocatalysts, the graphitic nature of carbon is observed by the Raman shifts in the range of 1250 cm^{-1} to 2250 cm^{-1}.[65, 66] The relative ratio of the D to G band reflects the ratio of disordered carbon (D) to crystalline carbon (G).[59]

X-ray absorption spectroscopy (XAS): Similar to XPS, XAS operates on the basis of core electron excitation to obtain information about the valence state and chemical environment. In the case of XAS, the relative absorption of X-rays is analyzed in contrast to the kinetic energy of the emitted electron.[67] XAS is carried out at a synchrotron where a high-intensity X-ray beam generated through electron acceleration in a particle accelerator. These X-rays are impinged upon a sample and depending on their energy and the sample composition pass through and are absorbed by the sample; changes in the X-ray energy are measured by a detector. These changes are described by the Lambert-Beer law in equation (1.3) which is used to describe the attenuation of X-rays:

$$\frac{I}{I_0} = e^{-\mu_{lin} z} \quad (1.3)$$

Here, the ratio of I to I_0 is the ratio of the emergent X-rays to the incident X-rays. On the other side of the equation, μ_{lin} is the linear absorption coefficient which is dependent on both the X-ray energy and the material under investigation and z refers to the distance traveled by the X-ray, which in this case reflects the thickness of the sample under study. The energy of the emitted X-rays is characteristic of the chemical environment of the material.

X-ray absorption near edge spectroscopy (XANES): When the energy of the incident X-rays is equal to the binding energy of the core electrons of the species under study, it can excite the core electron into the continuum which leads to the rise of an *edge*. This region is particularly useful in analyzing and comparing the oxidations states of samples with respect to a reference.

Extended X-ray absorption fine structure (EXAFS): Shortly beyond the edge region oscillatory features are observed; these oscillations are caused by the excited electron's interactions with

neighboring atoms. This region provides valuable information relating to the bonding nature and coordination of the absorbing atom.

Given that the atomic concentration of metals is relatively low in non-PGM electrocatalyst as stated earlier, XAS has proven to be a powerful technique to understand the valence and coordination structure for single-atom metal sites in non-PGM electrocatalysts.[23, 34] However, XAS remains a bulk technique which can be disadvantageous for non-homogenous materials.

1.3.4 Suggested active structures in non-PGM electrocatalysts

There have several claims as to which structures present in non-PGM electrocatalysts leads to the activity observed towards the ORR in acidic media. As shown in **Figure 1.3**, some of the more common structures claimed to serve as the active component in non-PGM electrocatalysts are nitrogen-carbon[4], FeN_x/FeN_4[23, 36, 44, 56, 68-71] and CoN_x/CoN_4[62, 72, 73] single atom sites, $Fe_3C@C$[35, 74], and reduced iron nanoparticles[34, 75]. Although uncertainty exists around the structure of the active site responsible for the ORR in non-PGM electrocatalysts, the general consensus is that FeN_4 structures give rise to the activity observed within those catalysts. Supporting evidence comes from biology, where FeN_4 moieties in hemoglobin are found to be responsible for the capture and dissociation of oxygen in the blood.[76]

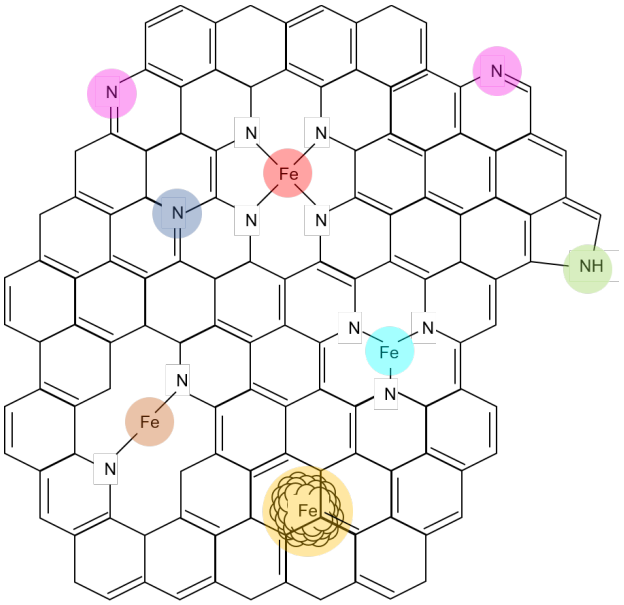

Figure 1.3 Suggested active structures of in non-PGM electrocatalysts including nitrogen and iron-based sites: pyridinic nitrogen (purple), pyrrolic nitrogen (green), graphitic nitrogen (blue), FeN_4 (red), FeN_3 (teal), FeN_2 (brown), reduced Fe (yellow).

Various experiments use probe molecules including carbon monoxide[77], cyanide anions[78, 79], and hydrogen sulfide[80] to investigate their impact on catalytic performance in RDE measurements. Another group investigated the impact of fluorination on the performance of a non-PGM electrode catalyst in a membrane electrode assembly.[81] The underlying assumption in these research efforts is that the probe molecule adsorb selectively to a specific site (in this case single atom FeN_x/FeN_4). Observing a reduction in the ORR performance suggests that the probe molecule inhibits the activation of oxygen at these sites. These studies conclude that single-atom sites play a key part in the reactivity of non-PGM ORR electrocatalysts.[82]

In this context, producing a high density of single-atom sites (metal atom bound to carbon or nitrogen atoms) has received much attention.[59, 83-86] Formation of these species has been shown to result in a high catalytic ORR activity in addition to high metal efficiency. Currently, the most

active non-PGM electrocatalysts for the ORR are composed of single-atom iron as the active structure.[87-89]

1.4 Synthetic pathways towards non-PGM electrocatalysts

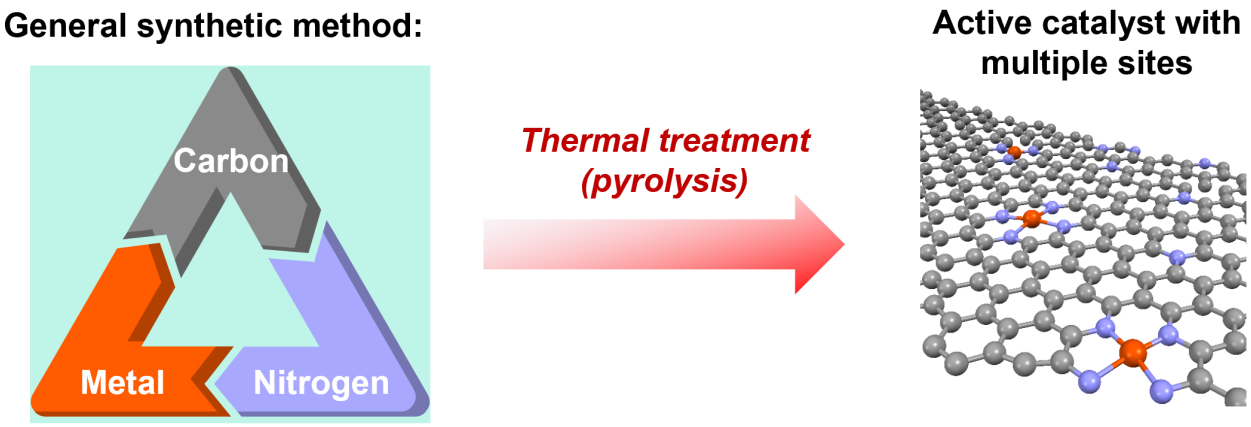

Figure 1.4 Schematic of a typical process to synthesize non-PGM electrocatalysts.

As mentioned, the composition of non-PGM electrocatalysts include carbon, nitrogen, and a metal. One demonstrated synthesis approach is to combine individual precursors of each elements, either in the solid phase or in a solvent, followed by thermal treatment to obtain the final catalyst (**Figure 1.4**). This approach known as the multiple precursor method and is the most widely used approach to obtaining active electrocatalysts.[56, 68, 69, 90, 91] However, this synthesis method may not lead uniform structures within the sample, some of which are inactive for the target reaction.[35, 36, 44, 92] The inability to form homogenous materials raises two research challenges: identification of the active structure and the development of synthesis strategies towards the preferred structure in these electrocatalysts.[25] This has inspired researchers to assess and improve on current synthesis models and develop methodologies to maintain structural and morphological homogeneity, despite the

harsh synthetic conditions non-PGM electrocatalyst precursors require. Three such approaches are the use of nitrogen-containing polymers, templating methods, and metal-organic framework (MOF) precursors.

1.4.1 Nitrogen-containing polymers as precursors towards non-PGM electrocatalysts

Atomic nitrogen plays a key role in the activity of non-PGM electrocatalysts; however, several studies have hinted at the presence of different structures.[23, 49, 56, 85, 93, 94] Using nitrogen-containing polymers as precursors increases the concentration of nitrogen in the sample which aids the formation and stabilization of single-atom metal sites. Additionally, the N-rich polymers provide a structural framework to promote catalyst uniformity. Of the more popular precursors used, polyaniline is made through the oxidative polymerization of aniline using ammonium persulfate.[95] In a typical of non-PGM electrocatalysts using polyaniline, a metal salt precursor is dispersed throughout the monomer solution during polymerization. This method limits the amount of metal aggregation through sintering during high temperature pyrolysis thus increases the number of single-atom sites.[21, 58, 96] Another common polymer precursor for the synthesis of non-PGM electrocatalysts is polypyrrole. The addition of the metal salt serves a dual function by helping to activate the polymerization of pyrrole while also serving as the metal source for the formation of single-atoms.[97, 98]

Other works have aimed to use nitrogen-containing polymers as precursor coatings to prevent metal sintering during pyrolysis (e.g. polyvinylpyrrolidone [PVP]). PVP was used to coat a metal-organic framework (MOF) prior to pyrolysis to preserve the precursor structure while increasing the final nitrogen content.[60, 99]

1.4.2 Templating methods in the design of non-PGM electrocatalysts

Templates afford another strategy in the synthesis of non-PGM electrocatalysts with a high dispersion of single atoms. Templates are well-defined base structures around which functional precursors can be assembled. Given the robust structure of templates, they are able to withstand the high pyrolysis temperatures typically used during the synthesis of non-PGM electrocatalysts. The controlled decomposition of templates allows for the formation of even distributed single atoms during pyrolysis by restricting the amount of sintering. Hard templates require the use of a strong acid/base (e.g. hydrofluoric acid or sodium hydroxide) to initiate their removal. Commonly used hard templates are metal oxides including silica[100-105] and alumina[106]; these materials are used as a model hard template onto which MOFs[107] and metal porphyrins/phthalocyanines[108-110] are assembled. Similarly, vanadium oxide was used as a layered template to intercalate iron porphyrins. Following thermal treatment, the metal oxide was removed using hydrofluoric acid, yielding a high surface area catalyst.[111]

In contrast to hard templates, soft templates are decomposed during thermal treatment and do not require strong acids and bases. For example, polystyrene was shown to be effective in serving as a template lending to the formation of single-atomic metal sites in a high surface area material. Following the formation of the MOF structures within the polystyrene template, the precursor was pyrolyzed to remove the polystyrene template, and the MOF transformed into the carbon-derived electrocatalyst.[112]

1.4.3 Metal-organic frameworks as precursors towards non-PGM electrocatalysts

Recently, MOF-derived non-PGM electrocatalysts have been shown to be among the most active towards the ORR.[113] MOFs represent a class of crystalline materials composed of organic linkers

connected by metal ions at the coordination centers (**Figure 1.5**).[114] Their structures offer a major benefit during the synthesis of non-PGM electrocatalysts: 1) the inherent presence of a transition metal which is atomically distributed throughout the lattice of the MOF and 2) their highly porous structures which lend to high surface. For these reasons, using MOFs as precursors in the synthesis of non-PGM electrocatalysts can lead to a higher level of metal dispersion throughout the framework.[115] Dispersion is key as it allows for the formation of individual active sites while minimizing metal aggregation at high pyrolysis temperatures. During the thermal treatment of MOF precursors, the organic chains decompose into a porous carbon network, while metal atoms are partially reduced and bound within the carbon matrix as single atom structures. This process is highly sensitive to the synthesis variables such as the type of organic linker and the temperature of pyrolysis. A high level of control is desirable for the selective formation of metal active centers for the ORR. Much of the work in this area has focused on the use of the zeolitic-imidazolate framework, ZIF-8, as the MOF precursor to synthesize non-PGM electrocatalysts.[116] This is inspired by previous work, where zinc salts have been used as activating agent to generate pores upon thermal treatment and enhance surface area.[117-121] Currently, MOF-derived materials exhibit the highest activity of the non-PGM electrocatalysts using both RDE measurements and as cathode materials in PEMFCs.

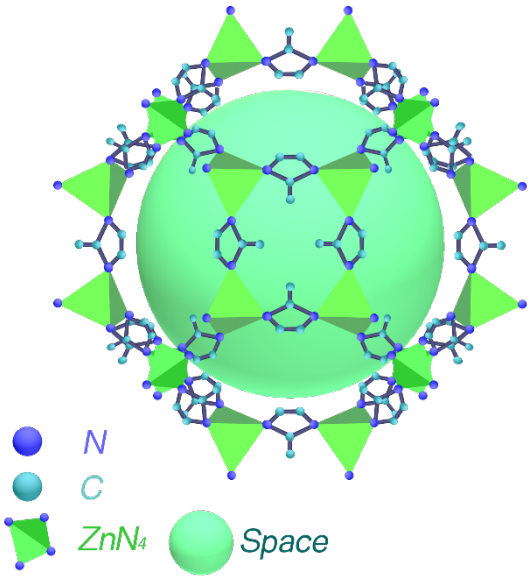

Figure 1.5 A MOF made up of a zinc center (green tetrahedrons) bonded to methylimidazole groups.

1.5 Electrochemical measurements of the ORR

1.5.1 The three-electrode setup

A common technique to probe the electrochemical reactivity of catalysts is a three-electrode setup (**Figure 1.6**). It consists of a working electrode, a counter electrode, and a reference electrode. In the case of the ORR, the working electrode is a rotating disk electrode (RDE), which consists of a central circular disk made of glassy carbon encased in a Teflon sheath. The electrocatalyst being investigated is deposited on the RDE to measure its activity. The counter electrode as the name suggests serves as a counter to the reaction occurring on the working electrode to complete the circuit. The reference electrode's operating potential is known and serves as the reference to the

potential applied on the working electrode. A graphite rod serves as the counter electrode while a reversible hydrogen electrode is the reference electrode. The three electrodes are placed in the electrolyte solution which serves as the reaction medium. The pH of the electrolyte solution is varied accordingly based on the relative concentrations of the acid and base. A reactant gas is then bubbled through the electrolyte solution such to react on the working electrode. For ORR, this gas is molecular oxygen (O_2), The RDE is rotated at a predetermined rotation rate to induce gas flow from the electrolyte to the catalyst surface through convection; this can assist in overcoming any mass transfer limitations.

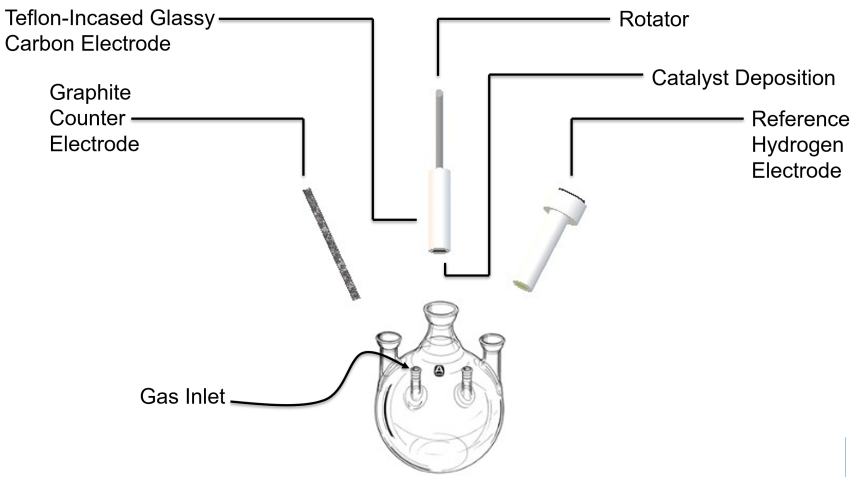

Figure 1.6 Illustration of a typical three-electrode setup used to measure the activity of electrocatalysts.

1.5.2 Linear-sweep voltammetry

Linear-sweep voltammetry (LSV), cyclic voltammetry (CV), open circuit potential (OCP) and the Koutecky-Levich analysis measurements are the main techniques to analyze the activity of candidate ORR electrocatalysts.

LSV is a one direction potential sweep over a given range while the resulting current is recorded to generate a polarization curve such as **Figure 1.7** (for carbon-supported platinum catalyst for ORR). This graph depicts the current generated on a catalyst surface as a function of the applied potential with respect to the reference electrode (V vs. RHE).

Generally, the polarization plot can be divided into three distinct regions.[122, 123] The first, known as the activation region (purple), refers to the region right before any current is detected, thus no reaction is taking place at that potential. The onset potential is the inflection point at which there is a sharp increase in the current measured and signifies that the catalyst has been *activated*. At the onset potential, the reaction at the working electrode results in an increase of measured current. Given that the ORR is a cathodic reaction, the generated current is negative (negative y-value on the graph). The kinetic region (blue, middle), otherwise known as the ohmic region, is symbolized by the near linear voltage drop as a response to an increase in the current. In this region, the increase in current is limited by the resistance arising from electrolyte-ion interactions as well as interactions with the catalyst. The half-wave potential can be obtained from this region and is defined as the potential at which half the limiting current density is achieved. The onset potential and half-wave potential are the two common benchmarks to compare the activity of non-PGM ORR electrocatalysts. Lastly, the mass transfer limited region (pink, left) is characterized by a saturation of the active sites on the catalyst such that the current density becomes independent of

the potential. The limiting current is the highest current that can be generated by the catalyst given the limitation on the reactants diffusing through the boundary layer towards the catalyst surface. The characteristic limiting current density can be used qualitatively to assess the relative number of active sites between electrocatalysts.

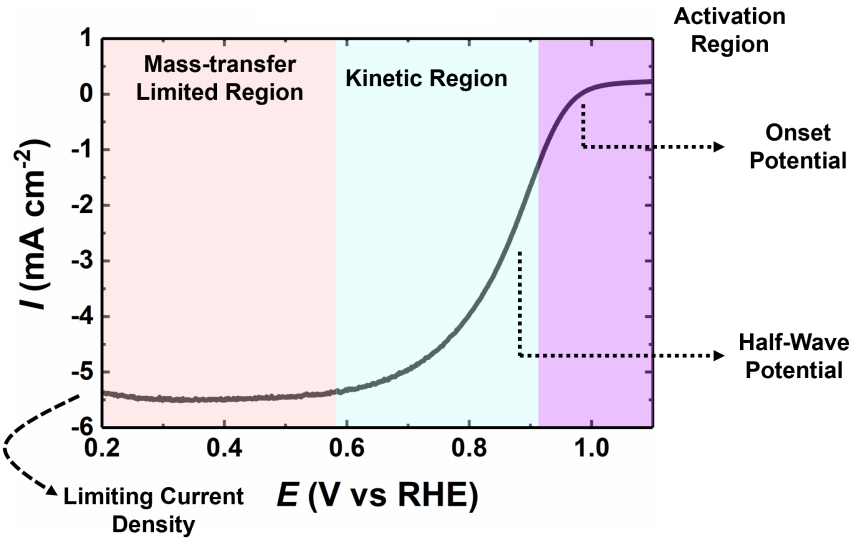

Figure 1.7 Polarization plot of 20% Pt/C electrocatalyst in a O_2-saturated 0.1M $HClO_4$ electrolyte

1.5.3 Experimental methods for investigating the ORR mechanism

Certain techniques can be utilized to the probe the mechanism of the electrochemical reduction of oxygen. Koutecky-Levich analysis relies on the relationship between the limiting current attained in the mass-transfer limited region and the rotation rate applied to the RDE according to equation (1.4) where ω stands for angular rotation rate in radians per second, the mass-transfer limited is given by i_L and n refers to the number of electrons transferred during the reaction.[124] The remaining variables describe constants relating to the system where F is the Faraday constant, A is the area of the electrode surface, D is the diffusion coefficient of the reactant through the electrolyte, v is

the viscosity of the electrolyte, and C is the concentration of the reactant in the electrolyte which in the case of a reacting gas (oxygen) in a liquid electrolyte (perchloric acid) is dependent on the solubility of the gas in the reaction medium. Linear regression identifies the relationship between the limiting current and the angular rotation rate to calculate the number of electrons transferred during the reaction. In the case of the ORR, the value of n (the number of electrons) falls between two and four, and correlates to the $2e^-$ and $4e^-$ pathways.

$$\frac{1}{i_L} = \frac{1}{i_K} + \left(\frac{1}{0.62nFAD^{\frac{2}{3}}\nu^{-\frac{1}{6}}C}\right) \times \omega^{1/2} \qquad (1.4)$$

A more direct approach utilizes a rotating ring-disk electrode (RRDE). The RRDE includes an additional working electrode in the form of a platinum ring surrounding the glassy carbon disk of the first working electrode. This method is especially useful in investigating the ratio of hydrogen peroxide formed through the $2e^-$ pathway on the first working electrode containing the catalyst under study. The secondary ring electrode serves to reduce the hydrogen peroxide following its formation on the first working electrode; the current generated at the secondary ring electrode is also measured and is an indicator of the level of hydrogen peroxide being generated on the first working electrode which suggests which electron transfer pathway dominates for the ORR.

1.6 Proposed mechanisms on carbon-based single atom non-PGM electrocatalysts

Metal surfaces are relatively simple to model and are computationally-less intensive to calculate. In an effort to understand and develop a suitable model for the ORR mechanism on carbon-based non-PGM electrocatalysts simplified representations of single-atom structures were developed. As mentioned earlier the oxygen reduction at a low pH can progress through the 2e- pathway and

form hydrogen peroxide as an intermediate prior to forming water; the alternative and more favorable pathway is the 4e- pathway which is a direct reduction into water.

Through the investigation of nearly 40 non-PGM electrocatalysts it was shown that metal-based active structures were more conducive to the 4e- pathway in addition to a secondary reduction of hydrogen peroxide, whereas metal-free nitrogen-carbon sites promoted the 2e- pathway through hydrogen peroxide and depending on the chemical environment of nitrogen (pyrrolic versus pyridinic) can initiate a further reduction into water.[125] Later work demonstrated that nitrogen-carbon sites were not active towards the peroxide reduction reaction while metal-based showed moderate activity suggesting they possibly contributed towards the 2e- pathway.[126]

Using density-functional theory (DFT) to model single-atom FeN_4 embedded in carbon, it was shown that oxygen undergoes reduction following the associative mechanism. **Scheme 1.3** shows that the rate-determining step (RDS) shown in red was suggested to be the OOH* bond cleavage.[127, 128]

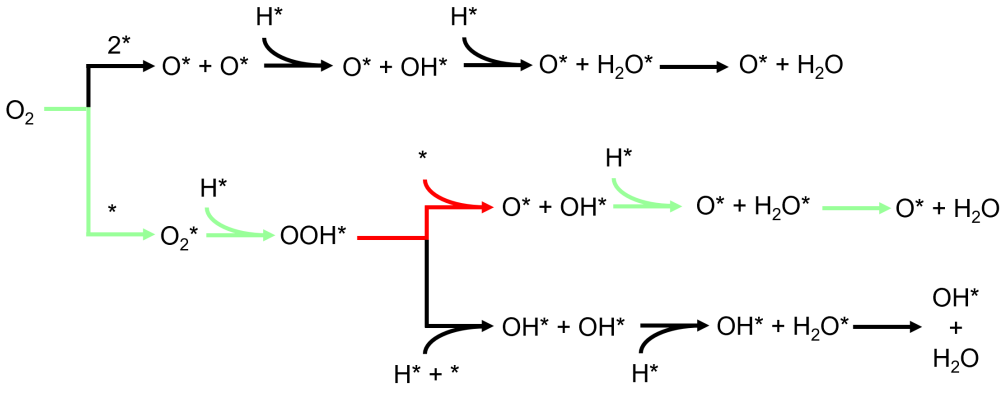

Scheme 1.3 Proposed ORR pathways on FeN_4 embedded graphene.

A further study related the adsorption of the adsorbed hydroxide intermediate OH* to the potential applied. It showed that in the range of 0.28 V to 1.00 V the Fe-centered site of the FeN_4 structure was occupied by OH*. During this operational range OH contributes to the activity observed in the iron-based non-PGM electrocatalyst and can influence the binding energies of certain reaction intermediates on the catalyst iron active center.[129] In accordance with later work using a first-principle DFT study, it was shown that the interatomic distances between single-atom sites. It was shown that by reducing the distance between adjacent FeN_x (x = 3, 4) sites the adsorption energies of oxygen and the hydroxide ion which translates to a greater active site density.[130] More recent work has suggested an atypical pathway wherein two hydroxide ions are bonded to the same active metal-coordinated active site.[131]

1.7 Goals of thesis

The underlying aim of this thesis is two-fold: (1) to develop a framework through which to understand the structural origins of the activity observed in non-PGM electrocatalysts and (2) to improve on existing synthetic strategies to enhance structural and morphological homogeneity in non-PGM electrocatalysts. The overarching goal is to develop robust synthetic pathways to achieve active cathode catalysts for the ORR through the design and functionalization of our material precursors.

On a fundamental level, an understanding of the design principles of single-atom electrocatalysts for the electrochemical ORR provides a means to expand on the synthetic processes leading to their formation. In a broader sense, these design principles can guide the development of high performance non-PGM ORR electrocatalysts which will decrease the costs of PEM fuel cells and

allow for its commercialization for a variety of industries in clean energy storage and utilization. The ORR remains a vital reaction in a host of other technologies/processes including methanol fuel cells, ethanol fuel cells, formic acid fuel cells, solid acid fuel cells, metal-air batteries, and in peroxide synthesis. Progress in material design for the ORR can be applied and extended to those reactions.

In the following chapters, strategies towards the design and synthesis of MOF-derived single-atom electrocatalysts for the ORR are outlined. Chapter 2 presents the work on using ZIF-8 as a precursor to correlate the effect of temperature on the decomposition of the MOF. Experimental evidence along with a DFT study showed that the presence of neighboring iron can lead to an enhancement of the ORR activity through the activation of the surface carbon atoms near the single atom iron site and favor the cleavage of the O-OH bond. This work led to the development of a new MOF structure based on cadmium as the sacrificial metal. In Chapter 3, we demonstrated the capability to synthesize an active single-atom based non-PGM electrocatalyst at a significantly lower temperature using our newly developed MOF. At a higher synthesis temperature our material exhibited notable activity both in a three-electrode and in a membrane electrode assembly (MEA) setup. Chapter 4 covers the work done on using an immobilization strategy to enhance the dispersion of our MOF precursor across a carbon support; we demonstrate that we are able to achieve near complete dispersion of the active metal (Fe) with a limited formation of nanoparticles. Lastly, Chapter 5 presents the concluding remarks on this dissertation along with future research directions and recommendations.

CHAPTER 2

THE SYNERGISTIC EFFECTS OF FeN_X AND SUPERPARAMAGNETIC IRON IN THE ELECTROCATALYTIC REDUCTION OF OXYGEN

2.1 Introduction

Development of high performance non-PGM ORR electrocatalysts requires an understanding of the structures contributing to the high activity and stability. Controversy remains regarding the nature of the active center in non-PGM catalysts. Among those structures, iron-coordinated-nitrogen species or FeN_x moieties have long been hypothesized to be the active centers towards the reduction of oxygen.[5, 23, 56, 103, 132-136] Iron carbides, nitrides, and reduced iron nanoparticles embedded within a carbon matrix have also been proposed to serve as the active species.[4, 34-36, 137] Given their structural heterogeneity, non-PGM electrocatalysts are still under scrutiny as to what constitutes the active site for the ORR.[138] Typically, studies investigate several pyrolysis temperatures and gas environments in an attempt to identify the temperature which results in the most active catalyst.[53, 139]

The temperature of pyrolysis plays a critical role in regulating the structures formed in the final catalyst material. Shown in **Figure 2.1**, during pyrolysis the MOF structure undergoes transformations at each stage which are governed by temperature.

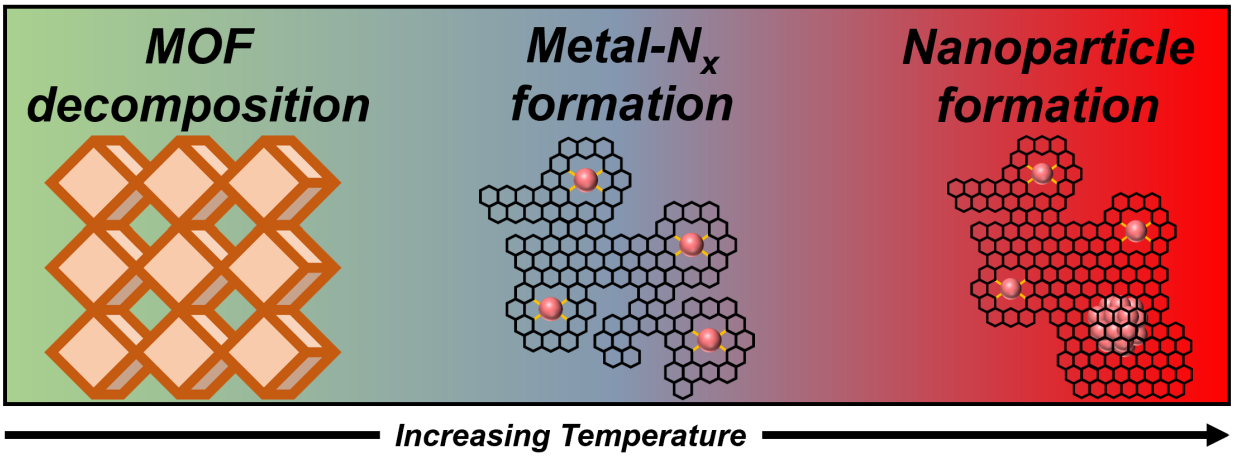

Figure 2.1 Thermal map showing the stages in the conversion of a MOF precursor into a carbon-based catalyst.

Initially, the MOF structure begins to decompose as the organic linkers break down. In the second phase, the thermal energy lends metal atoms greater mobility to coordinate and form single atoms structures embedded within the carbon support. At elevated temperatures, sintering can occur which allows for the formation of crystalline nanoparticles either in the reduced phase or as carbides or nitrides depending on the reaction conditions.

The temperatures assigned to this thermal map are dependent upon the catalytic precursors and gas environment; however, in the context of typical pyrolysis-based syntheses of MOF-derived non-PGM electrocatalysts this trend appears often. In this work, we endeavored to develop an intuition for the relationship between temperature and structure of the non-PGM electrocatalysts as defined through the use of ZIF-8 as the primary MOF precursor.

2.2 Experimental design

In this study, our goal was to understand the structure-property-activity relationship in the ZIF-8 derived non-PGM electrocatalysts for the ORR; specifically, we systematically varied the pyrolysis temperature, characterized the chemical and morphological structure, and measured the corresponding electrochemical activity. Our experiment was designed to develop an understanding of the role of temperature and its impact on the chemical and physical structure of non-PGM electrocatalysts. Initially, we surveyed several of the reported active non-PGM electrocatalysts to obtain a model electrocatalyst for our study. The next stage involved the synthesis of the carbon-based electrocatalysts. We used characterization techniques to determine the chemical and physical properties of the electrocatalyst. Lastly, we compared the catalytic activity to explore the structure-activity relationship of our materials.

Based on our experiments, we propose a model that integrates both an iron-coordinated-nitrogen structure and an iron particle which collectively act to activate the catalytic surface for the ORR under acidic conditions. By calculating the adsorption energies of the reaction intermediates on the surface of the model catalyst we show that the presence of an iron nanoparticle in the vicinity of the single atom structure can lead to a more active catalyst.

2.3 Experimental methods

2.3.1 Material synthesis

Synthesis of ZIF-8 derived non-PGM electrocatalyst ($FeNC_T$). The synthesis of ZIF-8 based iron electrocatalysts was modified from literature.[23] The first stage involved the mixing of the zeolitic

imidazolate MOF precursor, ZIF-8, (800 mg) was ball-milled with a nitrogen-containing compound, 1, 10-phenanthroline (200 g), and the active metal salt iron(II) acetate (32 mg). The ground powder was collected and transferred to an alumina combustion boat (Sigma Aldrich, 5 mL). The flash pyrolysis technique was used in the synthesis of Fe-C-N_T. This combustion boat was then placed inside of a quartz tube (I.D.: 22 mm, O.D.: 25 mm, and length: 0.6 m), and purged with ammonia for about 95 min. After the purge, the tube was inserted into a tube furnace (Thermo Fisher Scientific™, Lindberg/Blue M™ Mini-Mite™). The sample underwent a flash pyrolysis (**Figure 2.2**): a tube furnace was heated to a target temperature (750-1050 °C); the quartz tube was then inserted into the furnace for a total reaction time of 15 min under the continuous flow of ammonia. Lastly, the tube was removed and allowed to naturally cool, while remaining under the flow of ammonia. The final catalysts were stored in vials and sealed with parafilm.

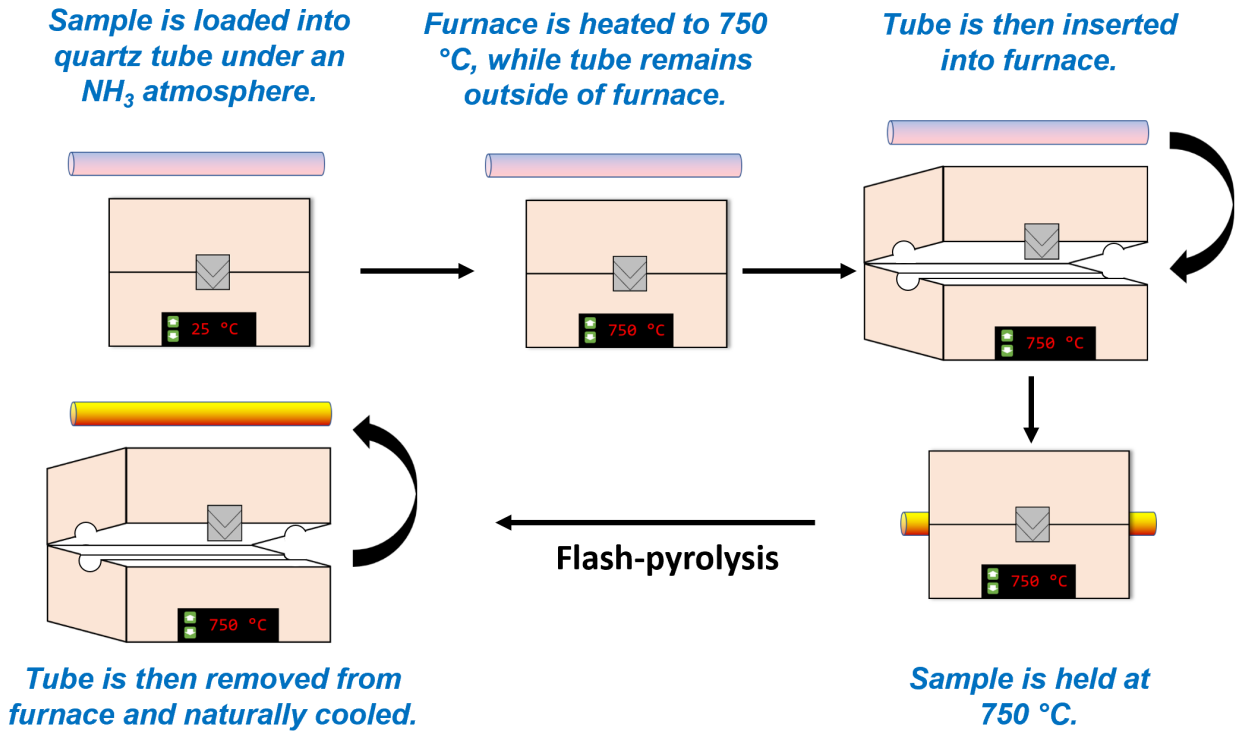

Figure 2.2 Schematic of the typical pyrolysis procedure "flash pyrolysis" to make $FeNC_T$.

2.3.2 Material characterization

Transmission electron micrographs and scanning transmission electron micro-images (STEM) were acquired at an accelerating voltage of 200 kV using a FEI Talos F200X TEM/STEM. TEM sample were prepared as follows: catalyst materials were dispersed in ethanol to create a translucent solution, next a few drops of solution were deposited onto carbon-coated TEM grids and allowed to dry. Powder X-ray diffraction (PXRD) patterns were acquired using a Rigaku Miniflex 600 with a Cu Kα radiating source. Typically, a continuous scan was performed between 10 and 80° 2θ. Inductively coupled plasma mass spectrometry (ICP-MS) analysis was carried out on a PerkinElmer NexION 350D system. Mössbauer analysis was performed with a Co^{57} source emitting gamma rays at 14.4 keV on a constant acceleration spectrometer at 300 K. X-ray photoelectron spectroscopy (XPS) was performed using a Kratos Axis ULTRA with an Al Kα

monochromatic X-ray source to determine the binding energy of nitrogen in each of the catalyst samples.

2.3.3 Electrochemical analysis

A three-electrode setup was used to evaluate the oxygen reduction reaction (ORR) activity of these catalysts. A graphite rod (Pine, MPGRR250) was used as the counter electrode and a reversible hydrogen electrode (Hydroflex™, ET070 eDAQ) was used as the reference electrode. The working electrode was prepared using the following procedure: 5 mg of the catalyst was dispersed in a solvent containing 235 µL of deionized (DI) water (18.2 MW·cm, Thermo Fisher Scientific™, Barnstead™ E-Pure™), 235 µL of ethanol (200 Proof, Decon Labs, Inc.), and 45 µL of Nafion binder (D521 alcohol based 1100 EW at 5% weight, Nafion™ Store) to create an ink mixture. This ink mixture was sonicated for 30 min prior to drop-casting onto the surface of a glassy-carbon rotating-disk electrode (RDE). A total of 20 µL of the ink was deposited onto the surface of RDE in two equal portions of 10 µL. After the first deposition of 10 µL, the ink was given 10 min to dry, followed by the deposition another 10 µL to create a thin film catalyst layer on the electrode surface. The ORR performance of the catalysts was tested in 0.1 M perchloric acid ($HClO_4$) electrolyte (70% Veritas Double Distilled, GFS Chemicals) using a standard three-electrode system. Oxygen gas (Airgas Inc., 99.999%) was bubbled through the electrolyte for a total of 40 min prior to the RDE testing. Prior to the measurements, the catalysts underwent a conditioning step in situ by sweeping between 0.0 V and 1.1 V versus RHE at a step of 0.01 V for a total of two times using linear sweep voltammetry (LSV). Staircase voltammetry (SCV) was carried out between 0.0 V and 1.1 V at an interval of 0.02 V and a step period of 30 s to obtain the polarization curves.

2.3.4 Density-functional theory calculations

Periodical spin-polarized density functional theory (DFT) calculations were performed using plane-wave basis code Castep with ultrasoft pseudopotentials.[140] The generalized gradient approximation (GGA) with Perdew-Burke-Ernzerhof (PBE)[141] function was used to describe the electronic exchange and correlation. The cutoff energy for plane-wave basis set was set to 600 eV. The Brillouin zone was sampled on 4×4×1 Monkhorst-Pack grids. The GGA+U (U_{eff} = 2.2 eV) approach was used to correct self-interaction errors of iron d-electrons.[142] The orthorhombic graphene supercells with lattice parameters of a=9.847 Å and b=8.527 Å were used to model the carbon network. A 15 Å thick vacuum layer in the Z direction was used to minimize the possible interactions between the periodic graphene sheets. The carbon bond length is 1.421Å in the optimized graphene sheet, which agrees well with previous theoretical results.[143] The convergence tolerances of geometry optimization were set to 1.0×10^{-5} eV/atom for the energy, 0.03 eV/Å for the maximum force, and 1.0×10^{-3} Å for the maximum displacement. The adsorption energy (E_{ads}) is calculated as the energy difference between the adsorbate-catalyst system and the assembly of the isolated catalyst and the adsorbate in the gas phase according to the following equation:

$$E_{ads} = E_{catalyst+adsorbate} - E_{catalyst} - E_{adsorbate}$$

2.4 Results and discussion

2.4.1 Characterization of ZIF-8 derived non-PGM electrocatalyst ($FeNC_T$)

To analyze the morphology of our catalysts, high-resolution STEM was carried out on both $FeNC_{750}$ and $FeNC_{950}$ catalysts using STEM/TEM. For $FeNC_{750}$, the lowest pyrolysis temperature,

the MOF structure was mostly preserved, and some nanoparticles were formed (**Figure 2.3**). As can be seen in **Figure 2.3a**, the structure is highly heterogenous with fibrous carbon interspersed with nanoparticle structures in the top right and bottom left, a carbonaceous network in the top left and what appears to be an intermixed MOF remnant structure (**Figure 2.3b**).

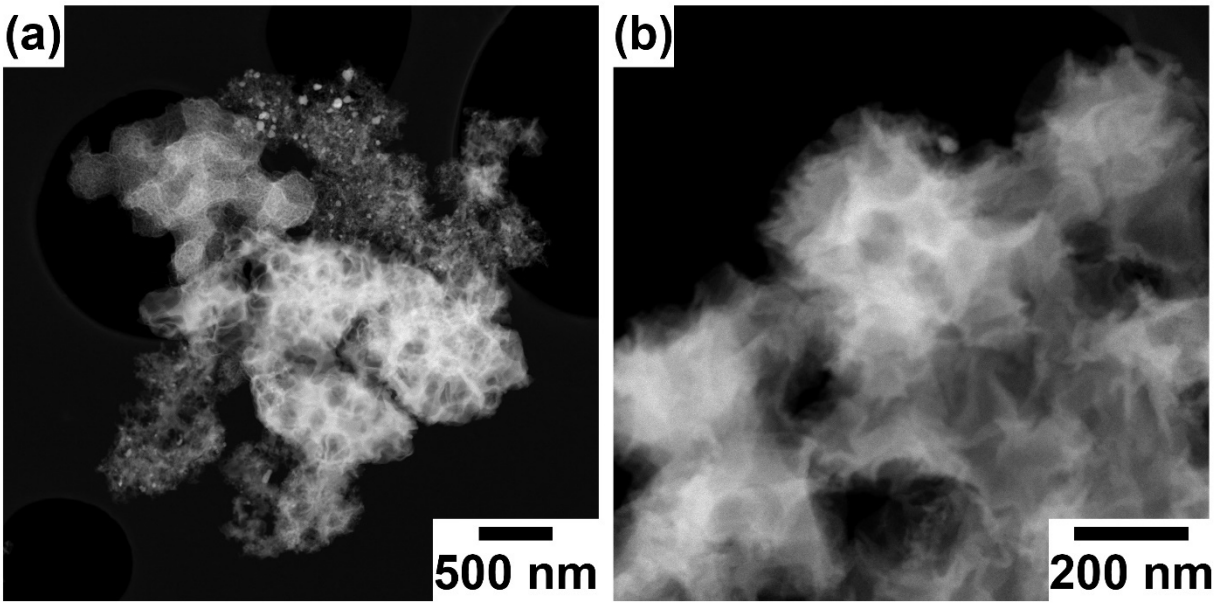

Figure 2.3 (a) Low-magnification TEM image of $FeNC_{750}$ showing a highly heterogeneous structure (b) TEM image of $FeNC_{750}$ showing remnants of the MOF structure.

Judging from the electron dispersive X-ray spectroscopy (EDS) mapping of $FeNC_{750}$ shown in **Figure 2.4a and b** there is a large amount of remaining zinc interspersed throughout the structure. The distribution of elemental zinc and iron within the nanoparticle (**Figure 2.4c and d)** structures indicates that the partial evaporation of zinc coupled with the formation of a carbonaceous support conducive to hosting single atom structures did not occur.

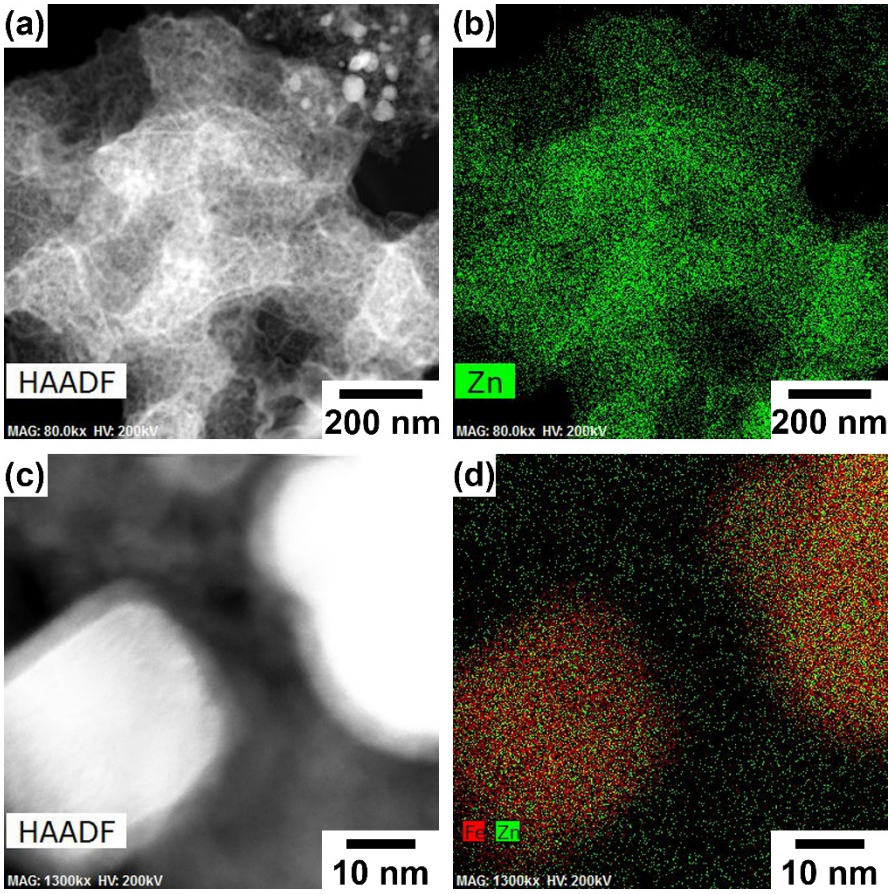

Figure 2.4 Representative STEM image of as-made $FeNC_{750}$ (a, c) EDS mapping showing the abundance of remaining zinc after pyrolysis.

The EDS spectrum of a $FeNC_{750}$ nanoparticle further shows both Zn and Fe existed in the product (**Figure 2.5**). This is likely due to the relatively low temperature of 750 °C used during synthesis which is below the bulk boiling point of zinc. This indicates that a higher pyrolysis temperature is needed to remove zinc and generate an active electrocatalyst.

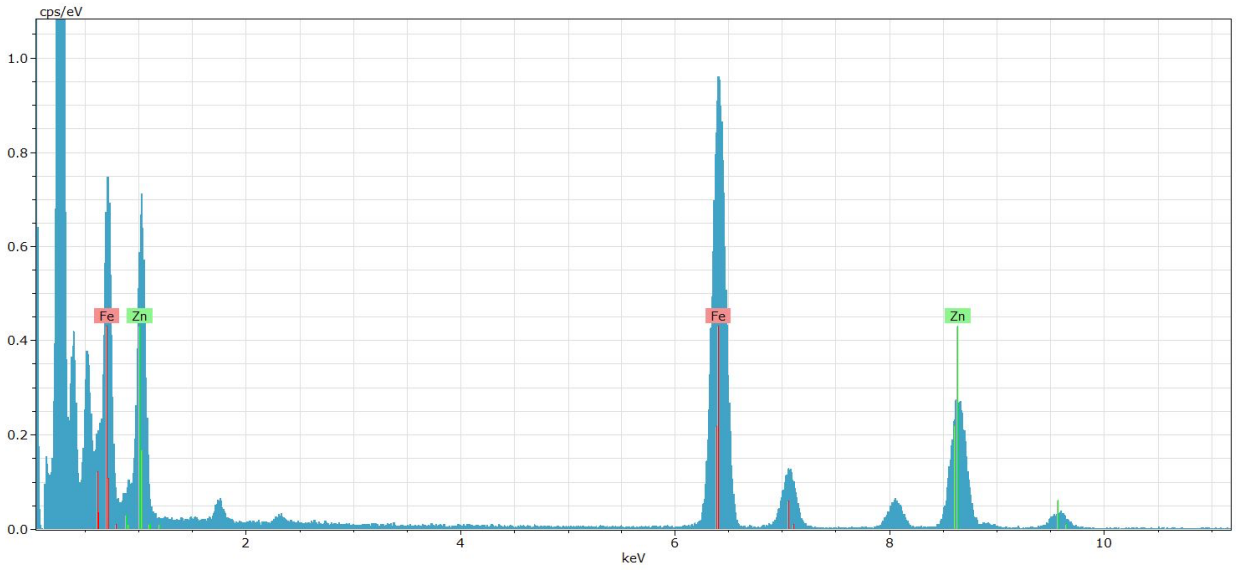

Figure 2.5 EDS spectrum showing the presence of Zn and Fe.

In contrast, the TEM image of $FeNC_{950}$ (**Figure 2.6a**) portrays a catalyst layout consisting of iron nanoparticles with a darker contrast, on the order of 10 to 20 nm in diameter, encapsulated within a graphitic carbon framework. **Figure 2.6a inset** shows an iron nanoparticle of about 20 nm encapsulated by a 1 nm thick layer of graphitic carbon. Dark-field TEM in **Figure 2.6b** depicts single-atomic iron species which can be distinguishable through the z-contrast and appears as white spots against a dark plane.

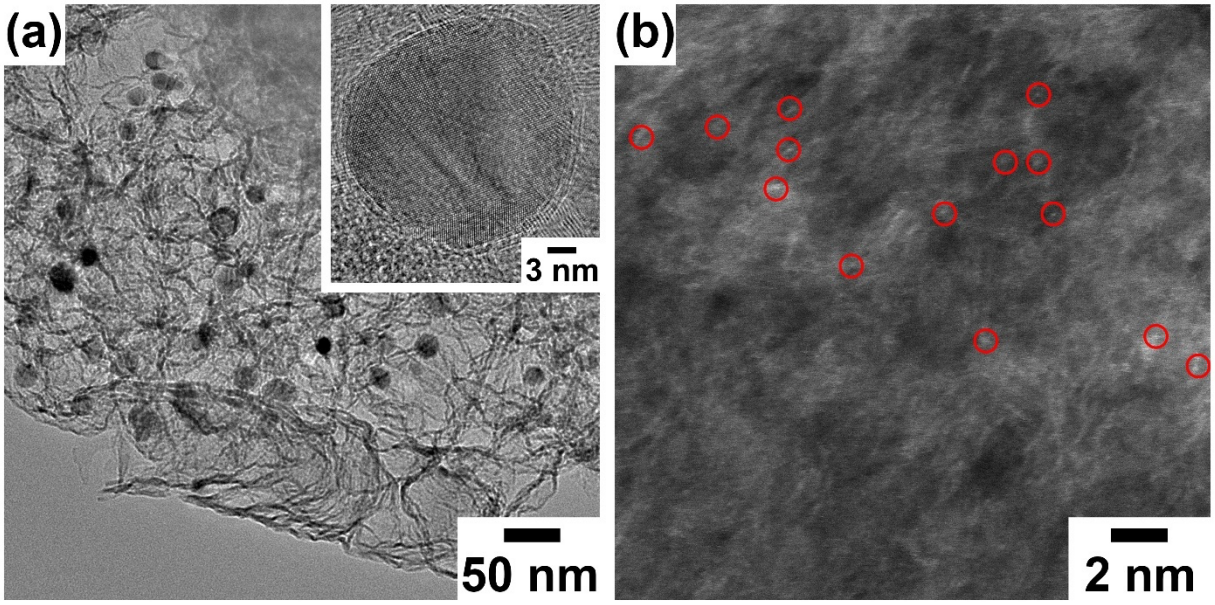

Figure 2.6 (a) TEM of $FeNC_{950}$ showing graphitic carbon with encapsulated iron nanoparticles (b) Dark-field STEM of $FeNC_{950}$ showing possible single-atomic iron moieties circled in red.

X-ray photoelectron spectroscopy (XPS) was used to probe the chemical environment and valence states of the elements present on the material surface of the as made electrocatalysts. As shown in **Figure 2.7**, the peaks corresponding to iron were not discernable from the general spectrum of both $FeNC_{750}$ and $FeNC_{950}$. Noticeably, the zinc 2p peaks are prominent for $FeNC_{750}$ but are absent for $FeNC_{950}$; this signifies that in the case of $FeNC_{750}$ there remains a significant amount of zinc post pyrolysis which is also what is observed in the above EDS mappings. In the case of $FeNC_{950}$, the absence of the zinc peaks demonstrates that zinc had been removed from the catalyst during pyrolysis which allowed for the conversion of the MOF material.

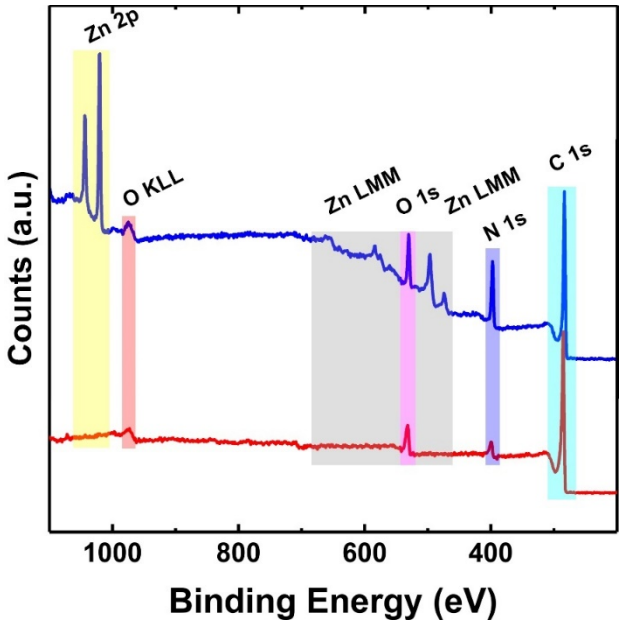

Figure 2.7 Survey XPS for $FeNC_{750}$ (blue) and $FeNC_{950}$ (red) with chemical regions highlighted.

Based on the ICP-MS measurements (**Table 2.1**) of the weight percentages of iron and zinc in $FeNC_{850}$, $FeNC_{950}$, $FeNC_{1050}$, with an increase in temperature the relative amounts of zinc decrease while an increase in the iron amounts is observed. This indicates that higher temperatures can enhance zinc removal which can effectively lead to a transformation of the catalyst structure. However, a further increase in temperature causes the relative concentration of iron to increase through the removal of zinc and carbon. Additionally, the carbon becomes more graphitic as seen in **Figure 2.6a**. These structural changes affect the relative abundance of specific active sites. A closer investigation of the XPS profile of the nitrogen 1s region for all four catalysts shows the presence of the metal-nitrogen bond in the samples synthesized at temperatures greater than 750 °C (**Figure 2.8**). This is characteristic of the single atom iron structures coordinated by nitrogen present within these materials.[46] The binding energies associated with the different nitrogen structures are summarized in **Table 2.2**.

Table 2.1 Inductively coupled plasma mass spectrometry (ICP-MS) results for the $FeNC_T$ electrocatalysts.

	Zn (wt. %)	**Fe (wt. %)**
$FeNC_{850}$	4.3	5.6
$FeNC_{950}$	0.18	5.5
$FeNC_{1050}$	0.01	7.2

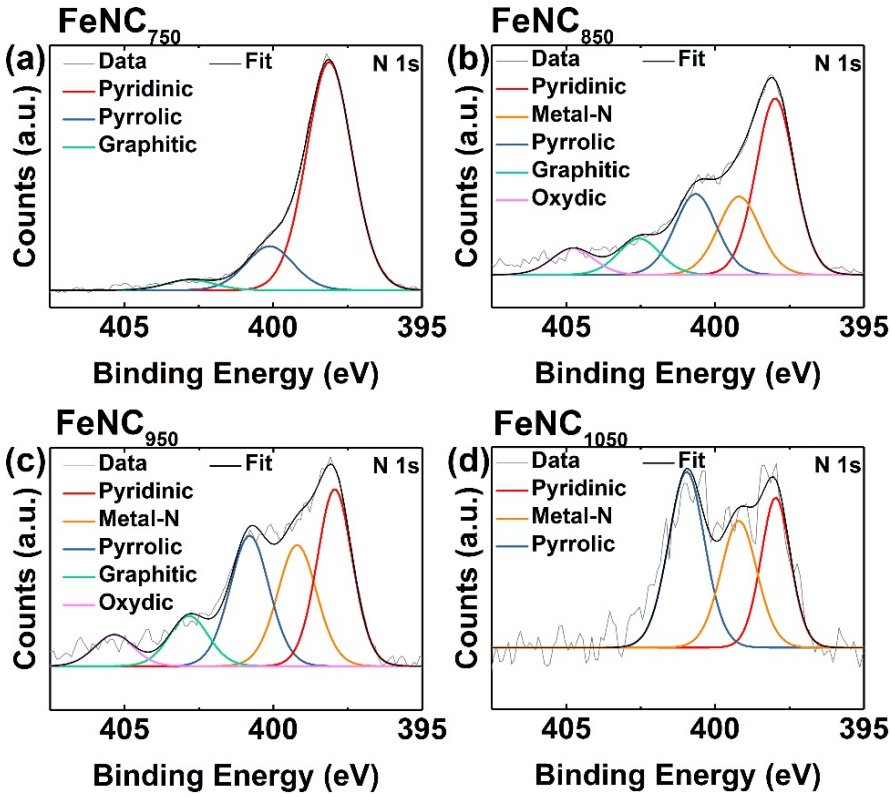

Figure 2.8 XPS of nitrogen 1s region for $FeNC_T$ electrocatalysts; the peaks correspond to the various nitrogen species present within each sample based on the binding energy.

Table 2.2 X-ray photoelectron spectroscopy analyses of the nitrogen species in the $FeNC_T$ electrocatalysts.

Sample	Binding Energy (eV)				
	Pyridinic	**Metal-N**	**Pyrrolic**	**Graphitic**	**Oxydic**
$FeNC_{750}$	398.1	-	400.1	402.8	-
$FeNC_{850}$	398.0	399.2	400.7	402.6	404.8
$FeNC_{950}$	397.9	399.2	400.8	402.8	405.3
$FeNC_{1050}$	398.0	399.2	401.0	-	-

Powder X-ray diffraction (PXRD) was used to investigate the bulk crystal structure of the four electrocatalysts. **Figure 2.9** shows that $FeNC_{750}$ contained peaks pertaining to iron zinc carbide (Fe_3ZnC). This confirmed the results from the above EDS and XPS data which indicated that there remained a residual amount of zinc within the electrocatalyst post pyrolysis; at 750 °C, zinc is likely to agglomerate with the iron in the sample and form an iron zinc carbide crystalline phase structure. With an increase in temperature the coupled formation of reduced iron as well as iron nitride (Fe_2N) is observed; thermal treatment under ammonia favors the formation of nitride structures which was expected.[144] To investigate the bonding environment of iron species Mössbauer spectroscopy was used. **Figure 2.10** shows that at the pyrolysis temperatures of 850 °C and 950 °C, catalysts $FeNC_{850}$ and $FeNC_{950}$, aside from containing the iron-nitrogen species, exhibit superparamagnetic α-iron. Catalyst $FeNC_{1050}$ shows a considerable decrease in the intensity

of the FeN_x species most likely due to having been pyrolyzed at 1,050 °C leading to a breakdown of single-atom sites and sintering; this was coupled with an increase in the intensity of superparamagnetic reduced iron structures.[44, 52-57] Peak assignments for both the iron-nitrogen moieties (FeN_x) and iron nanoparticle structures (spm α-Fe) are summarized in **Table 2.3**.

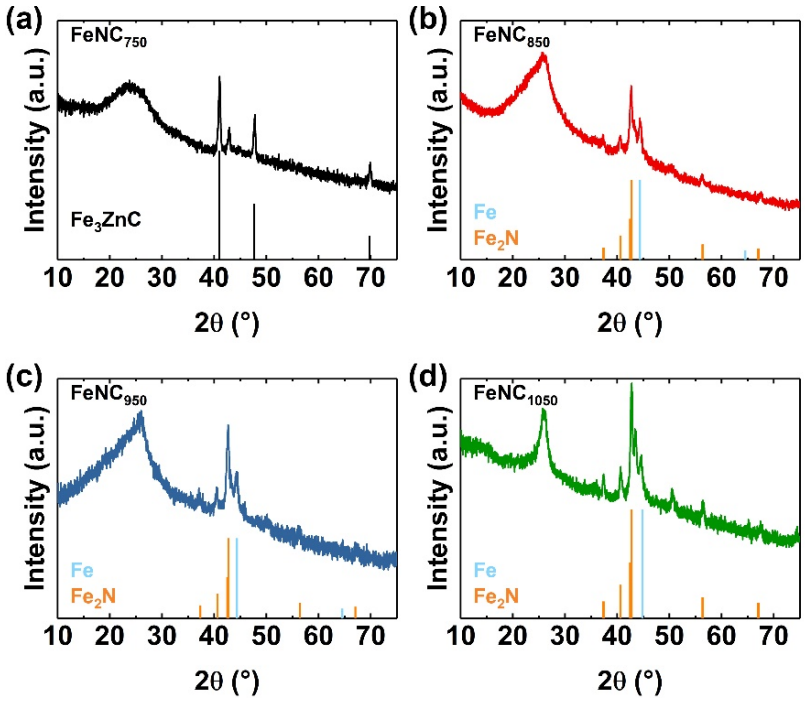

Figure 2.9 PXRD patterns of $FeNC_T$ electrocatalysts showing the presence of iron crystalline structures.

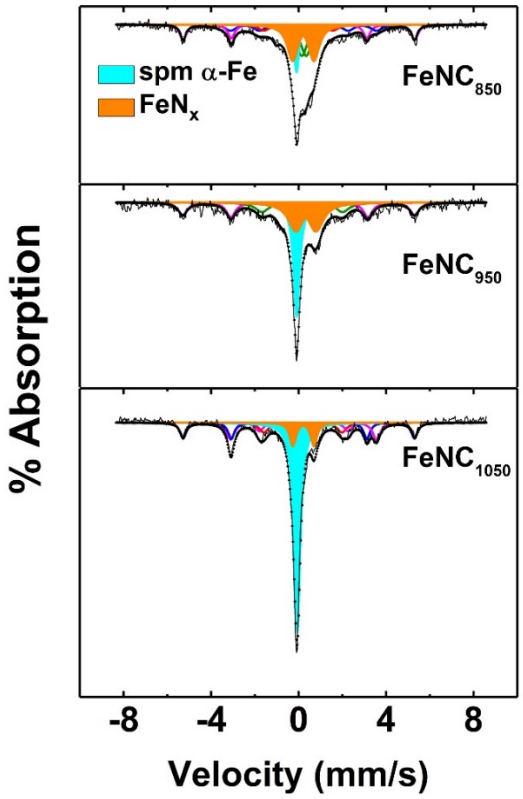

Figure 2.10 Mossbauer spectra of all catalyst samples with the peaks of both FeN_x and superparamagnetic α-Fe shown in orange and teal respectively.

Table 2.3 Mossbauer fitting results for the $FeNC_T$ electrocatalysts.

Sample	Component	δ_{iso} (mm s^{-1})	ΔE_Q (mm s^{-1})	FWHM (mm s^{-1})	Assignment
$FeNC_{850}$	Doublet	0.37	0.97	0.60	FeN_x
	Singlet	-0.07	-	0.26	α-Fe
$FeNC_{950}$	Doublet	0.32	0.89	0.82	FeN_x
	Singlet	-0.1	-	0.35	α-Fe
$FeNC_{1050}$	Doublet	0.22	0.96	0.34	FeN_x
	Singlet	-0.07	-	0.35	α-Fe

2.4.2 ORR activity analysis of ZIF-8 derived non-PGM electrocatalyst ($FeNC_T$)

Figure 2.11a depicts the linear sweep voltammograms of each of the four catalysts. A low temperature of 750 °C yields an inactive catalyst, while both $FeNC_{850}$ and $FeNC_{950}$ showed a considerable increase in activity. A loss in performance was observed for $FeNC_{1050}$, as indicated by the onset potential and half-wave potential (**Figure 2.11b**). The optimal pyrolysis temperatures for this catalyst lies in the range of 850 °C and 950 °C where an onset potential of 0.87 V and a half-wave potential of 0.76 V vs RHE was achieved for both.

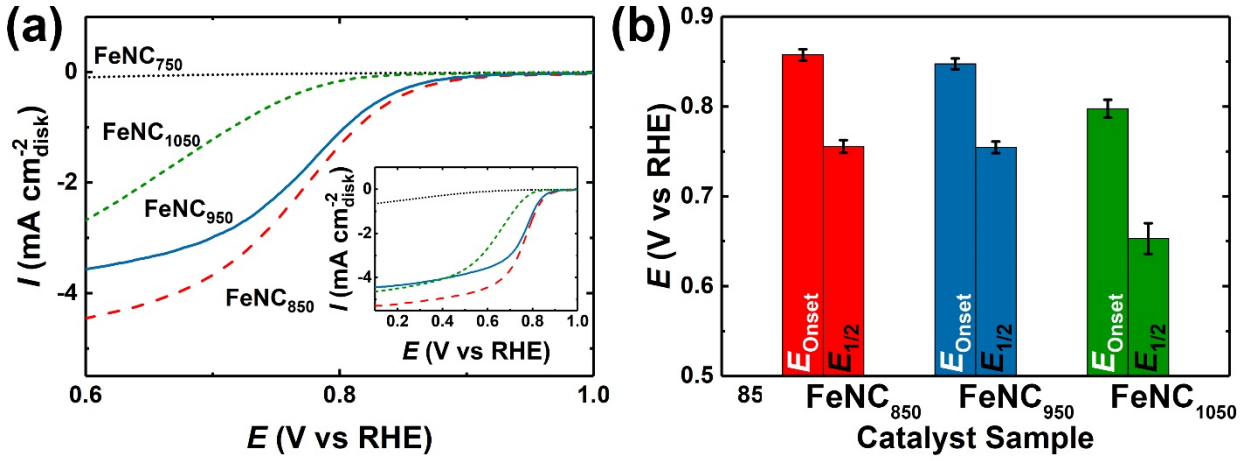

Figure 2.11 (a) Linear sweep voltammetry tests in 0.1 M $HClO_4$ from 0.6 V to 1.0 V versus RHE (b) E_{Onset} and $E_{1/2}$ values plotted for each catalyst sample.

2.5 Density functional theory calculations

Experimental evidence indicate that iron nanoparticles can enhance the ORR catalytic activity, but the catalytic mechanism is not clear.[4, 21, 32, 34, 35] To better understand the role of the iron nanoparticle in promoting the electrocatalytic reduction of oxygen, density functional-theory calculations were considered. As shown, our experimental data suggests that iron nanoparticles are an integral part of the catalyst framework. Simulations were run to account for changes in reaction thermodynamics through the inclusion and exclusion of an iron nanoparticle near an FeN_4 com-plex. In order to study the role of iron nanoparticles in FeNC catalysts, various chemical species adsorbed on Fe-N-C catalyst were studied by a simplified model.

In this model, pristine graphene was first examined without any dopants and was observed to be inactive due to its very weak adsorption of oxygen, which has an adsorption energy of about 0.03 eV. The insertion of an iron atom beneath the graphene sheet increases the adsorption energy of oxygen to about 0.48 eV. This value is significantly lower than that for the oxygen adsorption on iron in the FeN_4 embedded graphene, which was calculated to be about 0.93 eV. By including an iron atom near the FeN_4 embedded graphene structure, the adsorption energy of O_2 increases to about 0.98 eV. The DFT calculation was focused on the step of OOH dissociation, which is regarded as the rate-determining step (RDS) for the ORR on FeN_4 embedded in graphene.[127] In the absence of a nearby iron nanoparticle, this step ($O - OH^* \rightarrow OH^* + O^*$) results in OH* binding to a nearby carbon and O* remaining adsorbed on the iron. With the additional of a nearby iron atom, OH* is more easily stabilized. This schematic is shown in **Figure 2.12**. The OOH dissociation process follows that the OOH adsorbed on the iron dissociates to form OH adsorbed on a carbon atom near a nitrogen atom with the remaining O adsorbed on iron as shown in. According to our DFT calculations, the addition of iron nanoparticles near the FeN_4-embedded graphene center can enhance the adsorption of O_2 onto the FeN_4 center as well as favor the adsorption and dissociation of OH onto the neighboring carbon atom (highlighted in red in **Figure 2.12**); this can promote the process of OOH dissociation. Therefore, we can deduce that the ORR may prefer to happen at the area of coexistence of FeN_4 and iron nanoparticles.

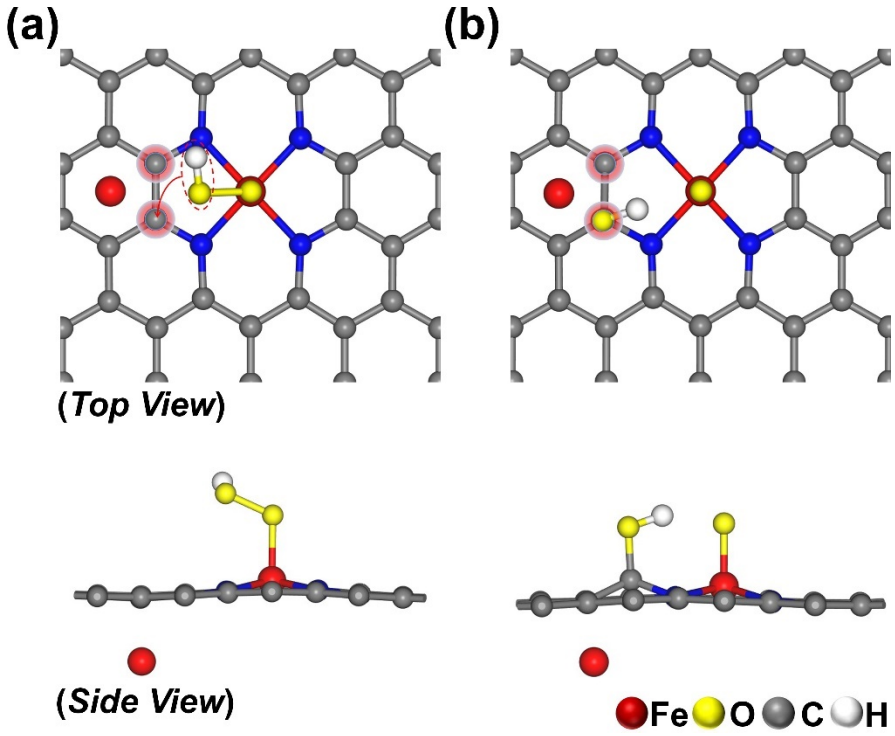

Figure 2.12 Carbon (gray), nitrogen (blue), red (iron), oxygen (yellow), hydrogen (white) (a) O – OH adsorbed onto the iron center of the FeN_4 species (b) O – O bond cleavage resulting on the remaining O on the iron center with the OH on the activated carbon (red glow).

As shown in **Figure 2.13** there is a decrease in the binding energy of OOH* onto the iron center coupled with a decrease in adsorption energy due to the OOH* bond cleavage carbon which would indicate a higher stabilization of intermediates along this reaction pathway. This would suggest that the presence of a metallic iron moieties near the FeN_4 centers could play a role in improving reaction kinetics. As shown by both Mössbauer spectra and transmission electron microscopy images, the active catalyst configuration comprises both single-atomic iron species and superparamagnetic iron nanoparticles. At higher pyrolysis temperatures, superparamagnetic α-iron is created coupled with the sudden activation of the catalysts. These nanoparticles are coated with several layers of graphene and are interspersed with the FeN_4 throughout the catalyst framework.

By conducting a series of DFT calculations we have been able to illustrate the role of superparamagnetic iron nanoparticles in activating surface carbon to allow for a lower adsorption energy associated with driving the OOH bond dissociation forward.

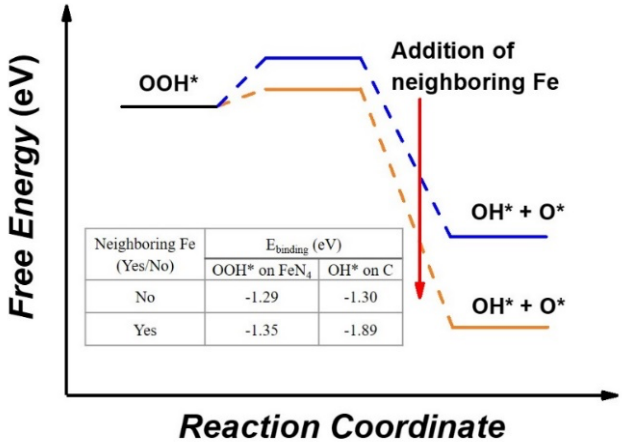

Neighboring Fe (Yes/No)	$E_{binding}$ (eV)	
	OOH* on FeN_4	OH* on C
No	-1.29	-1.30
Yes	-1.35	-1.89

Figure 2.13 Adsorption energy of adsorbate intermediates on different catalyst sites. The adsorption energy ($E_{binding}$) is calculated as the energy difference between the adsorbate-catalyst. system and the assembly of the isolated catalyst and the adsorbate in the gas phase according to the following equation: $E_{binding} = E_{catalyst+adsorbate} - E_{catalyst} - E_{adsorbate}$.

2.6 Summary and future considerations

In conclusion, we have demonstrated through a series of experimental results and computational methods that the presence of iron nanoparticles serves to enhance the activity of non-PGM. MOF-based catalysts were synthesized with ZIF-8 as a precursor at four different temperatures and were subjected to several characterization methods to determine the presence or lack thereof of species

within the catalyst material. It was revealed that indeed, the active catalysts contain both iron species and function to activate the nearby carbon atoms which aid in OOH bond cleavage which subsequently promotes the electrocatalytic reduction of oxygen.

The Mössbauer and TEM studies portray a catalyst structure comprising both single atomic iron species and superparamagnetic Fe nanoparticles. The graphene-coated nanoparticles are well dispersed across the carbon support along with the FeN_x sites. Thus, our model incorporated the presence of both structures in proximity and sought to explain its effect on the ORR. The DFT calculations suggest superparamagnetic Fe nanoparticles could facilitate the ORR through activating surface carbon to allow for a lower binding energy for intermediates associated with driving the dissociation of the OOH bond.

Moving forward, the need to develop strategies that can produce greater homogeneity in these carbon-based catalyst materials is of great importance. In doing so the presence of specific structures can be isolated and investigated; this can help eliminate the ambiguity surrounding heterogeneous materials.

CHAPTER 3

INVESTIGATING THE ROLE OF THE SACRIFICIAL METAL IN THE SYNTHESIS OF MOF-DERIVED NON-PGM ELECTROCATALYSTS FOR THE OXYGEN REDUCTION REACTION

3.1 Introduction

In the previous chapter, we showed that high pyrolysis temperatures are necessary for generating the active moieties in non-PGM electrocatalysts, but they also lead to the formation of agglomerated particles. In this context, MOFs are attractive precursors because of their ability to disperse the active metal prior to pyrolysis, thus generating a large density of single-atomic sites. Critical to this step is the use of a sacrificial metal (SM) that is present in the MOF precursor prior to pyrolysis. A classic example is that of ZIF-8 where zinc serves as the SM and is removed during pyrolysis. **Figure 3.1** highlights some of the functions of the SM which include dispersion of the active metal throughout the MOF, assisting in single atom site formation and increasing material surface area.

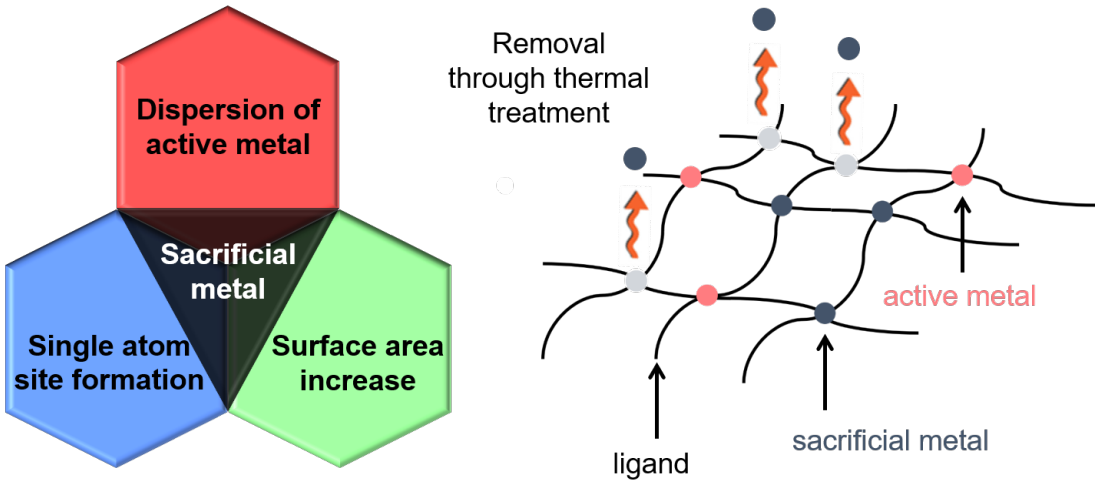

Figure 3.1 Summary of the role of the SM within non-PGM MOF precursor structures.

The dispersion of the active metal is hypothesized to restrict the extent to which the active metal can aggregate leading to a greater concentration of metal single-sites for high activity.[23, 59, 115] However, the high temperature associated with the removal of the SM results in the formation of agglomerated nanoparticles due to sintering.[145] In general, the SM should be able to incorporate within a MOF structure and possess a low enough boiling point temperature to be easily removed during the carbonization process. This places a constraint on potential elements that can serve this dual function. During the pyrolysis process, the precursor undergoes two successive changes prior to its transformation into an electrocatalyst. The first involves a breakdown of the organic linkers which are converted into carbon through a process known as carbonization.[146-148] This begins at relatively low temperatures ranging between 300 °C to 500 °C. The second process involves the extraction of the SM which depending on its bulk boiling temperature generally exceeds 800 °C.

Table 3.1 List of the composition and pyrolysis temperature of MOF precursors used in the synthesis of non-PGM ORR electrocatalysts.

Sacrificial metal species	Active metal species	Organic linker	Pyrolysis temperature (°C)	Suggested active structure	References
-	Co	3, 5-imidazole	750 (Ar)	CoN_4	[149]
Zn	Fe	imidazole	1050 (Ar) – 950 (NH_3)	-	[113, 150]
Zn	Fe	2-methylimidazole	1050 (Ar) – 950 (NH_3)	-	[22, 113, 150, 151]
Zn	Fe	2-ethylimidazole	1050 (Ar) – 950 (NH_3)	-	[113]
Zn	Fe	4-azabenzimidazole	1050 (Ar) – 950 (NH_3)	-	[113]
Zn	Fe	2-methylimidazole	1050 (Ar) – 950 (NH_3)	FeN_4C_{12}	[23]
-	Fe	2-aminoterephthalate	700 (Ar)	-	[152]
Zn	Fe	2-methylimidazole	1000 (Ar)	Single-atom Fe	[70]
Zn	Fe	imidazole	1000 (NH_3)	-	[115]
Zn	Fe	2-methylimidazole	1000 (NH_3)	-	[115]
Zn	Fe	2-ethylimidazole	950 (NH_3)	-	[115]
Zn	Fe	benzimidazole	1000 (NH_3)	-	[115]
Zn	Fe	2-methylimidazole	900 (N_2)	FeN_5	[153]
Zn	Fe	2-methylimidazole	1000 (Ar)	FeN_4	[60]
Zn	Fe	2-methylimidazole	900 (Ar)	Single-atom Fe	[154]
Zn	Co	2-methylimidazole	900 (Ar)	Single-atom Co	[154]
Zn	Fe, Co	2-methylimidazole	900 (Ar)	$FeCoN_x$	[154]
Zn	Fe	2-methylimidazole	950 (Ar)	FeN_x	[71]
Zn	Fe	2-methylimidazole	1100 (N_2)	FeN_4	[59, 155, 156]
Zn	Co	2-methylimidazole	1050 (Ar)	FeN_4	[72]
Zn	Mn	2-methylimidazole	1100 (N_2) – 900 (N_2)	MnN_4	[27]
Zn	Co	2-methylimidazole	900 (N_2)	CoN_4	[62]
Zn	Mn	2-methylimidazole	800 (Ar) – 1100 (Ar) – 1100 (Ar)	MnN_4	[157]
Zn	Fe	2-methylimidazole, 2-undecylimidazole	1100 (N_2)	FeN_4	[156]
Zn	Fe	2-methylimidazole, benzimidazole	1100 (N_2)	FeN_4	[156]
Zn	Fe	2-methylimidazole, 1,2,4-triazole	1100 (N_2)	FeN_4	[156]
-	Co	2-methylimidazole	800 (N_2)	CoN_x, C-encapsulated Co	[158]
Zn	Fe	benzimidazole	1100 (N_2)	-	[159]
Zn	Fe	2-methylimidazole	1050 (Ar) – 1050 (NH_3)	FeN_4	[5]
Zn	Fe	terephthalonitrile	900 (N_2)	FeN_x	[160]
-	Co	2-methylimidazole	750 (Ar) – 750 (NH_3)	-	[161]
Zn	Co	2-methylimidazole	1000 (Ar) – 950 (NH_3)	-	[161]

Table 3.1 (continued.)

Zn	Fe	2-methylimidazole	1050 (Ar)	FeN_xC_y	[162]
Zn	Co	2-methylimidazole	1050 (Ar)	CoN_xC_y	[162]
Zn	Cr	2-methylimidazole	950 (NH_3)	N-groups	[162]
Zn	Fe	2-methylimidazole	900 (N_2)	FeN_x	[163]
Zn	Fe	1,4,5,8-naphthalenetetracarboxylic anhydride	950 (Ar)	FeN_4	[164]
Zn	Fe	2-methylimidazole	1000 (N_2)	FeN_x	[165]
Zn	Fe	2-methylimidazole	950 (10% H_2/Ar)	FeN_4	[166]
-	Fe	1H-1,2,3-triazole	850 (N_2) – 800 (NH_3)	ε-Fe_2N	[167]
Zn	Co	2-methylimidazole	1100 (N_2)	CoN_4	[168]
Zn	Fe	2-methylimidazole	900 (N_2)	-	[169]
Zn	Co	2-methylimidazole	900 (N_2)	-	[169, 170]
Zn	Fe, Co	2-methylimidazole	900 (N_2)	-	[169]
Zn	Co	2-methylimidazole	1000 (Ar)	CoN_3 nanoparticles	[171]
Zn	Fe	2-methylimidazole, 1,3,5-benzenetricarboxylic acid	1000 (N_2) – 800 (NH_3)	Fe/Fe_3C, Fe-N-C	[172]
Zn	Fe	2-methylimidazole	900 (Ar)	FeN_x, thiophene S	[173]

Table 3.1 highlights some of the more commonly used MOF precursors in the synthesis of non-PGM electrocatalysts. Zinc has proven to be a favorable SM in generating highly active MOF-derived non-PGM electrocatalysts for the ORR. As such the majority of electrocatalysts synthesized from MOF precursors rely on zinc. However, as a result, this imposes a limit on the temperature used during synthesis. To overcome this, we turned towards tuning the sacrificial metal in an effort to promote greater homogeneity in the active structures within the electrocatalyst. In our work, we explored the use of alternative metal elements other than zinc to synthesize non-PGM ORR electrocatalysts, which are named as of M-MOF_T where M is the sacrificial metal element (zinc, cadmium, etc.) and T is the pyrolysis temperature. Our initial goal was to identify the role of zinc as a SM by comparing it to an alternative metal. As shown in **Figure 3.2**, several metals were considered based on their bulk boiling points. Cadmium was a good choice given its

relatively low boiling point and ability to incorporate into a MOF structure.[174-176] The low boiling point may provide an opportunity to carry out the pyrolysis at lower temperatures which may reduce the formation of nanoparticles while still generating single-atom iron sites.

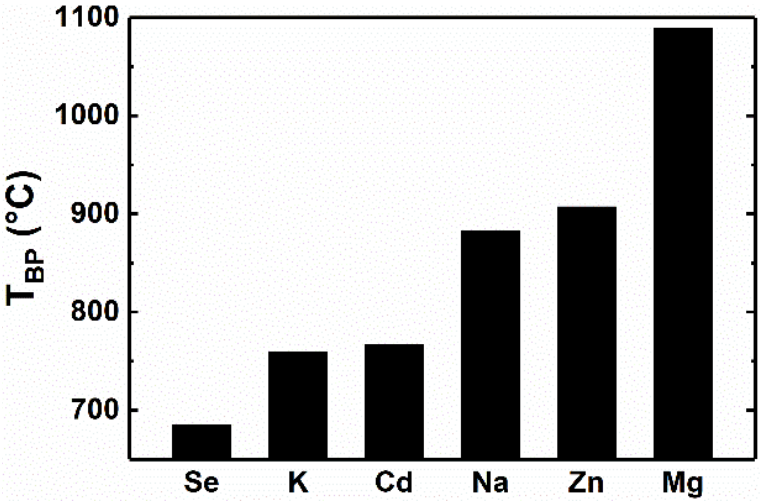

Figure 3.2 Bulk boiling point temperatures of several metal elements.

3.2 Experimental design

Our experimental design was a multistep process. Initially, we developed syntheses for crystalline MOFs using different metal salts and organic precursors. Subsequent pyrolysis transformed these MOFs into carbon-based electrocatalysts. Similar to Chapter 2, we used characterization techniques to determine the chemical and physical properties of the electrocatalyst. Lastly, we compared the catalytic activity to explore the structure-property relationship of our materials.

The aim of this project was to elucidate the role of the SM in the synthesis of MOF-derived non-PGM electrocatalysts. In this context, we compiled candidate elements which were viable to serve this role and synthesized the MOFs. The experimental design was as follows:

- Confirm MOF crystallinity using powder X-ray diffraction (PXRD).
- Convert MOF into carbon-based electrocatalyst and investigate the temperature limitations on the MOF-derived non-PGM electrocatalysts for different SMs used.

For our study we chose pyrolysis temperatures between 750 and 950 °C. This was based on our previous work where 750 °C represented a practical lower limit due to the large amount of zinc remaining leading to an inactive electrocatalyst for the ORR whereas the most active electrocatalyst was synthesized at 950 °C.

3.3 Experimental methods

3.3.1 Material synthesis

Synthesis of novel Cd-based MOF (Cd-Fe-DABCO-TPA). **Figure 3.3** depicts the overall synthetic setup for the MOF Cd-Fe-DABCO-TPA. In a normal synthetic procedure, the dual-ligated Cd-Fe-DABCO-TPA MOFs were made by mixing $Cd(NO_3)_2{\cdot}4H_2O$ (0.498 g), $Fe(NO_3)_3{\cdot}9H_2O$ (0.0082 g) and 1,4-diazabicyclo[2.2.2]octane (0.5482 g) in 15 mL of the solvent dimethylformamide. The above mixture was allowed to react in a 50 mL three-neck flask at 150 °C using a magnetic stirrer/hot plate (VWR, Cat. No. 97042-714). In a separate beaker, terephthalic acid (803.4 mg) was first entirely dissolved in 10 mL of dimethylformamide at 150 °C before being poured into the above three-neck flask. Afterwards, an additional 10 mL of dimethylformamide was added

subsequently into the beaker to dissolve any residual terephthalic acid and then transferred into the three-neck flask to bring the total volume of the mixture to 35 mL. The flask was sealed using two stoppers and was placed in a home-made aluminum heating block which was preheated to 150 °C. A condenser was connected to the top of the flask. The reaction was carried out for 2 h at this temperature and a stirring rate of 400 rpm. After a reaction time of 2 h, the condenser was removed and the dimethylformamide was allowed to evaporate over a 12 h period. The resulting MOF product was collected and washed with a total of 65 mL of hot dimethylformamide (~150 °C) three times, followed by centrifuging at 9000 rpm (Beckman Coulter Inc., Allegra X-30 Series) until a clear supernatant was obtained. The product was then dried at 80 °C under vacuum overnight to obtain the final Cd-Fe-DABCO-TPA MOF product.

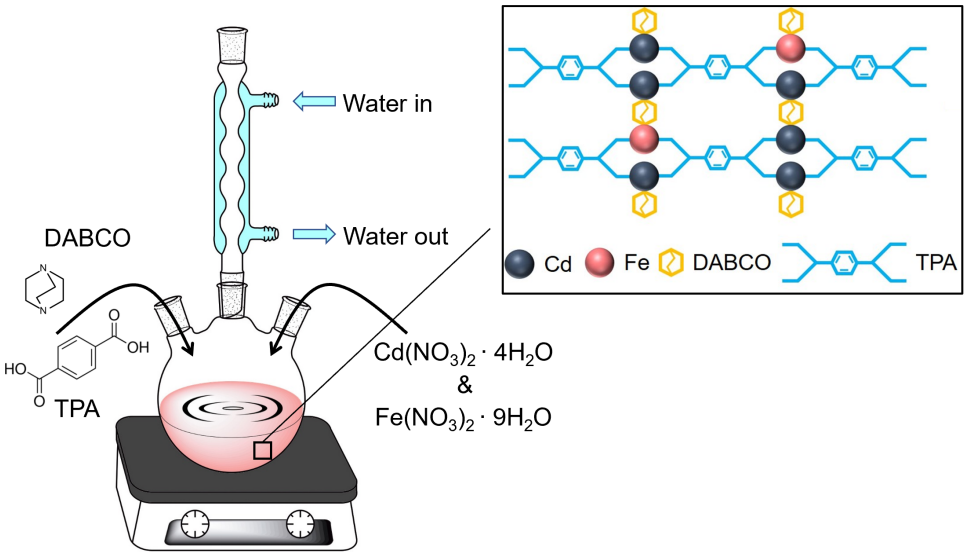

Figure 3.3 Schematic of the typical synthetic procedure to make Cd-Fe-DABCO-TPA MOF.

Synthesis of MOF-derived non-PGM electrocatalyst (Fe-C-N_T). To synthesize the non-PGM Fe-C-N_T electrocatalyst, the as-made Cd-Fe-DABCO-TPA MOF precursor (600 mg) was ball-milled

with 1, 10-phenanthroline (150 mg) in a 12-mL agate crucible equipped with five 12-mm balls of the same material for 2 h in a rotary ball mill (Fritsch Planetary Micro-Mill, Pulverisette 7"). The ground powder was collected and transferred to an alumina combustion boat (Sigma Aldrich, 5 mL). The flash pyrolysis technique was used in the synthesis of Fe-C-N_T. This combustion boat was then placed inside of a quartz tube (I.D.: 22 mm, O.D.: 25 mm, and length: 0.6 m), and purged with ammonia for about 95 min. After the purge, the tube was inserted into a tube furnace (Thermo Fisher Scientific™, Lindberg/Blue M™ Mini-Mite™) that was preheated to either 750 °C or 950 °C, and kept at this temperature for 15 min. After the reaction, the quartz tube was removed from the furnace and allowed to cool to room temperature under the flow of ammonia. The final product was collected and ground using a mortar and pestle to obtain the final electrocatalyst labeled as Fe-C-N_{750} or Fe-C-N_{950}.

3.3.2 Material characterization

Scanning electron microscopy (SEM) images were acquired at an accelerating voltage of 10 kV using a Hitachi S4700. SEM sample preparation involved the direct placement of catalysts onto a piece of carbon tape then onto a sample holder. Transmission electron microscopy (TEM) micrographs were acquired at an accelerating voltage of 200 kV using a JEOL 2100 Cryo TEM. TEM sample were prepared as follows: catalyst materials were dispersed in ethanol to create a translucent solution, next a few drops of solution were deposited onto carbon-coated TEM grids and allowed to dry. Powder x-ray diffraction (PXRD) patterns were acquired using a Rigaku Miniflex 600 with a Cu Kα radiating source. Typically, a continuous scan was performed between 10 and 80° 2θ. Scanning transmission electron microscopy (STEM) images and electron energy dispersive loss spectroscopy (EELS) were acquired at an accelerating voltage of 80 kV using a Thermo Fisher Scientific Themis Z advanced probe aberration corrected analytical TEM/STEM.

Images were obtained in a monochromated STEM mode with a 1.2 Å probe size, 0.3 eV energy spread, 30 mrad convergence angle, and approximately 20 pA probe current. The ADF-STEM image is lightly smoothed to decrease noise. EELS spectra were obtained on a Gatan imaging filter (GIF Quantum 965) with 0.25 eV dispersion and 25 mrad collection angle. The EEL spectrum was obtained by continuously scanning the electron beam over an area similar to the ADF-STEM image and summing multiple EEL spectra. Each spectrum was acquired at a 0.2-s dwell and a total S4 of 1400 frames were summed up to obtain the final EEL spectrum. For the inset Fe-$L_{2,3}$ edge, a power-law background subtraction was performed in Matlab and a Savitksy-Golay filter was applied to increase the signal to noise ratio. Samples were prepared using the same method outlined above for the TEM samples. Inductively coupled plasma mass spectrometry (ICP-MS) analysis was carried out on a PerkinElmer NexION 350D system. Brunauer-Emmett-Teller (BET) surface area analysis was performed using a Micromeritics 3Flex Analyzer and SmartVac Degasser. X-ray absorption spectroscopy (XAS) was performed in transmission mode using beamline 20-BM-B at the Advanced Photon Source (APS) at Argonne National Laboratory. Sample pellets were prepared by pressing ~20 mg of the catalyst and an equal amount of boron nitride powders using a benchtop manual press and 6 mm pellet die (Carver, Inc). The obtained XAS data were analyzed using the Athena software. Mössbauer analysis was performed with a Co^{57} source emitting gamma rays at 14.4 keV on a constant acceleration spectrometer at 300 K. X-ray photoelectron spectroscopy (XPS) was performed using a Kratos Axis ULTRA with an Al Kα monochromatic X-ray source to determine the binding energy of nitrogen in each of the catalyst samples.

3.3.3 Electrochemical analysis

A three-electrode setup was used to evaluate the oxygen reduction reaction (ORR) activity of these electrocatalysts. A graphite rod (Pine, MPGRR250) was used as the counter electrode and a

reversible hydrogen electrode (Hydroflex™, ET070 eDAQ) was used as the reference electrode. The working electrode was prepared using the following procedure: 5 mg of the catalyst was dispersed in a solvent containing 235 μL of deionized (DI) water (18.2 MW·cm, Thermo Fisher Scientific™, Barnstead™ E-Pure™), 235 μL of ethanol (200 Proof, Decon Labs, Inc.), and 45 μL of Nafion binder (D521 alcohol based 1100 EW at 5% weight, Nafion™ Store) to create an ink mixture. This ink mixture was sonicated for 30 min prior to drop-casting onto the surface of a glassy-carbon rotating-disk electrode (RDE). A total of 20 μL of the ink was deposited onto the surface of RDE in two equal portions of 10 μL. After the first deposition of 10 μL, the ink was given 10 min to dry, followed by the deposition another 10 μL to create a thin film catalyst layer on the electrode surface. The ORR performance of the catalysts was tested in 0.1 M perchloric acid ($HClO_4$) electrolyte (70% Veritas Double Distilled, GFS Chemicals) using a standard three-electrode system. Oxygen gas (Airgas Inc., 99.999%) was bubbled through the electrolyte for a total of 40 min prior to the RDE testing. Prior to the measurements, the catalysts underwent a conditioning step *in situ* by sweeping between 0.0 V and 1.1 V versus RHE at a step of 0.01 V for a total of two times using linear sweep voltammetry (LSV). Staircase voltammetry (SCV) was carried out between 0.0 V and 1.1 V at an interval of 0.02 V and a step period of 30 s to obtain the polarization curves.

3.3.4 Membrane electrode assembly testing

The membrane electrodes were fabricated using a previously reported method.[177] The catalyst inks were prepared by sonicating a mixture of catalyst, ionomer dispersion (Aquivion® D83-24B, EW 830 g mol^{-1} SO_3H, Sigma-Aldrich), DI-water and isopropanol (Fisher Chemical, >99.5%) in an ultrasonic bath for 3 h. The 5 cm^2 membrane electrode assembly (MEA) was fabricated by first hot-pressing a Pt anode (gas diffusion electrode, 40% Pt on Vulcan® carbon, 0.3 mg_{Pt} cm^{-2},

Sigracet® 29 BC carbon fiber paper) to one side of a Nafion® NR-211 membrane at a temperature of 120 °C and a pressure of 5.3 MPa for 5 min. The catalyst ink was then brush-painted to the cathode side of the membrane at ~80 °C to achieve predetermined catalyst loadings of ca. 4.8 or 6.8 mg cm^{-2}. The full MEA was assembled with a gas diffusion layer (GDL, Sigracet® 29 BC carbon fiber paper) covering the cathode catalyst layer. Two PTFE gaskets were used for sealing the MEA in the cell hardware at ca. 75% to 80% of its original thickness. The H_2/O_2 fuel cell performance was measured at 80 °C, using fully humidified gases. The partial pressure of H_2 at the anode and the partial pressure of O_2 at the cathode was maintained at 1.0 bar. The flow rate of H_2 was set at 200 sccm. For the MEA with catalyst loading of 4.8 mg cm^{-2} and 35 wt.% of D83 ionomer, the flow rate of O_2 was 500 sccm. For the MEA with catalyst loading of 6.8 mg cm^{-2} and 45 wt.% of D83 ionomer, the flow rate of O_2 was 200 sccm. The polarization plots were recorded from an open cell voltage (OCV, ca. 0.96 V) to 0.2 V at steps of 0.02 V with a step period of 10 s.

3.4 Results and discussion

3.4.1 Characterization of novel Cd-based MOF (Cd-Fe-DABCO-TPA)

Scanning electron microscopy (SEM) was used to characterize the morphology of the newly produced MOF. **Figure 3.4** is an SEM image of the as-synthesized Cd-Fe-DABCO-TPA MOF precursor. It is shown to have an orthorhombic structure with a long-edge length between 5 to 7 μm with a fairly uniform distribution. To compare the effect due to the addition of iron on the resulting MOF morphology, an iron-free Cd-DABCO-TPA MOF was prepared. The iron-free Cd-DABCO-TPA MOF displayed a similar morphology to its iron-containing counterpart, suggesting that there was no change in the type of MOF structure following the addition of iron (**Figure 3.5**).

The PXRD pattern of Cd-Fe-DABCO-TPA MOF in **Figure 3.6** shows the presence of sharp peaks at low 2θ angles indicating a highly crystalline sample characteristic of a MOF structure. Inductively coupled plasma mass spectrometry (ICP-MS) results revealed that the Cd-Fe-DABCO-TPA MOF prior to pyrolysis contained 18.03 wt. % of cadmium and 0.18 wt. % of iron. These results suggested that we had obtained a material with a high degree of crystallinity composed of cadmium as the sacrificial metal and iron as the active metal.

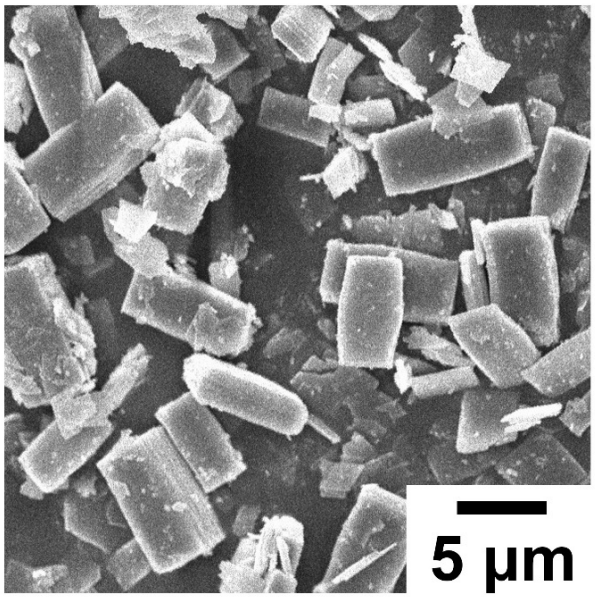

Figure 3.4 SEM image of as-synthesized iron-containing Cd-DABCO-TPA precursors.

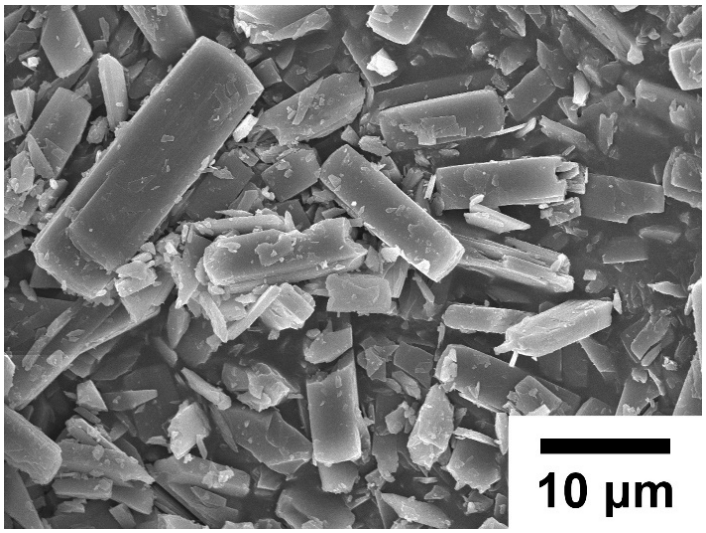

Figure 3.5 Representative SEM image of as-synthesized Cd-DABCO-TPA MOF (without iron).

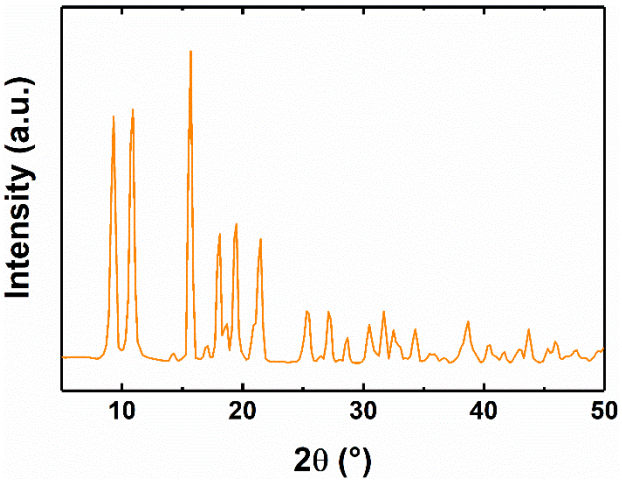

Figure 3.6 PXRD pattern of as-synthesized Cd-Fe-DABCO-TPA MOF.

3.4.2 Characterization of MOF-derived non-PGM electrocatalyst (Fe-C-N_T)

The SEM image shown in **Figure 3.7** of the as-synthesized electrocatalyst Fe-C-N_{750} revealed a change in the precursor morphology; the MOF crystals observed earlier had decomposed into

irregular shapes after the pyrolysis. This suggested that at 750 °C a breakdown of the MOF occurred giving away to an amorphous-like structure. PXRD shows a broad peak for both Fe-C-N_{750} and F-C-N_{950} catalysts (**Figure 3.8**). The broad peak centered around 25° 2θ is from the nitrogen-doped carbon matrices. For Fe-C-N_{750}, the peak centered near 43° 2θ could be assigned to the (101) plane of the 2H phase graphite. For the Fe-C-N_{950} catalyst, two additional narrow peaks appeared at 40.8° and 42.9° 2θ. The two narrow diffractions for Fe-C-N_{950} sample are likely from the small amount of iron nitride (Fe_2N), which forms only at relatively high temperatures and is magnetically active. These results agreed with previously studies which showed metal nitrides could form under high temperature treatments with ammonia.[178]

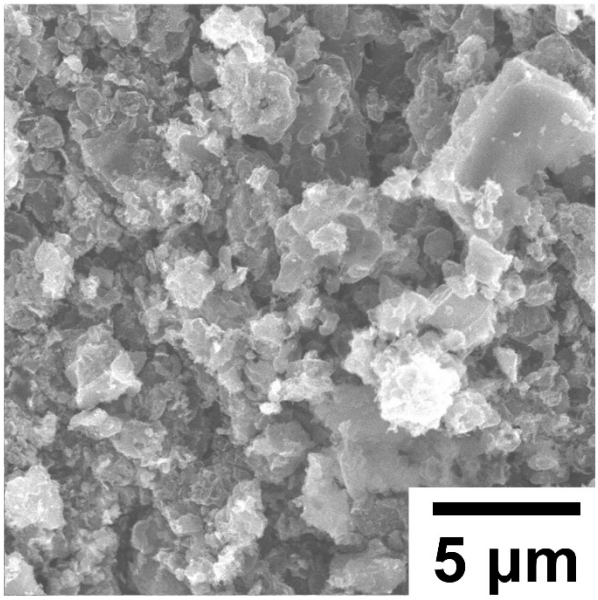

Figure 3.7 SEM micrograph of the Fe-C-N_{750} non-PGM electrocatalyst.

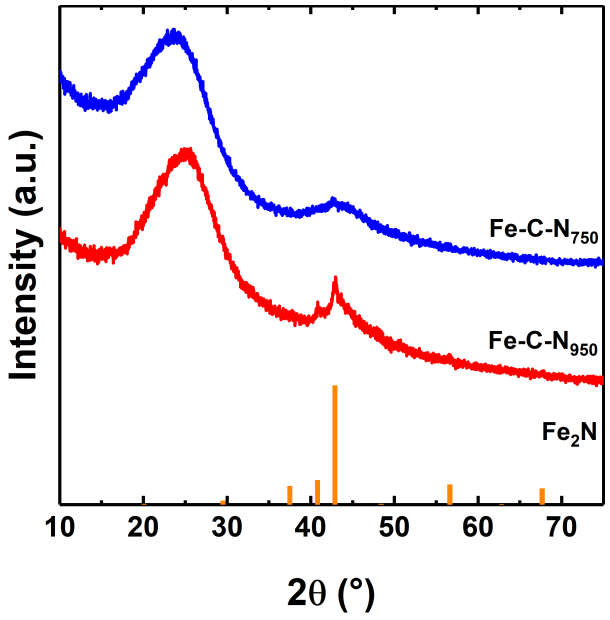

Figure 3.8 PXRD patterns of both Fe-C-N_{750} and Fe-C-N_{950} non-PGM electrocatalysts indicating the lack of metallic Fe in both samples.

Transmission electron microscopy (TEM) images were taken to examine the detailed morphology of the electrocatalysts. The TEM study revealed that the MOF crystals transformed into amorphous- and flake-like products after pyrolysis (**Figure 3.9a, b**). ICP analysis showed that the Fe-C-N_{750} electrocatalyst contained 0.4 wt. % of cadmium indicating a near complete removal of the SM after the pyrolysis. This is starkly different to the Fe-C-N_{750} sample which contained near 15.4 wt. % of the SM post pyrolysis. This difference could largely be attributed to the difference in bulk boiling point temperatures between the two SMs, which is 767 °C for cadmium, and 907 °C for zinc. Thus, at a low pyrolysis temperature (750 °C), the electrocatalysts derived from the cadmium exhibited the necessary high specific surface area, active structures needed, while zinc-based materials such as ZIF-8 generally required higher temperatures for the removal of the SM and the formation of the necessary Fe-C-N structures as the active catalysts.

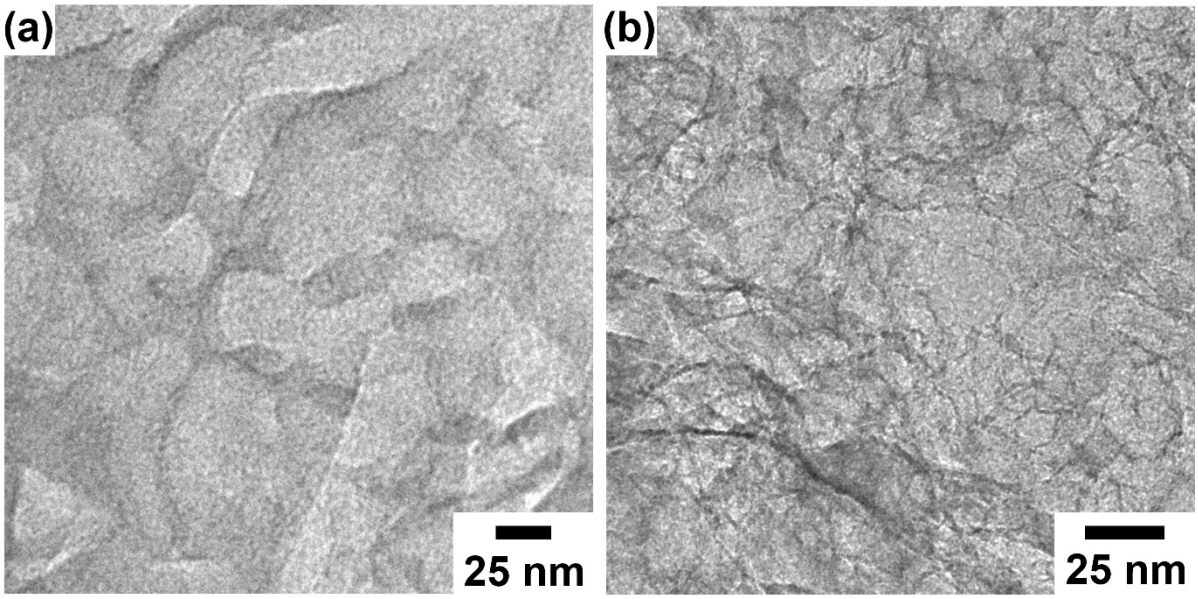

Figure 3.9 TEM images of (a) Fe-C-N_{750} (b) Fe-C-N_{950} non-PGM electrocatalysts.

Figure 3.10 shows the nitrogen gas isotherm of these two non-PGM electrocatalysts. The Brunauer-Emmet-Teller (BET) analysis exhibited a specific surface area of 431 m^2 g^{-1} for Fe-C-N_{750} and 869 m^2 g^{-1} for Fe-C-N_{950}. Besides increased surface area, the Fe-C-N_{950} catalyst also showed a hysteresis in the isotherm and the Type IV adsorption-desorption curve, characteristic of a mesoporous material. The Barrett-Joyner-Halenda (BJH) analysis indicated the Fe-C-N_{950} catalyst contained mesoporous structures with pore diameters centered at 3.7 nm and 23 nm, respectively. Our results indicated that the formation of pore structures is temperature-dependent; at high temperatures a greater amount of volatile compounds were removed, leading to the development of high surface area and large pore diameters. Mossbauer spectroscopy was used to confirm the types of iron structures present in both samples. **Figure 3.11** shows the Mossbauer spectra for both Fe-C-N_{750} and Fe-C-N_{950}. Aside from the presence of iron-nitrogen moieties (FeN_x

and Fe_xN) within both samples, there is a single peak in the spectra of Fe-C-N_{950} indicative of the presence of superparamagnetic α-iron species. The Mossbauer fitting results are summarized in **Table 3.2**. Unlike several materials[32, 33], however, carbide species and are not present for either Fe-C-N_{750} or Fe-C-N_{950}. This could possibly be attributed to the lower overall iron content within these catalysts which based on ICP results was found to be 0.8 wt.% for the low temperature sample and 3.1 wt.% for the high temperature sample.

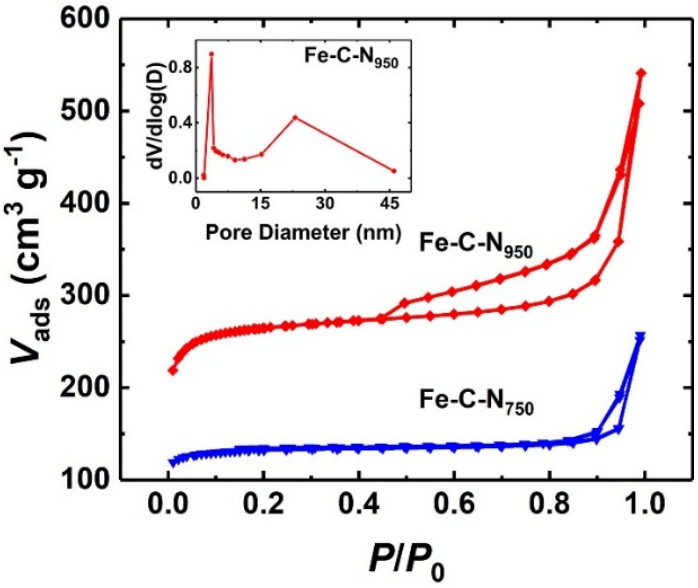

Figure 3.10 Nitrogen isotherm analysis of the two non-PGM electrocatalysts Fe-C-N_{750} and Fe-C-N_{950}. Inset shows the pore size analysis of the Fe-C-N_{950} electrocatalyst by the BJH method.

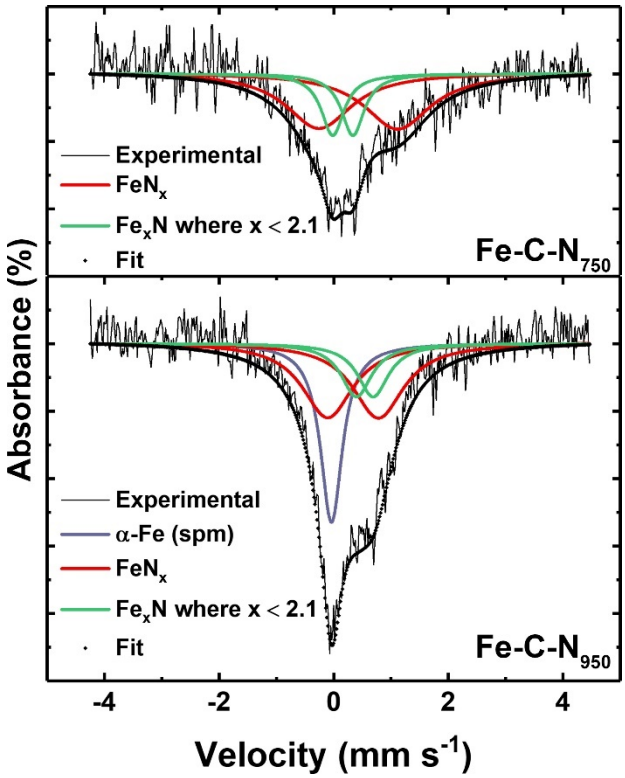

Figure 3.11 Mossbauer spectra for Fe-C-N_{750} and Fe-C-N_{950}.

Table 3.2 Mossbauer fitting results for the Fe-C-N_{750} and Fe-C-N_{950}.

Sample	Component	δ_{iso} (mm s^{-1})	ΔE_Q (mm s^{-1})	FWHM (mm s^{-1})	Absorbance (%)	Assignment
Fe-C-N_{750}	Doublet 1	0.43	1.37	1.38	27.3	FeN_4
	Doublet 2	0.16	0.35	0.48	72.7	Fe_xN ($x < 2.1$)
Fe-C-N_{950}	Doublet 1	0.34	0.88	1.07	51.7	FeN_4
	Doublet 2	0.54	0.29	0.65	22.0	Fe_xN ($x < 2.1$)
	Singlet	-0.04	-	0.46	26.3	spm α-Fe

To further confirm the presence of superparamagnetic species in Fe-C-N_{950} and lack thereof in Fe-C-N_{750}, vibrating-sample magnetometry (VSM) was used. As shown in **Figure 3.12**, Fe-C-N_{950} exhibits superparamagnetic behavior as indicated by its rapid initial response to the applied magnetic field, whereas Fe-C-N_{750} depicts paramagnetic behavior, judging by its linear response. The absence of hysteretic behavior further suggests the lack of ferromagnetic structures. A high-resolution STEM study was performed with both Fe-C-N_{750} and Fe-C-N_{950} catalysts using the probe aberration-corrected analytical STEM/TEM (**Figure 3.13**). The images show that Fe-C-N_{750} contains an even-dispersion of single-atom moieties throughout the catalyst (**Figure 3.13a**), while Fe-C-N_{950} contains both single-atoms and clusters of such single atoms (**Figure 3.13b**). In some regions, such atoms sintered to form loose metal clusters.

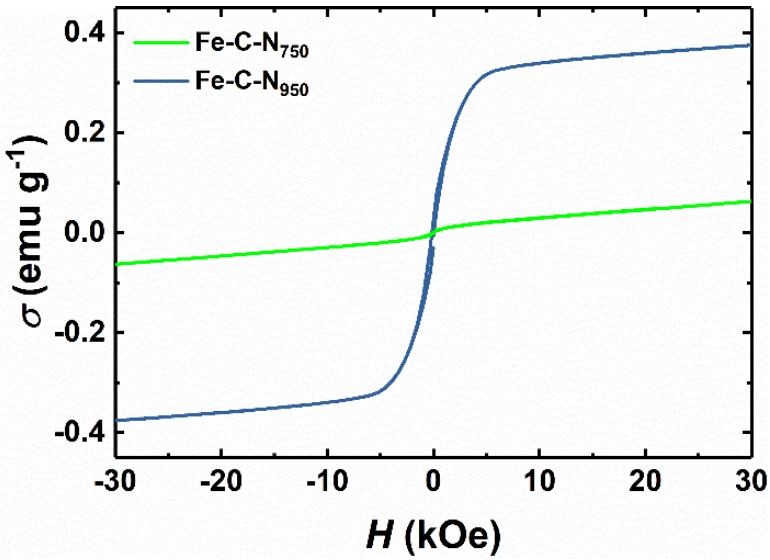

Figure 3.12 VSM data at 300 K showing the magnetization of both Fe-C-N_{750} and Fe-C-N_{950}.

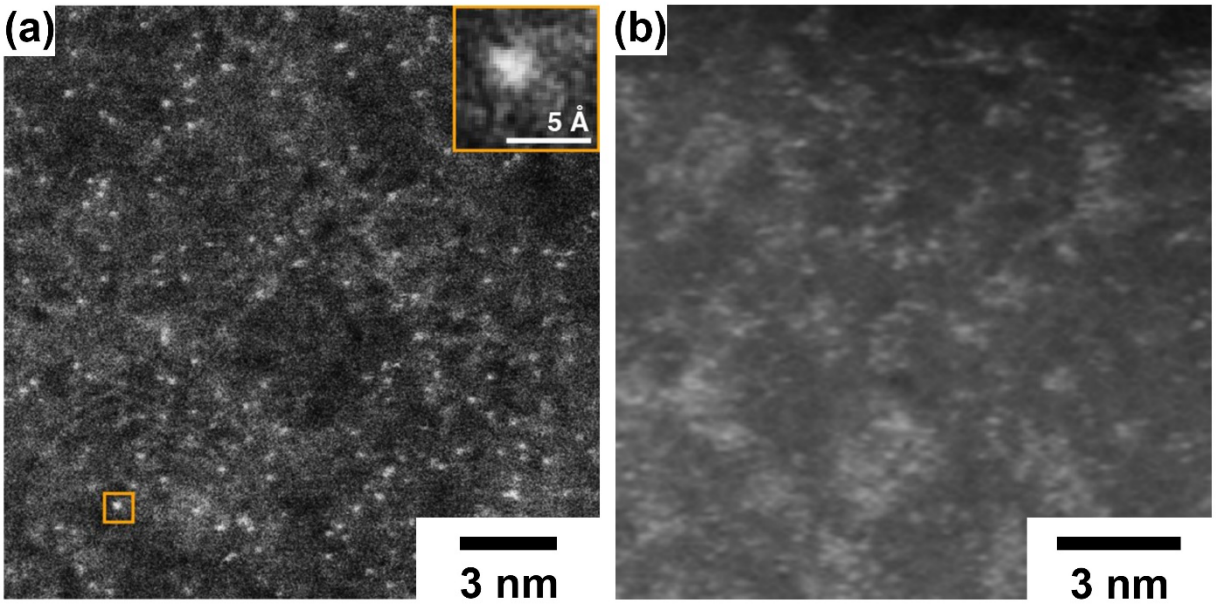

Figure 3.13 ADF-STEM micrographs of (a) the Fe-C-N_{750} electrocatalyst showing the even dispersion of a large number of single atoms and (b) the Fe-C-N_{950} catalyst showing the clustering of single Fe atoms.

In the EELS spectra (**Figure 3.14**) of Fe-C-N_{750}, the intensity of the iron $L_{2,3}$ edge is weak but is detectable (inset of **Figure 3.14**). The weak signal is due to a relatively low scattering cross-section and the relatively small amount of iron in the catalyst. The metallic sites in the Fe-C-N_{750} electrocatalyst are evenly dispersed and exhibit a dense population. Our data suggests that the use of cadmium as a SM can drive down the temperature of pyrolysis, which contributes to the formation of a high density of single-atom structures and subsequently the ORR activity observed in the Fe-C-N_{750} electrocatalyst.

X-ray absorption spectroscopy (XAS) as well as X-ray photoelectron spectroscopy (XPS) were used in conjunction with one another to study both the bulk and surface properties of the Fe-C-N_{750} and Fe-C-N_{950} non-PGM electrocatalysts. XAS affords a wealth of information including,

oxidation state by examining the near-edge region (XANES) and interatomic distances by examining the region beyond the edge (EXAFS). Specifically, analysis of the iron K-edge can provide information pertaining to its oxidation state. However, because of the heterogeneity of the iron structures present in our materials, as shown in previous characterizations, most analyses should be made comparatively rather than absolutely.[59, 179] **Figure 3.15** show the XANES of Fe K-edge region for both Fe-C-N_{750} and Fe-C-N_{950} electrocatalysts and the corresponding references. The results indicate that the oxidation states of Fe single atoms in these two Fe-C-N ORR catalysts lied in between 0 (Fe foil) and +2 (FeO) or +3 (Fe_2O_3). In the case of Fe-C-N_{950}, there was an apparent shift of the oxidation state to a lower energy in the Fe K-edge as compared to that of Fe-C-N_{750} (**Figure 3.16b**); this suggests that the metallic iron clusters led to an overall decrease in the bulk oxidation state of iron.

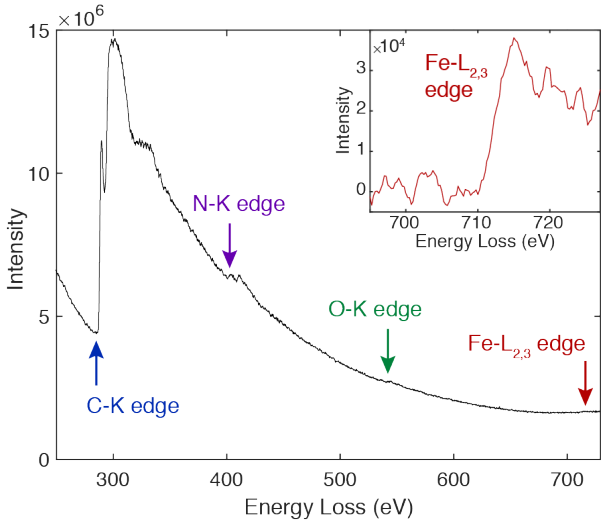

Figure 3.14 EEL spectrum showing the presence of carbon, nitrogen, oxygen, and iron. (inset) Background subtracted spectrum of Fe-$L_{2,3}$ edge. The inset spectrum was smoothed using a Savitsky-Golay filter to improve the signal to noise ratio

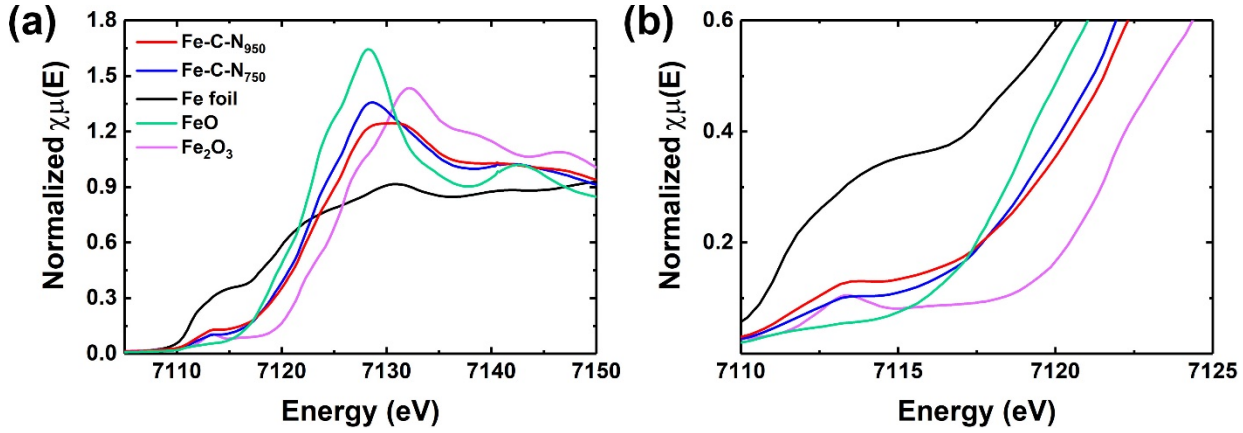

Figure 3.15 (a) Normal and (b) enlarged XANES for the Fe K-edge (including the references) for the Fe-C-N_{750} and Fe-C-N_{950} non-PGM electrocatalysts.

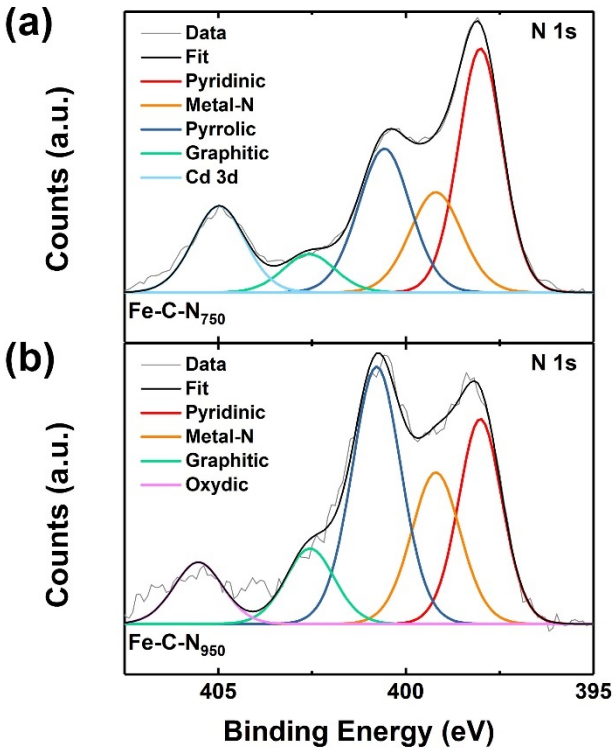

Figure 3.16 XPS analysis of the N 1s regions for the Fe-C-N_{750} and Fe-C-N_{950} non-PGM electrocatalysts.

XPS was used to characterize the nitrogen binding present in these Fe-C-N ORR electrocatalysts (**Figure 3.16**). A trace amount of cadmium was detected only for the Fe-C-N_{750} catalyst and contributed to the overlapping peaks observed in the N 1s spectra. Both the Fe-C-N_{750} and Fe-C-N_{950} samples show nitrogen peaks pertaining to the pyridinic and pyrrolic species. Such nitrogen structures were attributed to the high activity observed in non-PGM electrocatalysts.[93] The presence of metal-nitrogen peaks in both Fe-C-N_{750} and Fe-C-N_{950} electrocatalysts is indicative that single atomic moieties are strongly coordinated. **Table 3.3** summarizes the binding energies of the various nitrogen moieties.

Table 3.3 X-ray photoelectron spectroscopy analyses of the nitrogen species in the Fe-C-N_T electrocatalysts

Sample	Binding Energy (eV)				
	Pyridinic	Metal-N	Pyrrolic	Graphitic	Oxydic
Fe-C-N_{750}	398.0	399.2	400.6	402.6	-
Fe-C-N_{950}	398.0	399.2	400.8	402.6	405.5

3.4.3 ORR performance analysis of MOF-derived non-PGM electrocatalyst (Fe-C-N_T)

Figure 3.17a shows the staircase voltammetry (SCV) curves for Fe-C-N_{750} with a half-wave potential of 0.70 V vs RHE while that of ZIF-8/Fe_{750} was essentially inactive. The results of the Koutecky-Levich analysis indicates that the Fe-C-N_{750} electrocatalyst promotes the $4e^-$ pathway (**Figure 3.18b.**). Notably, Fe-C-N_{750} yielded significantly higher activity over ZIF-8/Fe_{750} (which relied on zinc as the SM). As mentioned earlier, ICP-MS analysis revealed that Fe-C-N_{750} contained 0.4 wt. % cadmium after pyrolysis while ZIF/Fe_{750} retained a greater amount of zinc and contained around 15.4 wt. %. The difference in boiling point may result in the largely reduced amount of sacrificial metals even at low pyrolysis temperature and subsequently a reduction in the measured electrocatalytic activity. However, at a higher pyrolysis temperature of 950 °C, the Fe-N-C_{950} electrocatalyst exhibited similar activity to ZIF-8/Fe_{950} with a half-wave potential of 0.80 V. This result highlighted the importance of the SM which not only effects the physical properties

of the electrocatalyst but also regulates the structures formed under pyrolysis both of which impact performance.

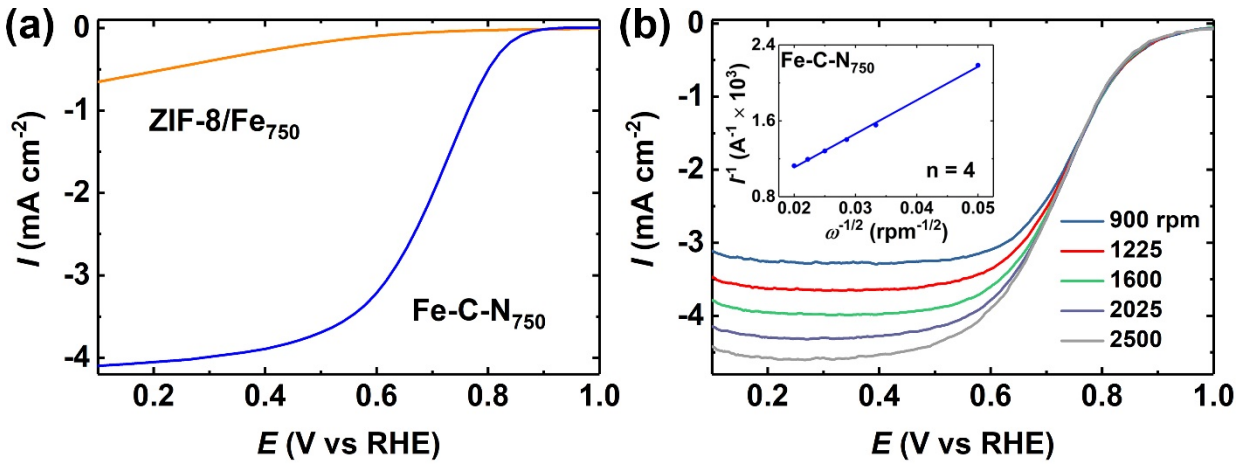

Figure 3.17 (a) Staircase voltammogram and (b) Koutecky-Levich analysis of the Fe-C-N_{750} electrocatalyst. The polarization curve for ZIF-8/Fe_{750} catalyst was measured for comparison.

At a higher temperature of 950 °C, Fe-C-N_{950} exhibited a half-wave potential of 0.80 V which is 100 mV greater than that of Fe-C-N_{750} and promoted a $4e^-$ reduction pathway as determined by a Koutecky-Levich measurement (**Figure 3.18a**). The catalyst operation within a membrane electrode assembly (MEA) system is quite different from its operation in a three-electrode setup. Thus, while a three-electrode setup is effective for evaluating the electrochemical performance on a fundamental level of catalysts with minimal interference of other phenomena, it is not seen as a suitable resource in evaluating a catalyst's practical application in fuel cells where other factors aside from intrinsic activity have a more pronounced influence on performance. These factors include: 1) reactant/product transport, 2) layer stability under high fuel cell operating conditions, and 3) water management. The membrane electrode assembly (MEA) testing was carried out to

assess the performance of the Fe-C-N_{950} non-PGM electrocatalyst under fuel cell operating conditions. The MEA consists of gas diffusion electrodes with the cathode layer made of non-PGM Fe-C-N_{950} ORR electrocatalyst. The anode and cathode layers were separated by a proton-conducting Nafion® NR-211 membrane. **Figure 3.18b and c** show the MEA performance in a single fuel cell using the testing protocols recommended by the US Department of Energy (DOE). The ionomer loadings were set at 35 wt.% and 45 wt.%, respectively, to evaluate the catalytic performance in both the kinetic region at low current densities and mass transport-limited region at high current densities. Our study shows that at the ionomer loading of 45 wt.%, the newly developed Fe-C-N_{950} electrocatalyst exhibited a current density of 44 mA cm^{-2} at a voltage of 0.87 V (iR-free), which is close to the DOE 2020 ORR catalyst performance target of 0.90 V. At the cell voltage of 0.80 V (iR-free), the MEA made with this Fe-C-N_{950} catalyst exhibited a current density of 157 mA cm^{-2}, surpassing some of the non-PGM electrocatalysts derived from the ZIF-8/Fe precursors (**Figure 3.18b**).[155] The power density reached 680 mW cm^{-2} for a single cell in the H_2/O_2 MEA testing (**Figure 3.18c**).

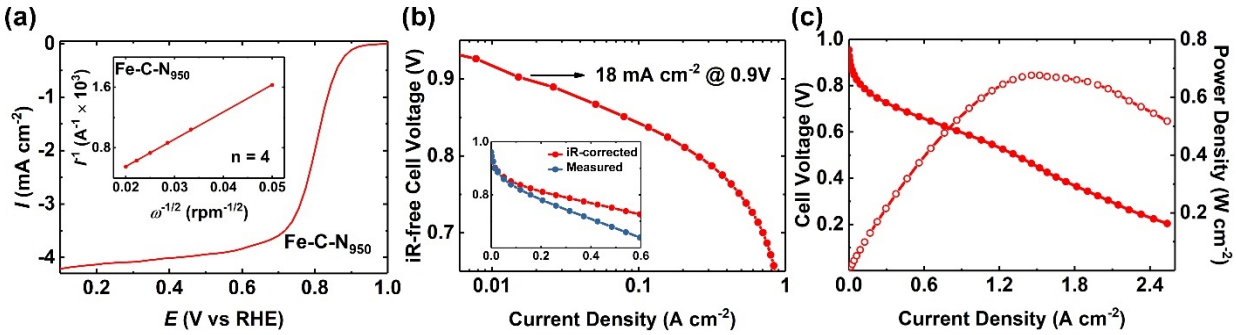

Figure 3.18 (a) Staircase voltammogram, (b) *iR*-free cell voltage and current density relationship, and (c) power density and current density relationship of the Fe-C-N_{950} non-PGM electrocatalysts in the MEA testing. The inset in (a) is the Koutecky-Levich analysis and the inset in (b) shows the difference between the as-measured and *iR*-corrected curves.

3.5 Summary and future considerations

In summary, through our work we sought to understand the effect of temperature on iron structure formation, specifically by impacting the removal of the SM. The synthesis of non-PGM electrocatalysts involves high temperature pyrolysis which has been shown to enhance the performance of these electrocatalysts.[180] Naturally, this high temperature pyrolysis has an impact on the resulting physical and chemical structure of non-PGM electrocatalysts. During pyrolysis two competing processes are at play: 1) sacrificial metal removal 2) diffusion of active metal species to coordinate with nitrogen or towards the formation of nanoparticle structures (sintering).[181] In an attempt to acquire greater control over structure formation during pyrolysis, our synthesis employed a technique known as flash pyrolysis in order to minimize the time the catalyst was exposed to the heat treatment as well as incorporating cadmium as the sacrificial metal in an effort to reduce the temperature at which to carry out pyrolysis. As shown in **Figure 3.19**,

further exposure to heat in addition to a higher temperature would increase the likelihood of reduced nanoparticle structures. By relying on cadmium as the SM, the pyrolysis temperature can further be reduced which can further restrict the amount of aggregation experienced by the active metal (iron).

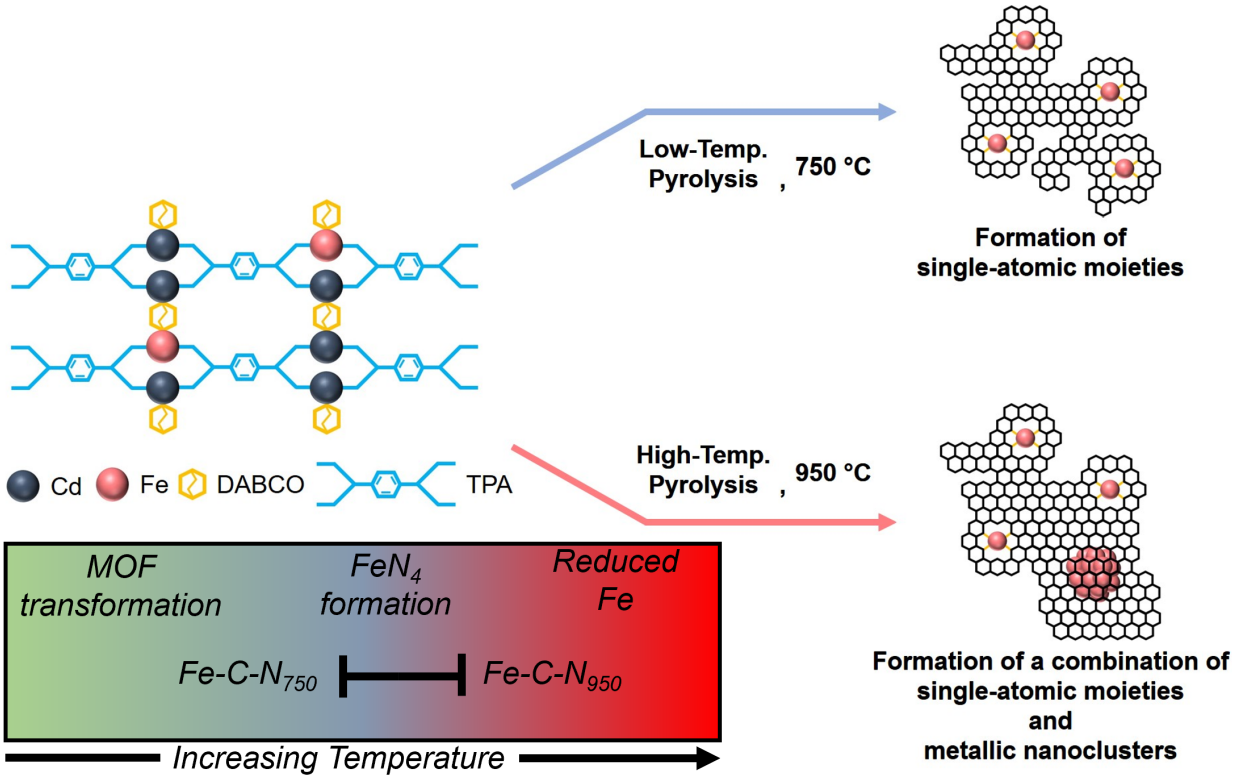

Figure 3.19 Schematic of the experimental design showing that a lower temperature favors the formation of single-atom iron moieties while a higher temperature leads to the formation of nanoparticle structures.

CHAPTER 4

CARBON AS AN IMMOBILIZING SUPPORT TO IMPROVE SINGLE ATOM MONO-DISPERSITY

4.1 Introduction

The ability to effectively disperse a precursor can determine the extent to which single atoms can be generated during synthesis.[182] Several different strategies have been developed for synthesizing single metal atom (Fe, Co) ORR electrocatalysts. These strategies typically involve using an atomically-dispersed precursor (ADP)[146] in the form of a polymer such as polyaniline[21, 28, 96, 183, 184] or a MOF[23, 59]. These precursors operate on the principle of spatial confinement; their regular, porous structures allow for a high dispersion of the active precursor throughout the lattice. The next stage a post treatment which typically involves the reduction of these metal precursors to form the metal single atom stabilized within the support matrix. In the case of non-PGM electrocatalysts derived from polymer or MOF precursors, this involves a carbonization process wherein the support is formed simultaneously from a decomposition of the organic precursors into a nitrogen doped-carbon support. A secondary approach relies on synthesizing the support matrix with defects followed by introducing the active metal precursor onto the defective support.[103, 185] The idea would be to leverage the defects as anchors to capture and stabilize single atom structures. This can effectively prevent single atom movement which can lead to agglomeration during the post-treatment process.

As previously discussed, MOFs are seen as suitable precursors because of their advantageous properties; most important of which is their capacity to disperse the active metal prior to pyrolysis, thus leading to the formation of a large density of single-atom sites by mitigating the effects of

sintering. In addition, controllable nitrogen doping through ligand exchange, resultant carbon structures and porosity after decomposition through pyrolysis make the MOF a front running precursor in the synthesis of non-PGM electrocatalysts. Secondary processing techniques including the utilization of organic coatings were also shown to be especially effective in promoting the dispersity of the metal precursor and be favorable towards the generation of single-atomic sites.[60, 62] It was also demonstrated that by varying the sacrificial metal, the activation temperature for catalyst precursors could also be altered, resulting in the formation of single atom active structures at a reduced temperature.[144]

In this chapter, we conducted a two-pronged approach: (1) the synthesis of a dual-ligated bimetallic MOF followed by (2) an immobilization process wherein the MOF was deposited and dispersed onto a Ketjen black carbon support and effectively immobilized on the surface of the support. The aim of this approach was to investigate the effect of this immobilization method in generating a greater density of single atoms.

4.2 Experimental design

In this study, we developed a strategy to synthesize single atom non-PGM electrocatalysts by taking into consideration the utilization of a catalyst support. In terms of the selection of MOFs (other than ZIF-8) for the preparation of non-PGM ORR electrocatalysts, a dual-ligated MOF with 1,4-diazabicyclo[2.2.2]octane (DABCO) as the N-containing ligand and terephthalic acid (TPA) a secondary ligand was chosen.[186, 187] Structurally, terephthalic acid coordinates to the metal atoms within the horizontal plane; the nitrogen-containing ligands serve as a column in the vertical plane to complete the three-dimensional structure. The use of a secondary ligand assists in metal

distribution throughout the MOF structure; specifically, the distance between the single atom active sites (iron) and the sacrificial metal (zinc) within the MOF can be further be distanced which can impact the distribution of single atoms post pyrolysis. The next stage involved the immobilization of the as-made MOFs onto a Ketjen black carbon support to distribute and anchor the MOF structures followed by pyrolysis. Following this design concept, we were able to obtain uniformly dispersed metal single atom sites throughout the MOF-derived non-PGM ORR electrocatalysts. **Figure 4.1** illustrates the synthetic route for the preparation of Fe-based atomically dispersed non-PGM electrocatalysts.

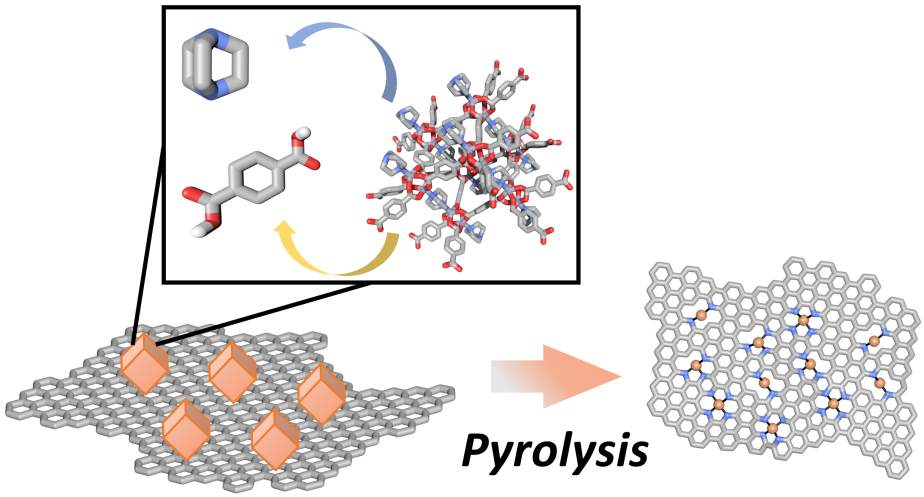

Figure 4.1 Synthetic pathway towards a dual-ligated MOF-derived non-PGM electrocatalyst a using the immobilization method

4.3 Experimental methods

4.3.1 Material synthesis

Synthesis of dual-ligated MOF Zn-Fe-DABCO-TPA. The synthesis of the dual-ligated MOF Zn-Fe-DABCO-TPA consisted of mixing weighed amounts of $Zn(NO_3)_2 \cdot 6H_2O$ (0.4485 g) and $Fe(NO_3)_3 \cdot 9H_2O$ (0.0154 g) along with 1,4-diazabicyclo[2.2.2]octane (0.5139 mg) were dissolved in 15 mL of dimethylformamide at 150 °C in a 50 mL three-neck flask. After the addition of a stir bar, the above mixture was given time to react in a using a magnetic stirrer/hot plate (VWR, Cat. No. 97042-714). In a separate beaker, terephthalic acid (761.1 mg) was completely dissolved in 10 mL of dimethylformamide at 150 °C before being poured into the three-neck flask. This was followed by adding an additional 10 mL of dimethylformamide into the beaker to capture any undissolved terephthalic acid and subsequently pouring it into the three-neck flask for a total of 35 mL. The off-center openings of the three-neck flask were sealed using two glass stoppers while the center opening was fixed with a reflux condenser. The mixture was then placed in a stirred oil bath to react. The reaction was given time to react over a 2 h period and a stir rate of 300 rpm. After that the condenser was removed to allow for the evaporation of dimethylformamide (~12 h). The product was then collected and washed several times with hot dimethylformamide followed by centrifugation at 9000 rpm (Beckman Coulter Inc., Allegra X-30 Series) until a clear supernatant was obtained. The product was then dried at 120 °C under vacuum overnight to obtain the final Zn-Fe-DABCO-TPA MOF product.

Synthesis of MOF-derived non-PGM electrocatalyst (Fe/C_T and Fe_T). To synthesize the non-PGM electrocatalyst Fe/C_T, the as-made MOF Zn-Fe-DABCO-TPA, 1, 10-phenanthroline and Ketjen black carbon were added at a ratio of 5:1:1 into a three-neck flask along with 30 mL

dimethylformamide. The off-center openings of the three-neck flask were sealed using two glass stoppers while the center opening was fixed with a reflux condenser. The mixture was stirred at 300 rpm and placed onto an aluminum block preheated to 150 °C. After a reaction time of 4 h the condenser was removed to allow for the evaporation of dimethylformamide. After 12 hours, the product was collected and ground into fine powder.

The ground powder was collected and transferred to a quartz boat (MTI, 100 mm L × 17 mm W × 10 mm H). This combustion boat was then placed inside of a quartz tube (I.D.: 22 mm, O.D.: 25 mm, and length: 0.6 m), and inserted into a tube furnace (Thermo Fisher Scientific™, Lindberg/Blue M™ Mini-Mite™). purged with argon for about 30 min. After the purge, the temperature was raised to a target temperature at a rate of 5 °C min^{-1} and kept at this temperature for 2 h. After the reaction, the temperature was lowered back to room temperature at a rate of 5 °C min^{-1}. The final product was collected and ground using a mortar and pestle to obtain the final electrocatalyst labeled as Fe/C_T. A reference electrocatalyst was synthesized following the same procedure omitting the use of a Ketjen black carbon support and the corresponding sample was labeled as Fe_T.

4.3.2 Material characterization

Scanning electron microscopy (SEM) images were obtained using a Hitachi S4700 at an acceleration voltage of 10 kV. SEM samples were prepared by directly placing catalysts onto the carbon tape on the sample holder. Transmission electron microscopy (TEM) micrographs were obtained using a JEOL 2100 Cryo with an accelerating voltage of 200 kV. TEM samples were prepared by dispersing catalysts in ethanol and depositing on carbon-coated TEM grids. Powder x-ray diffraction patterns were obtained using a Rigaku Miniflex 600 using Cu radiation to confirm

the lack of metallic iron formation during pyrolysis. Typically, a continuous scan was performed between 2θ = 10 to 80°. To determine the presence of iron single atoms, scanning transmission electron microscopy (STEM) images was obtained using a FEI Themis Z advanced probe aberration corrected analytical TEM/STEM at an accelerating voltage of 300 kV. Samples were prepared using the same method outlined for the TEM samples above. ICP-MS analysis was carried out on a PerkinElmer NexION 350D system to analyze the amounts of both zinc and iron to confirm the evaporation of zinc during pyrolysis and obtain the relative loading of iron in the final catalyst samples. Brunauer−Emmett−Teller (BET) surface area analysis was performed using a Quantachrome Nova 2000e BET Analyzer. XAS was performed to analyze the Fe K-edge of our catalyst samples in transmission mode using beamline 20-BM-B at the Advanced Photon Source (APS) at Argonne National Laboratory. Sample pellets were prepared by pressing the catalyst powders. The obtained XAS data were analyzed using the Athena and Artemis software. X-ray photoelectron spectroscopy (XPS) was performed using a Kratos Axis ULTRA with an Al Kα monochromatic x-ray source to analyze the binding energies of doped nitrogen in each of the catalyst samples.

4.3.3 Electrochemical analysis

A three-electrode setup was used to evaluate the oxygen reduction reaction (ORR) activity of these electrocatalysts. A graphite rod (Pine, MPGRR250) was used as the counter electrode and a reversible hydrogen electrode (Hydroflex™, ET070 eDAQ) was used as the reference electrode. The working electrode was prepared using the following procedure: 5 mg of the catalyst was dispersed in a solvent containing 300 µL of ethanol (200 Proof, Decon Labs, Inc.), and 60 µL of Nafion binder (D521 alcohol based 1100 EW at 5% weight, Nafion™ Store) to create an ink mixture. This ink mixture was sonicated for 30 min prior to drop-casting onto the surface of a

glassy-carbon rotating-disk electrode (RDE). A total of 16 μL of the ink was deposited onto the surface of RDE in two equal portions of 8 μL. After the first deposition of 8 μL, the ink was given time to dry, followed by the deposition another 8 μL to form a thin film catalyst layer on the glassy-carbon electrode surface at a loading of 1 mg cm^2. The ORR performance of the catalysts was tested in 0.1 M perchloric acid ($HClO_4$) electrolyte (70% Veritas Double Distilled, GFS Chemicals) using a standard three-electrode system. Oxygen gas (Airgas Inc., 99.999%) was bubbled through the electrolyte for a total of 40 min prior to the RDE testing. The catalysts were evaluated by linear-sweep voltammetry (LSV) between 0.0 V to 1.1 V at a step of 0.01 V in O_2-saturated 0.1 M $HClO_4$ at room temperature and a rotation rate of 900 rpm.

4.4 Results and discussion

4.4.1 Characterization of dual-ligated MOF Zn-Fe-DABCO-TPA

Figure 4.2 depicts an SEM image of the Zn-Fe-DABCO-TPA MOF. Iron was added as the active component metal in the zinc-based and exhibited an orthorhombic morphology. As seen in **Figure 4.2b** the long edge length lay in the range of 1 to 2 μm and was relatively uniform in distribution. The powder X-ray diffraction (PXRD) pattern shows the as-synthesized MOF precursor was highly crystalline judging by the sharp peaks at low angles of 2θ which are characteristic of a MOF structure (**Figure 4.3**).

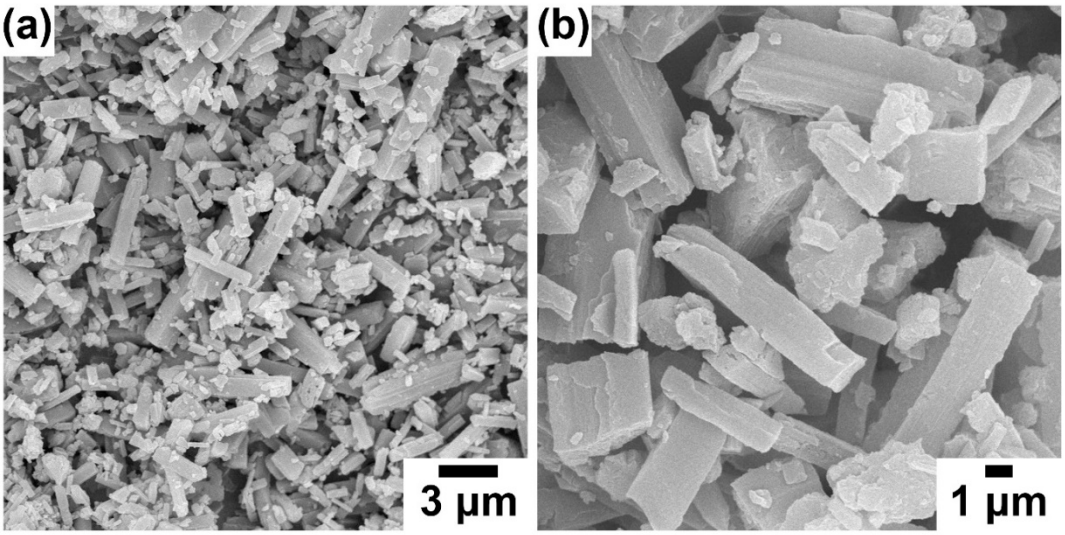

Figure 4.2 Scanning electron microscopy (SEM) images of Zn-Fe-DABCO-TPA MOFs.

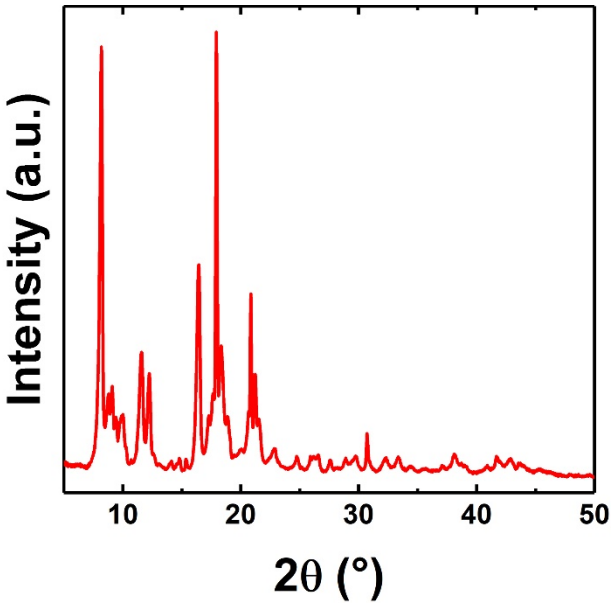

Figure 4.3 PXRD of the Zn-Fe-DABCO-TPA MOF showing high crystallinity.

4.4.2 Characterization of MOF-derived non-PGM electrocatalyst (Fe/C_T and Fe_T)

Figure 4.4a depicts the PXRD pattern for the Fe/C_{950} non-PGM electrocatalyst which exhibits two broad peaks centered at 22° and 43° corresponding to graphite carbon.[60, 188] The peaks appear to be quite broad characteristic of a carbon-based amorphous material. In contrast, while the Fe_{950} sample showed similar peaks attributed to graphite carbon, its profile also exhibited peaks attributed to iron oxide (Fe_2O_3). The Brunauer-Emmet-Teller (BET) surface area was also calculated based on the nitrogen adsorption isotherm shown in **Figure 4.4b**. The calculated surface area for Fe/C_{950} was 912 $m^2\ g^{-1}$ while that for Fe_{950} was calculated to be 714 $m^2\ g^{-1}$; the larger surface area observed in the Fe/C_{950} sample may be attributed to the use of Ketjen black carbon support.

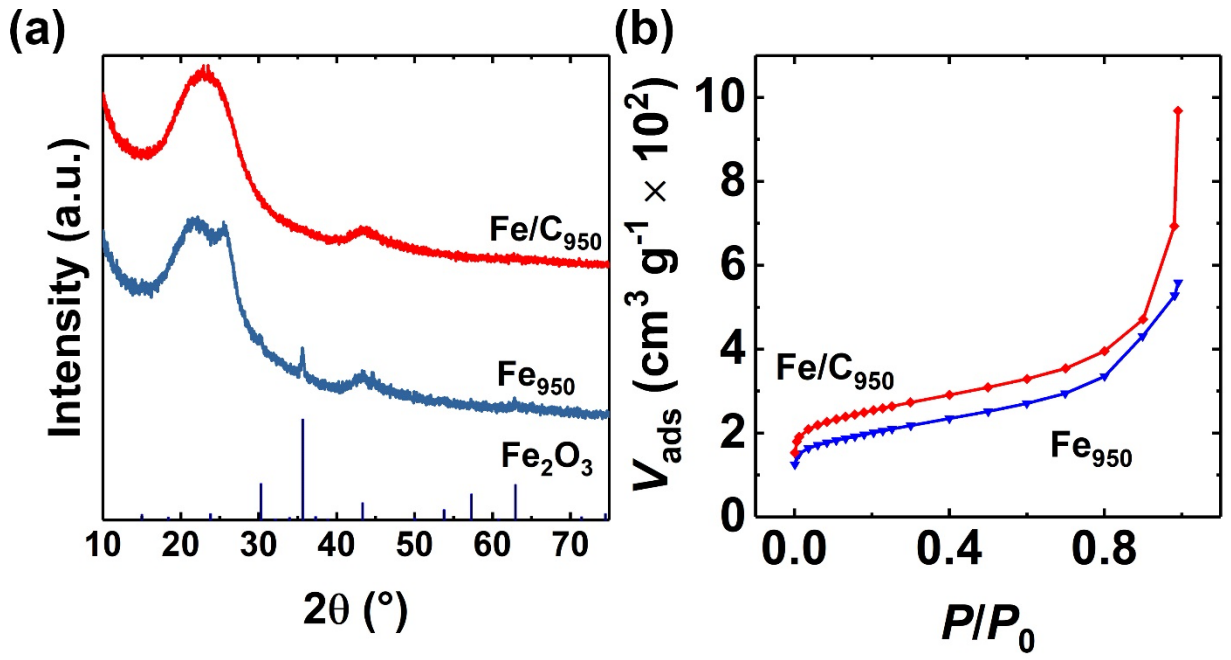

Figure 4.4 (a) PXRD of Fe/C_{950} and Fe_{950} (b) nitrogen adsorption isotherm for Fe/C_{950} and Fe_{950}.

Figure 4.5a shows the transmission electron microscopy (TEM) micrograph of the produced electrocatalysts which exhibit porous structures without any observable nanoparticles. Given the relatively large sizes of the MOF precursors based on the SEM images above, the high temperature synthesis did not lead to the formation of nanoparticles. This is likely due to the immobilization of the MOFs onto the Ketjen black carbon support which assists in the anchoring and distribution of the MOF precursors; this can decrease the likelihood of nanoparticle formation by reducing the effect of sintering. An aberration-corrected scanning transmission electron microscopy (STEM) study was carried out on the Fe/C_{950} to observe the structure of the single-atom moieties. The STEM image in **Figure 4.5b** shows bright spots, indicated by the yellow arrow; these bright spots correspond to single iron atoms in the carbon structure. In contrast, the TEM micrographs shown in **Figure 4.6** of the control Fe_{950} electrocatalyst, synthesized without the use of a Ketjen black carbon support, depicts an amorphous carbon structure consisting of several nanoparticle structures. This result suggests that in the absence of a carbon support, metal atoms are more likely to sinter together to form nanoparticles following the collapse of the MOF structure during pyrolysis; through the immobilization strategy, MOFs can be well dispersed across the support which can promote the isolation of single atoms and reduce agglomeration during the high temperature thermal treatment. The final iron loadings in both Fe/C_{950} and Fe_{950} based on inductively-coupled plasma mass spectrometry (ICP-MS) measurements are 0.72 wt.% and 2.16 wt.% respectively; the lower metal loading observed for Fe/C_{950} was likely a result of the carbon support.

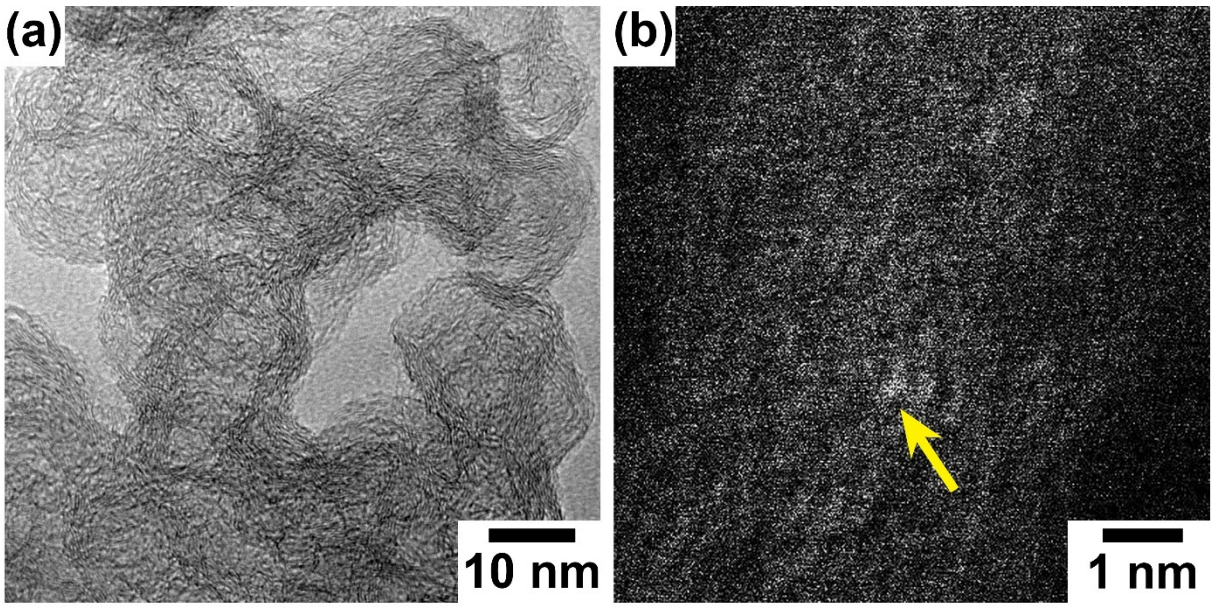

Figure 4.5 (a) Transmission electron micrograph of Fe/C_{950} showing a highly porous amorphous carbon structure (b) Aberration-corrected scanning transmission electron microscopy (STEM) of Fe/C_{950} showing an even dispersion of single-atom moieties in a carbon support.

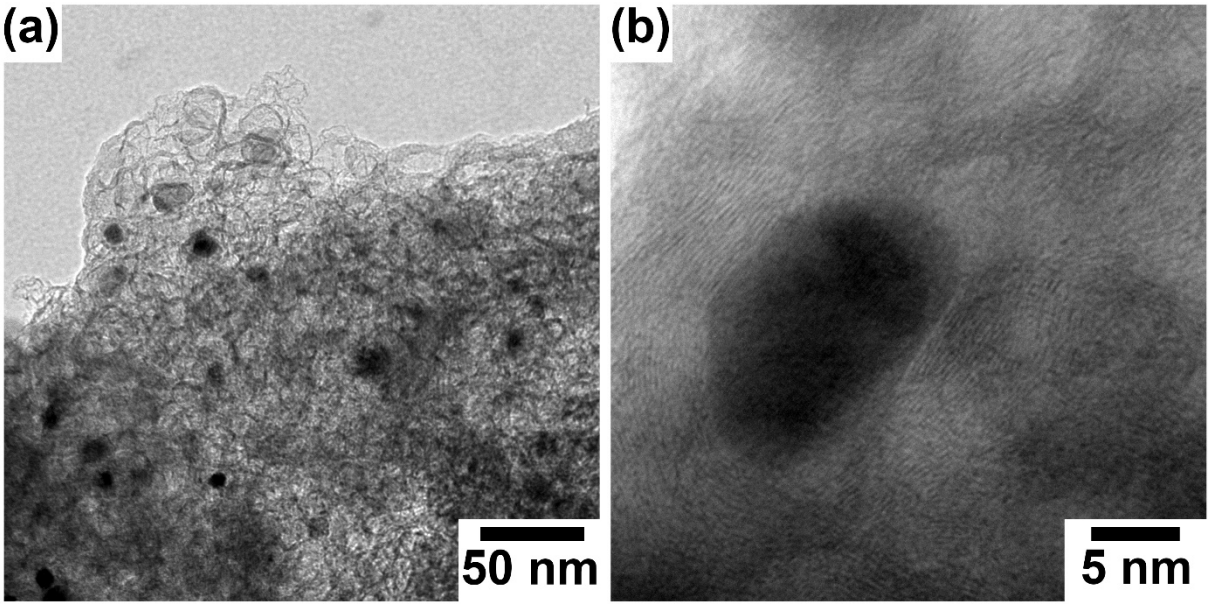

Figure 4.6 High-resolution transmission electron microscopy (HR-TEM) of (a, b) Fe_{950} showing the formation of metal nanoparticles.

To investigate the impact of temperature on the morphology and crystal structure of Fe/C_T, 850 °C and 1,050 °C were chosen as pyrolysis temperatures to treat the catalytic precursors. **Figure 4.7** shows the PXRD profiles for both Fe/C_{850} and Fe/C_{1050}; both materials did not exhibit the characteristic peaks of reduced iron or iron oxide structures. This suggested that alternative pyrolysis temperatures of 850 °C and 1,050 °C, the use of Ketjen black as the carbon support hindered nanoparticle formation. The TEM results in **Figure 4.8** further confirm the absence of these nanoparticles in both Fe/C_{850} and Fe/C_{950}. This further confirmed that at differing temperatures, the utilization of the Ketjen black carbon support can facilitate MOF dispersion which can mitigate nanoparticle formation.[189]

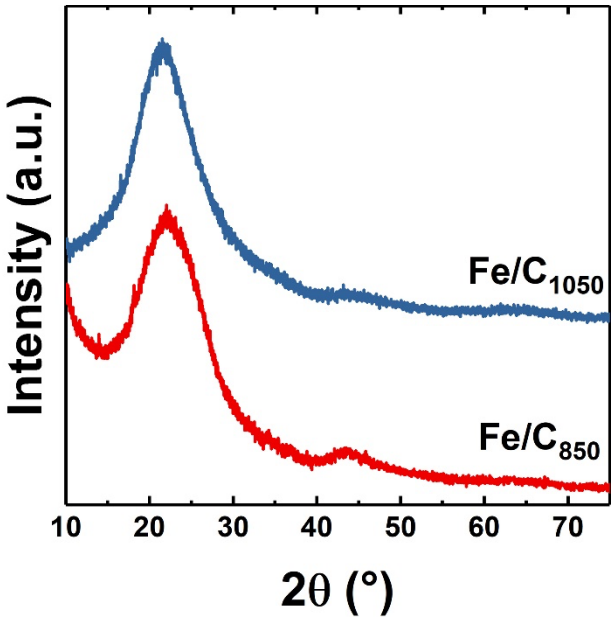

Figure 4.7 PXRD patterns of Zn-Fe-D-T derived electrocatalysts Fe/C_T under different pyrolysis conditions.

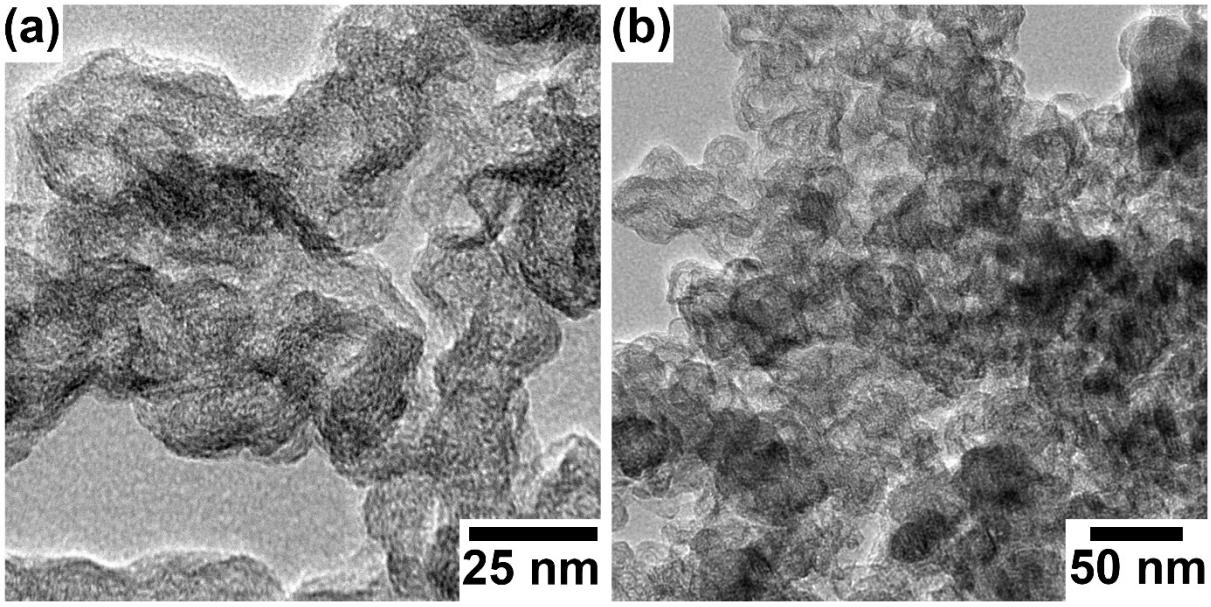

Figure 4.8 TEM micrographs of Zn-Fe MOF-derived Fe/C_T catalysts at different pyrolysis temperatures：(a) 850 ℃; (b) 1050 ℃.

X-ray adsorption near-edge spectroscopy (XANES) was used to investigate the chemical environment of the Fe atoms in both Fe/C_{950} and Fe_{950} and how they compared to standard reduced iron. This is done by evaluating absorption edge of each of these samples and correlating to the oxidation states of each catalyst at a synchrotron. The Fe/C_{950} and Fe_{950} electrocatalysts were investigated to elucidate the impact of the carbon support on the resultant valence state of the iron structures in both materials. **Figure 4.9** show the XANES of the iron K-edge region for both the Fe/C_{950} and Fe_{950} electrocatalysts and the corresponding reference iron foil. The delayed ascent in the edge energy of both electrocatalyst materials suggests that the overall valence state of the iron structures in both electrocatalysts is greater than that of the iron foil. X-ray photoelectron spectroscopy (XPS) of the nitrogen 1s region was used to examine the chemical environment of the various nitrogen structures based on their respective binding energies. **Figure 4.10** depicts the spectra for the nitrogen 1s region which shows both the Fe/C_{950} and Fe_{950} samples exhibit nitrogen

peaks pertaining to the pyridinic and pyrrolic species. Such nitrogen structures were attributed to the binding of Fe atoms for the high activity observed in non-PGM electrocatalysts.[93] The presence of metal-N peaks in both Fe/C_{950} and Fe_{950} electrocatalysts suggests that both materials exhibit iron structures which are strongly coordinated by nitrogen atoms.[46, 144] The binding energies of the various nitrogen moieties based are summarized in **Table 4.1**.

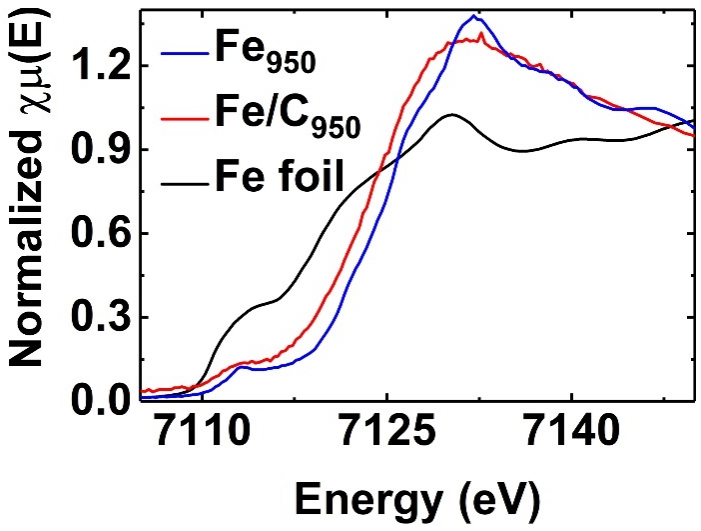

Figure 4.9 XANES of Fe K-edge for Fe/C_{950} and Fe_{950}.

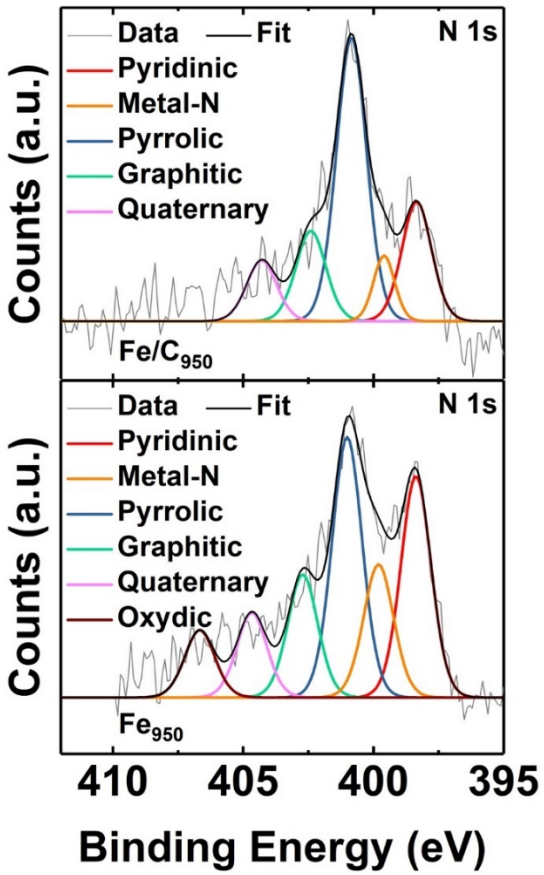

Figure 4.10 XPS spectra of the nitrogen 1s region of Fe_{950} and Fe/C_{950}.

Table 4.1 XPS analyses of the nitrogen species in the Fe/C_{950} and Fe_{950} electrocatalysts.

Sample	Binding Energy (eV)					
	Pyridinic	Fe-N	Pyrrolic	Graphitic	Quaternary	Oxydic
Fe/C_{950}	398.3	399.6	400.8	402.4	404.3	-
Fe_{950}	398.4	399.8	401.0	402.7	404.7	406.7

Graphitic carbon has also been shown to contribute to the ORR activity in non-PGM electrocatalysts.[23, 59] Raman spectroscopy was used to investigate the graphitic structure in both the Fe/C_{950} and Fe_{950} electrocatalysts. The Raman spectroscopy for graphite contains two major peaks. The first known as the G band located ~1582 cm^{-1} and arises from the radial breathing mode (RBM) observed in sp^2 carbon materials. The second is the disorder-induced D band located at ~1345 cm^{-1}.[65, 190-192] Calculating the ratios of the area between these two bands gives a benchmark of the relative graphitic nature of the carbon material. **Figure 4.11** shows the Raman spectra of both Fe/C_{950} (a) and Fe_{950} (b). The Fe/C_{950} sample exhibited a D/G ratio of 2.81, while that for the Fe_{950} electrocatalyst was calculated to be 1.81. The results suggest that a larger D/G ratio is indicative of greater disorder. The fitting value of the D and G bands of the graphitic carbon region are summarized in **Table 4.2**.

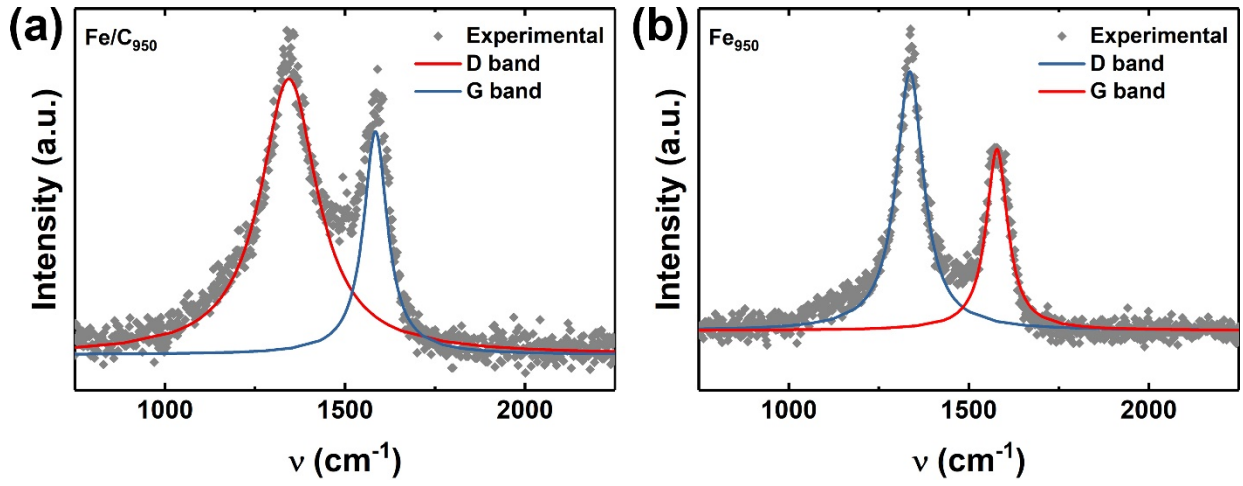

Figure 4.11 Raman spectra for (a) Fe/C_{950} and (b) Fe_{950} depicting the D band and G bands.

Table 4.2 Raman fitting results of D and G bands in the Fe/C_{950} and Fe_{950} electrocatalysts.

Band	Fe/C_{950}		Fe_{950}	
	ν (cm^{-1})	**FWHM (cm^{-1})**	**ν (cm^{-1})**	**FWHM (cm^{-1})**
D	1344.1	192.3	1336.3	92.4
G	1584.5	80.3	1578.1	72.3

4.4.3 ORR activity analysis of MOF-derived non-PGM electrocatalyst (Fe/C_T and Fe_T)

Linear-sweep voltammetry (LSV) was utilized to assess the activity of the as-made electrocatalysts. **Figure 4.12** shows the LSV data for the Fe/C_T and Fe_{950} electrocatalysts. As shown in Figure **4.12a**, among the three Fe/C_T electrocatalysts, Fe/C_{950} exhibited the greatest positive onset potential (E_{onset}) of 0.96 V and a half-wave potential ($E_{1/2}$) of 0.84 V versus the reversible hydrogen electrode (RHE). Both values were higher than those for the reference Pt/C under the same RDE testing conditions. **Figure 4.12b** shows the polarization curves for all three non-PGM Fe/C_T electrocatalysts and the control of Fe_{950} catalyst. There is not a clear trend between the benchmark values of the E_{onset} and the $E_{1/2}$; however, there exists an optimal pyrolysis temperature of 950 °C (Figure 2d). When the pyrolysis temperature was above or below this temperature, the ORR activity of the produced Fe/C catalysts was low in comparison. In the case of Fe_{950}, wherein there was an omission of the Ketjen black carbon support as a MOF-dispersing agent, the resulting non-PGM electrocatalyst exhibited reduced activity. Koutecky-Levich analysis was used to analyze the charge transfer of the reaction. **Figure 4.13a** shows the linear sweep

voltammograms for the Fe/C_{950} electrocatalyst at different rotation rates between 400 rpm and 2500 rpm. Based on the analysis the Fe/C_{950} electrocatalyst underwent a four-electron transfer pathway during the ORR (**Figure 4.13b**).

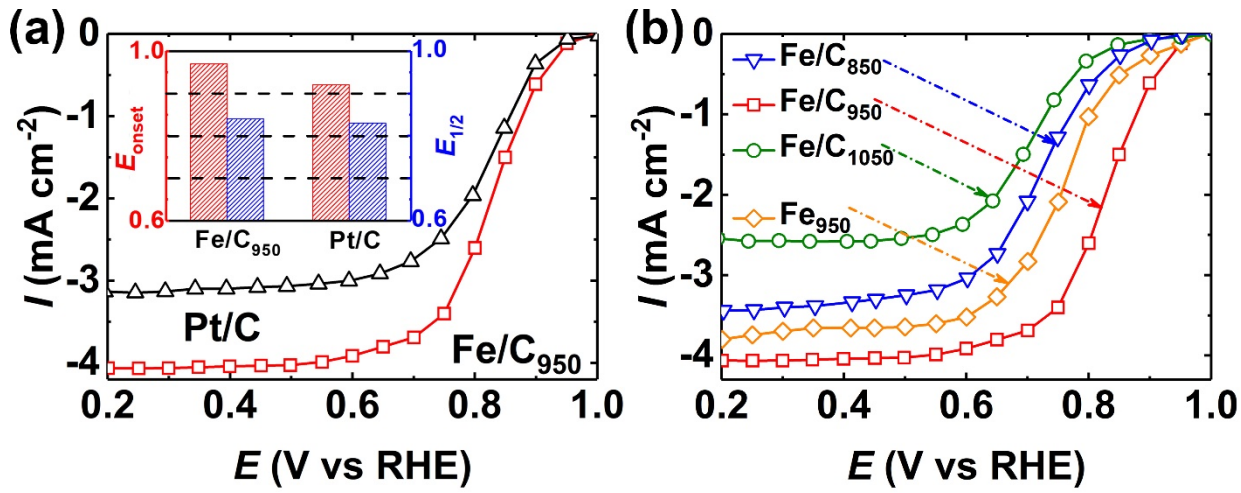

Figure 4.12 (a) Linear sweep voltammograms of Fe/C_{950} and reference Pt/C catalysts and (b) of Fe/C_T and Fe_{950}. Test conditions: O_2-saturated 0.1 M $HClO_4$, disk rotation rate 900 rpm, catalyst loading 1 mg cm^{-2}.

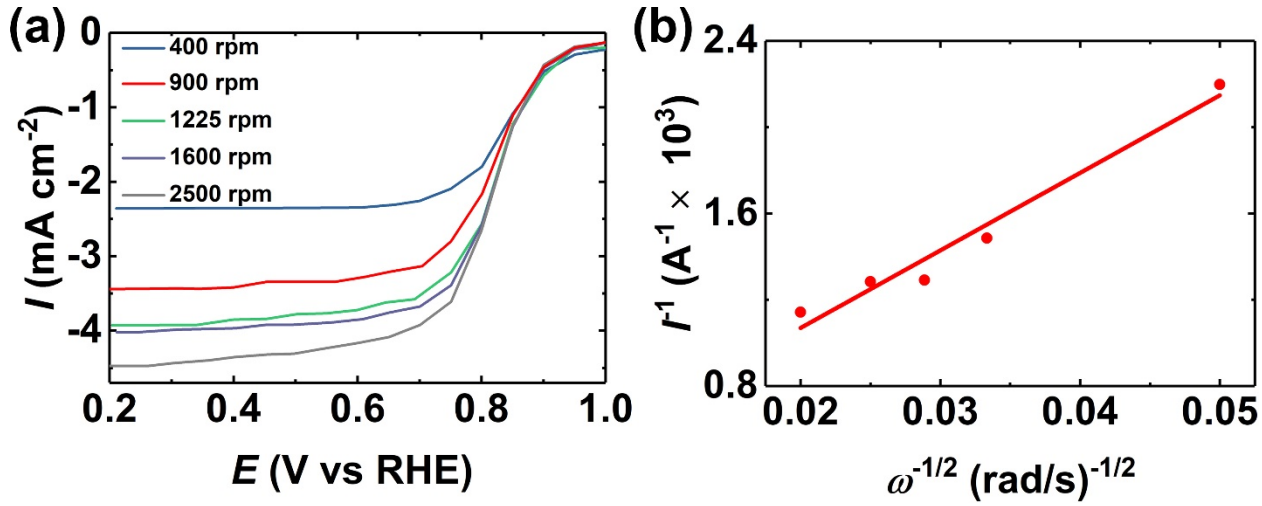

Figure 4.13 (a) Voltammograms and (b) Koutecky-Levich analysis of Fe/C_{950}.

4.5 Summary and future considerations

As is well established, the general synthesis of non-PGM electrocatalysts involves high temperature pyrolysis which has been shown to enhance the performance of these electrocatalysts for several reasons. While high temperature pyrolysis is necessary for the removal of the SM and the formation of an active catalyst surface, it can lead to the unwanted formation of inactive nanoparticle structures through sintering. In our study we were able to demonstrate, through our dual-strategic approach of using a MOF in conjunction with immobilization onto a support, the synthesis of metal single atom structures active for the ORR. By utilizing a dual-ligated MOF in conjunction with an immobilization strategy, atomically dispersed single Fe-atom ORR electrocatalysts were produced at an optimal pyrolysis temperature around 950 °C. The approach developed in this study is capable of producing high-level single Fe atoms in amorphous environments and promotes the formation of a high density of single atoms as FeN_x active sites.

This provides a useful design platform for making high-performance non-PGM electrocatalysts. In conclusion, the use of dual-ligated MOF ADPs and the introduction of additional Ketjen carbon black as the support/dispersion solid led to the controlled synthesis favoring the production of a single atom Fe-containing non-PGM catalysts with activity exceeding certain reference Pt/C catalysts.

CHAPTER 5

CONCLUDING REMARKS, FUTURE DIRECTIONS, AND RECOMMENDATIONS

In this thesis, we used ZIF-8 as a model precursor to understand the role of pyrolysis temperature in determining the structure of active components in MOF-derived non-PGM electrocatalysts. Our experimental results, characterization techniques, and computational methods allowed for the identification of iron nanoparticles alongside single atom iron structures which serve to boost the activity of non-PGM MOF-derived electrocatalysts. Based on our computational study, it was revealed that the presence of a carbon-encapsulated iron particle can initiate OOH bond cleavage through the activation of surface carbon atoms; this activation leads to a decrease in the energy of adsorption of OH* onto the surface carbon atom. This allowed us to identify the need to carve out strategies to produce greater homogeneity in MOF-derived electrocatalyst materials. The objective would be to synthesize electrocatalyst materials with specific structures to be investigated and assist in eliminating the ambiguity surrounding the active structures in non-PGM electrocatalysts for the ORR.

Through a tuning of the sacrificial metal, we synthesized a novel DABCO-TPA dual-ligated cadmium-based MOF precursor. We demonstrated that the temperature of synthesis of MOF-derived non-PGM electrocatalysts can be reduced thereby improving the structural homogeneity as shown through our various characterization methods. At higher temperatures reduced nanoparticle structures were formed with an observed increase in the activity towards the ORR. Lastly, we were able to demonstrate that the immobilization of our dual-ligated DABCO-TPA MOF onto a Ketjen black carbon support afforded an alternative pathway to achieving dispersed single atom sites at elevated pyrolysis temperatures. In our work we have proposed methods to

increase the dispersion of the active metal precursor prior to pyrolysis in an attempt to increase single-atom site density in the final catalyst.

Moving forward, there is a need to take into consideration additional aspects relating to the performance of non-PGM electrocatalysts, in particular catalyst stability. Furthermore, the use of in-situ and operando techniques provide an avenue for investigating changes in the catalyst behavior under reaction conditions. Lastly, the use of electrochemical methods such as three-electrode half-cell measurements are insufficient in benchmarking the performance of electrocatalysts; there is a need to integrate of these catalyst materials into membrane-electrode assembly (MEA) systems which is necessary to understand how these catalyst materials function under realistic operating conditions.

Cathode catalysts in PEMFCs must be able to operate in highly acidic environments and at various potentials without substantial degradation. In the case of non-PGM electrocatalysts, catalyst degradation can occur through a number of pathways.[193-196] The first applies primarily to iron-based systems, wherein hydrogen peroxide (H_2O_2), a product from the incomplete reduction of oxygen, can react with Fe^{2+} sites to generate hydroxyl radicals through a process known as the Fenton reaction which can oxidize and degrade the catalyst.[151] The second pathway results from the oxidation of the carbon support at high potentials into carbon dioxide which can lead to a destabilization of the metal sites. Operando techniques have shown that during operation there occurs an oxidation of carbon at high potentials; at lower potentials, catalyst demetallation is more apparent.[30, 197] Further experiments showed that demetallation primarily occurs in catalysts containing iron particles and, in their absence, demetallation was reduced.[198] Yet, a third can occur through "micropore flooding" which results when water (H_2O) generated at the catalyst surface is

not evacuated which can lead to its buildup and blockage of active structures to further carry out the reaction; this phenomena has also been suggested to lead to demetallation.[199]

To address these concerns, certain methods are introduced which can help suppress the above phenomena and maintain catalytic activity. Alternative metals such as cobalt[3, 62, 73, 168], manganese[27], and tin[28] can be used instead of iron to prevent the Fenton reaction. Graphitized carbon has been reported to exhibit greater stability under reaction conditions than amorphous carbon[200]; however, single atom sites are typically hosted within the amorphous carbon structure leading to a dilemma regarding the catalytic activity as it originates from the single atom structures versus the stability which can be enhanced through the presence of graphitic carbon.[201]

Future efforts should include a focus on developing non-PGM electrocatalysts with enhanced stability in PEMFCs. This can bridge the gap in taking these materials from a laboratory setting to commercial application.

REFERENCES

1. Debe, M. K., Electrocatalyst approaches and challenges for automotive fuel cells. *Nature* **2012,** *486*, 43-51.

2. Shi, H.; Shen, Y. F.; He, F.; Li, Y.; Liu, A. R.; Liu, S. Q.; Zhang, Y. J., Recent advances of doped carbon as non-precious catalysts for oxygen reduction reaction. *J. Mater. Chem. A* **2014,** *2*, 15704-15716.

3. Wang, X. X.; Prabhakaran, V.; He, Y.; Shao, Y.; Wu, G., Iron-free cathode catalysts for proton-exchange-membrane fuel cells: cobalt catalysts and the peroxide mitigation approach. *Adv. Mater.* **2019,** *31*, 1805126.

4. Strickland, K.; Miner, E.; Jia, Q.; Tylus, U.; Ramaswamy, N.; Liang, W.; Sougrati, M.-T.; Jaouen, F.; Mukerjee, S., Highly active oxygen reduction non-platinum group metal electrocatalyst without direct metal–nitrogen coordination. *Nat. Commun.* **2015,** *6*, 7343.

5. Li, J.; Ghoshal, S.; Liang, W.; Sougrati, M.-T.; Jaouen, F.; Halevi, B.; McKinney, S.; McCool, G.; Ma, C.; Yuan, X.; Ma, Z.-F.; Mukerjee, S.; Jia, Q., Structural and mechanistic basis for the high activity of Fe–N–C catalysts toward oxygen reduction. *Energy Environ. Sci.* **2016,** *9*, 2418-2432.

6. Nørskov, J. K.; Rossmeisl, J.; Logadottir, A.; Lindqvist, L.; Kitchin, J. R.; Bligaard, T.; Jónsson, H., Origin of the overpotential for oxygen reduction at a fuel-cell cathode. *J. Phys. Chem. B* **2004,** *108*, 17886-17892.

7. Ramaswamy, N.; Mukerjee, S., Fundamental mechanistic understanding of electrocatalysis of oxygen reduction on Pt and non-Pt surfaces: acid versus alkaline media. *Adv. Phys. Chem.* **2012,** *2012*, 491604.

8. Wroblowa, H. S.; Yen Chi, P.; Razumney, G., Electroreduction of oxygen: A new mechanistic criterion. *J. Electroanal. Chem.* **1976,** *69*, 195-201.

9. Anastasijević, N. A.; Vesović, V.; Adžić, R. R., Determination of the kinetic parameters of the oxygen reduction reaction using the rotating ring-disk electrode: Part II. Applications. *J. Electroanal. Chem. Interf. Electrochem.* **1987,** *229*, 317-325.

10. Ford, D. C.; Nilekar, A. U.; Xu, Y.; Mavrikakis, M., Partial and complete reduction of O_2 by hydrogen on transition metal surfaces. *Surf. Sci.* **2010,** *604*, 1565-1575.

11. Koper, M. T. M., Thermodynamic theory of multi-electron transfer reactions: implications for electrocatalysis. *J. Electroanal. Chem.* **2011,** *660*, 254-260.

12. Duan, Z.; Wang, G., A first principles study of oxygen reduction reaction on a Pt(111) surface modified by a subsurface transition metal M (M = Ni, Co, or Fe). *Phys. Chem. Chem. Phys.* **2011,** *13*, 20178-20187.

13. Holton, O. T.; Stevenson, J. W., The role of platinum in proton exchange membrane fuel cells. *Platin. Met. Rev* **2013,** *57*, 259-271.

14. Peng, Z.; Yang, H., Designer platinum nanoparticles: control of shape, composition in alloy, nanostructure and electrocatalytic property. *Nano Today* **2009,** *4*, 143-164.

15. Wu, J.; Yang, H., Platinum-based oxygen reduction electrocatalysts. *Acc. Chem. Res.* **2013,** *46*, 1848-1857.

16. Greeley, J.; Stephens, I. E. L.; Bondarenko, A. S.; Johansson, T. P.; Hansen, H. A.; Jaramillo, T. F.; Rossmeisl, J.; Chorkendorff, I.; Nørskov, J. K., Alloys of platinum and early transition metals as oxygen reduction electrocatalysts. *Nat. Chem.* **2009,** *1*, 552-556.

17. Stamenkovic, V.; Mun, B. S.; Mayrhofer, K. J. J.; Ross, P. N.; Markovic, N. M.; Rossmeisl, J.; Greeley, J.; Nørskov, J. K., Changing the activity of electrocatalysts for oxygen reduction by tuning the surface electronic structure. *Angew. Chem. Int. Ed.* **2006,** *45*, 2897-2901.

18. Mukerjee, S.; Srinivasan, S., Enhanced electrocatalysis of oxygen reduction on platinum alloys in proton exchange membrane fuel cells. *J. Electroanal. Chem.* **1993,** *357*, 201-224.

19. Chong, L.; Wen, J.; Kubal, J.; Sen, F. G.; Zou, J.; Greeley, J.; Chan, M.; Barkholtz, H.; Ding, W.; Liu, D.-J., Ultralow-loading platinum-cobalt fuel cell catalysts derived from imidazolate frameworks. *Science* **2018,** *362*, 1276-1281.

20. Stamenkovic, V. R.; Fowler, B.; Mun, B. S.; Wang, G.; Ross, P. N.; Lucas, C. A.; Marković, N. M., Improved oxygen reduction activity on $Pt_3Ni(111)$ via increased surface site availability. *Science* **2007,** *315*, 493-497.

21. Wu, G.; More, K. L.; Johnston, C. M.; Zelenay, P., High-performance electrocatalysts for oxygen reduction derived from polyaniline, iron, and cobalt. *Science* **2011,** *332*, 443-447.

22. Proietti, E.; Jaouen, F.; Lefèvre, M.; Larouche, N.; Tian, J.; Herranz, J.; Dodelet, J.-P., Iron-based cathode catalyst with enhanced power density in polymer electrolyte membrane fuel cells. *Nat. Commun.* **2011,** *2*, 416.

23. Zitolo, A.; Goellner, V.; Armel, V.; Sougrati, M. T.; Mineva, T.; Stievano, L.; Fonda, E.; Jaouen, F., Identification of catalytic sites for oxygen reduction in iron- and nitrogen-doped graphene materials. *Nat. Mater.* **2015,** *14*, 937-942.

24. Chen, Z. W.; Higgins, D.; Yu, A. P.; Zhang, L.; Zhang, J. J., A review on non-precious metal electrocatalysts for PEM fuel cells. *Energy Environ. Sci.* **2011,** *4*, 3167-3192.

25. Gewirth, A. A.; Varnell, J. A.; DiAscro, A. M., Nonprecious metal catalysts for oxygen reduction in heterogeneous aqueous systems. *Chem. Rev.* **2018,** *118*, 2313-2339.

26. Barkholtz, H. M.; Liu, D.-J., Advancements in rationally designed PGM-free fuel cell catalysts derived from metal–organic frameworks. *Mater. Horiz.* **2017,** *4*, 20-37.

27. Li, J.; Chen, M.; Cullen, D. A.; Hwang, S.; Wang, M.; Li, B.; Liu, K.; Karakalos, S.; Lucero, M.; Zhang, H.; Lei, C.; Xu, H.; Sterbinsky, G. E.; Feng, Z.; Su, D.; More, K. L.; Wang, G.; Wang, Z.; Wu, G., Atomically dispersed manganese catalysts for oxygen reduction in proton-exchange membrane fuel cells. *Nat. Catal.* **2018,** *1*, 935-945.

28. Luo, F.; Roy, A.; Silvioli, L.; Cullen, D. A.; Zitolo, A.; Sougrati, M. T.; Oguz, I. C.; Mineva, T.; Teschner, D.; Wagner, S.; Wen, J.; Dionigi, F.; Kramm, U. I.; Rossmeisl, J.; Jaouen, F.; Strasser, P., P-block single-metal-site tin/nitrogen-doped carbon fuel cell cathode catalyst for oxygen reduction reaction. *Nat. Mat.* **2020,** *19*, 1215–1223.

29. Choi, C. H.; Lim, H.-K.; Chung, M. W.; Chon, G.; Ranjbar Sahraie, N.; Altin, A.; Sougrati, M.-T.; Stievano, L.; Oh, H. S.; Park, E. S.; Luo, F.; Strasser, P.; Dražić, G.; Mayrhofer, K. J. J.; Kim, H.; Jaouen, F., The Achilles' heel of iron-based catalysts during oxygen reduction in an acidic medium. *Energy Environ. Sci.* **2018,** *11*, 3176-3182.

30. Choi, C. H.; Baldizzone, C.; Grote, J.-P.; Schuppert, A. K.; Jaouen, F.; Mayrhofer, K. J. J., Stability of Fe-N-C catalysts in acidic medium studied by operando spectroscopy. *Angew. Chem. Int. Ed.* **2015,** *54*, 12753-12757.

31. Shao, M.; Chang, Q.; Dodelet, J.-P.; Chenitz, R., Recent advances in electrocatalysts for oxygen reduction reaction. *Chem. Rev.* **2016,** *116*, 3594-3657.

32. Yang, H.; Oluf, J. J.; Wei, Z.; N., C. L.; Wei, X.; J., B. N.; Qingfeng, L., Hollow spheres of iron carbide nanoparticles encased in graphitic layers as oxygen reduction catalysts. *Angew. Chem. Int. Edit.* **2014,** *53*, 3675-3679.

33. Wu, Z. Y.; Xu, X. X.; Hu, B. C.; Liang, H. W.; Lin, Y.; Chen, L. F.; Yu, S. H., Iron carbide nanoparticles encapsulated in mesoporous Fe-N-doped carbon nanofibers for efficient electrocatalysis. *Angew. Chem. Int. Edit.* **2015,** *54*, 8179-8183.

34. Varnell, J. A.; Tse, E. C.; Schulz, C. E.; Fister, T. T.; Haasch, R. T.; Timoshenko, J.; Frenkel, A. I.; Gewirth, A. A., Identification of carbon-encapsulated iron nanoparticles as active species in non-precious metal oxygen reduction catalysts. *Nat. Commun.* **2016,** *7*, 12582.

35. Jiang, W.-J.; Gu, L.; Li, L.; Zhang, Y.; Zhang, X.; Zhang, L.-J.; Wang, J.-Q.; Hu, J.-S.; Wei, Z.; Wan, L.-J., Understanding the high activity of Fe–N–C electrocatalysts in oxygen reduction: Fe/Fe_3C nanoparticles boost the activity of $Fe–N_x$. *J. Am. Chem. Soc.* **2016,** *138*, 3570-3578.

36. Sun, T.; Jiang, Y.; Wu, Q.; Du, L.; Zhang, Z.; Yang, L.; Wang, X.; Hu, Z., Is iron nitride or carbide highly active for oxygen reduction reaction in acidic medium? *Catal. Sci. Technol.* **2017,** *7*, 51-55.

37. Dai, L. M.; Xue, Y. H.; Qu, L. T.; Choi, H. J.; Baek, J. B., Metal-free catalysts for oxygen reduction reaction. *Chem. Rev.* **2015,** *115*, 4823-4892.

38. Wiesener, K., N_4-chelates as electrocatalyst for cathodic oxygen reduction. *Electrochim. Acta* **1986,** *31*, 1073-1078.

39. Franke, R.; Ohms, D.; Wiesener, K., Investigation of the influence of thermal treatment on the properties of carbon materials modified by N_4-chelates for the reduction of oxygen in acidic media. *J. Electroanal. Chem. Interf. Electrochem.* **1989,** *260*, 63-73.

40. Varnell, J. A.; Sotiropoulos, J. S.; Brown, T. M.; Subedi, K.; Haasch, R. T.; Schulz, C. E.; Gewirth, A. A., Revealing the role of the metal in non-precious-metal catalysts for oxygen reduction via selective removal of Fe. *ACS Energy Lett.* **2018,** *3*, 823-828.

41. Singh, D.; Tian, J.; Mamtani, K.; King, J.; Miller, J. T.; Ozkan, U. S., A comparison of N-containing carbon nanostructures (CN_x) and N-coordinated iron–carbon catalysts (FeNC) for the oxygen reduction reaction in acidic media. *J. Catal.* **2014,** *317*, 30-43.

42. Jaouen, F.; Proietti, E.; Lefèvre, M.; Chenitz, R.; Dodelet, J.-P.; Wu, G.; Chung, H. T.; Johnston, C. M.; Zelenay, P., Recent advances in non-precious metal catalysis for oxygen-reduction reaction in polymer electrolyte fuel cells. *Energy Environ. Sci.* **2011,** *4*, 114-130.

43. Jaouen, F.; Lefèvre, M.; Dodelet, J.-P.; Cai, M., Heat-treated Fe/N/C catalysts for O_2 electroreduction: are active sites hosted in micropores? *J. Phys. Chem. B* **2006,** *110*, 5553-5558.

44. Kramm, U. I.; Zana, A.; Vosch, T.; Fiechter, S.; Arenz, M.; Schmeißer, D., On the structural composition and stability of Fe–N–C catalysts prepared by an intermediate acid leaching. *J. Solid State Electrochem.* **2016,** *20*, 969-981.

45. Pels, J. R.; Kapteijn, F.; Moulijn, J. A.; Zhu, Q.; Thomas, K. M., Evolution of nitrogen functionalities in carbonaceous materials during pyrolysis. *Carbon* **1995,** *33*, 1641-1653.

46. Kramm, U. I.; Abs-Wurmbach, I.; Fiechter, S.; Herrmann, I.; Radnik, J.; Bogdanoff, P., New insight into the nature of catalytic activity of pyrolysed iron porphyrin based electro-catalysts for the oxygen reduction reaction (ORR) in acidic media. *ECS Trans.* **2009,** *25*, 93-104.

47. Wang, H.; Wang, L.; Wang, Q.; Ye, S.; Sun, W.; Shao, Y.; Jiang, Z.; Qiao, Q.; Zhu, Y.; Song, P.; Li, D.; He, L.; Zhang, X.; Yuan, J.; Wu, T.; Ozin, G. A., Ambient electrosynthesis of ammonia: electrode porosity and composition engineering. *Angew. Chem. Int. Edit.* **2018,** *57*, 12360-12364.

48. Wu, G.; Nelson, M. A.; Mack, N. H.; Ma, S.; Sekhar, P.; Garzon, F. H.; Zelenay, P., Titanium dioxide-supported non-precious metal oxygen reduction electrocatalyst. *Chem. Commun.* **2010,** *46*, 7489-7491.

49. Wu, G.; Dai, C.; Wang, D.; Li, D.; Li, N., Nitrogen-doped magnetic onion-like carbon as support for Pt particles in a hybrid cathode catalyst for fuel cells. *J. Mater. Chem.* **2010,** *20*, 3059-3068.

50. Craig, P. P.; Dash, J. G.; McGuire, A. D.; Nagle, D.; Reiswig, R. R., Nuclear resonance absorption of gamma rays in Ir^{191}. *Phys. Rev. Lett.* **1959,** *3*, 221-223.

51. Kramm, U. I., Non precious catalysts for fuel cells - a short review on Mossbauer spectroscopy of Fe-N-C catalysts for ORR. *ECS Trans.* **2013,** *58*, 119-127.

52. Kramm, U. I.; Lefevre, M.; Larouche, N.; Schmeisser, D.; Dodelet, J.-P., Correlations between mass activity and physicochemical properties of Fe/N/C catalysts for the ORR in PEM fuel cell via ^{57}Fe Mossbauer spectroscopy and other techniques. *J. Am. Chem. Soc.* **2014,** *136*, 978-985.

53. Kramm, U. I.; Herranz, J.; Larouche, N.; Arruda, T. M.; Lefevre, M.; Jaouen, F.; Bogdanoff, P.; Fiechter, S.; Abs-Wurmbach, I.; Mukerjee, S.; Dodelet, J.-P., Structure of the catalytic sites in Fe/N/C-catalysts for O_2-reduction in PEM fuel cells. *Phys. Chem. Chem. Phys.* **2012,** *14*, 11673-11688.

54. Kramm, U. I.; Herrmann-Geppert, I.; Bogdanoff, P.; Fiechter, S., Effect of an ammonia treatment on structure, composition, and oxygen reduction reaction activity of Fe-N-C catalysts. *J. Phys. Chem. C* **2011,** *115*, 23417-23427.

55. Koslowski, U. I.; Abs-Wurmbach, I.; Fiechter, S.; Bogdanoff, P., Nature of the catalytic centers of porphyrin-based electrocatalysts for the ORR: a correlation of kinetic current density with the site density of Fe-N_4 centers. *J. Phys. Chem. C* **2008,** *112*, 15356-15366.

56. Kramm, U. I.; Herrmann-Geppert, I.; Behrends, J.; Lips, K.; Fiechter, S.; Bogdanoff, P., On an easy way to prepare metal–nitrogen doped carbon with exclusive presence of MeN_4-type sites active for the ORR. *J. Am. Chem. Soc.* **2016,** *138*, 635-640.

57. Kneebone, J. L.; Daifuku, S. L.; Kehl, J. A.; Wu, G.; Chung, H. T.; Hu, M. Y.; Alp, E. E.; More, K. L.; Zelenay, P.; Holby, E. F.; Neidig, M. L., A combined probe-molecule, Mössbauer, nuclear resonance vibrational spectroscopy, and density functional theory approach for evaluation of potential iron active sites in an oxygen reduction reaction catalyst. *J. Phys. Chem. C* **2017,** *121*, 16283-16290.

58. Chung, H. T.; Cullen, D. A.; Higgins, D.; Sneed, B. T.; Holby, E. F.; More, K. L.; Zelenay, P., Direct atomic-level insight into the active sites of a high-performance PGM-free ORR catalyst. *Science* **2017,** *357*, 479-483.

59. Zhang, H.; Hwang, S.; Wang, M.; Feng, Z.; Karakalos, S.; Luo, L.; Qiao, Z.; Xie, X.; Wang, C.; Su, D.; Shao, Y.; Wu, G., Single atomic iron catalysts for oxygen reduction in acidic media: particle size control and thermal activation. *J. Am. Chem. Soc.* **2017,** *139*, 14143-14149.

60. Liu, Q.; Liu, X.; Zheng, L.; Shui, J., The solid-phase synthesis of an Fe-N-C electrocatalyst for high-power proton-exchange membrane fuel cells. *Angew. Chem. Int. Edit.* **2017,** *57*, 1204-1208.

61. Li, J.; Zhang, H.; Samarakoon, W.; Shan, W.; Cullen, D. A.; Karakalos, S.; Chen, M.; Gu, D.; More, K. L.; Wang, G.; Feng, Z.; Wang, Z.; Wu, G., Thermally driven structure and performance evolution of atomically dispersed FeN_4 sites for oxygen reduction. *Angew. Chem. Int. Ed.* **2019,** *58*, 18971-18980.

62. He, Y.; Hwang, S.; Cullen, D. A.; Uddin, M. A.; Langhorst, L.; Li, B.; Karakalos, S.; Kropf, A. J.; Wegener, E. C.; Sokolowski, J.; Chen, M.; Myers, D.; Su, D.; More, K. L.; Wang, G.; Litster, S.; Wu, G., Highly active atomically dispersed CoN_4 fuel cell cathode catalysts derived from surfactant-assisted MOFs: carbon-shell confinement strategy. *Energ. Environ. Sci.* **2019,** *12*, 250-260.

63. Barr, T. L.; Seal, S., Nature of the use of adventitious carbon as a binding energy standard. *J. Vac. Sci. Technol. A* **1995,** *13*, 1239-1246.

64. Swift, P., Adventitious carbon—the panacea for energy referencing? *Surf. Interface Anal.* **1982,** *4*, 47-51.

65. Dresselhaus, M. S.; Jorio, A.; Hofmann, M.; Dresselhaus, G.; Saito, R., Perspectives on carbon nanotubes and graphene Raman spectroscopy. *Nano Lett.* **2010,** *10*, 751-758.

66. Malard, L. M.; Pimenta, M. A.; Dresselhaus, G.; Dresselhaus, M. S., Raman spectroscopy in graphene. *Phys. Rep.* **2009,** *473*, 51-87.

67. Martensson, N.; Söderström, J.; Svensson, S.; Travnikova, O.; Patanen, M.; Miron, C.; Saethre, L.; Børve, K.; Thomas, T.; Kas, J.; others, On the relation between X-ray photoelectron spectroscopy and XAFS. *J. Phys. Conf. Ser.* **2013,** *430*, 012131.

68. Mamtani, K.; Singh, D.; Tian, J.; Millet, J.-M. M.; Miller, J. T.; Co, A. C.; Ozkan, U. S., Evolution of N-coordinated iron–carbon (FeNC) catalysts and their oxygen reduction (ORR) performance in acidic media at various stages of catalyst synthesis: an attempt at benchmarking. *Catal. Letters* **2016,** *146*, 1749-1770.

69. Zhu, Y.; Zhang, B.; Feng, Z.; Su, D. S., Synthesis–structure–performance correlation for poly(phenylenediamine)s/iron/carbon non-precious metal catalysts for oxygen reduction reaction. *Catal. Today* **2016,** *260*, 112-118.

70. Wang, X.; Zhang, H.; Lin, H.; Gupta, S.; Wang, C.; Tao, Z.; Fu, H.; Wang, T.; Zheng, J.; Wu, G.; Li, X., Directly converting Fe-doped metal–organic frameworks into highly active and stable Fe-N-C catalysts for oxygen reduction in acid. *Nano Energy* **2016,** *25*, 110-119.

71. Zhang, C.; Wang, Y.-C.; An, B.; Huang, R.; Wang, C.; Zhou, Z.; Lin, W., Networking pyrolyzed zeolitic imidazolate frameworks by carbon nanotubes improves conductivity and enhances oxygen-reduction performance in polymer-electrolyte-membrane fuel cells. *Adv. Mater.* **2017,** *29*, 1604556.

72. Zitolo, A.; Ranjbar-Sahraie, N.; Mineva, T.; Li, J.; Jia, Q.; Stamatin, S.; Harrington, G. F.; Lyth, S. M.; Krtil, P.; Mukerjee, S.; Fonda, E.; Jaouen, F., Identification of catalytic sites in cobalt-nitrogen-carbon materials for the oxygen reduction reaction. *Nat. Commun.* **2017,** *8*, 957.

73. Xie, X.; He, C.; Li, B.; He, Y.; Cullen, D. A.; Wegener, E. C.; Kropf, A. J.; Martinez, U.; Cheng, Y.; Engelhard, M. H.; Bowden, M. E.; Song, M.; Lemmon, T.; Li, X. S.; Nie, Z.; Liu, J.; Myers, D. J.; Zelenay, P.; Wang, G.; Wu, G.; Ramani, V.; Shao, Y., Performance enhancement and degradation mechanism identification of a single-atom Co–N–C catalyst for proton exchange membrane fuel cells. *Nat. Catal.* **2020**.

74. Zhu, J.; Xiao, M.; Liu, C.; Ge, J.; St-Pierre, J.; Xing, W., Growth mechanism and active site probing of Fe_3C@N-doped carbon nanotubes/C catalysts: guidance for building highly efficient oxygen reduction electrocatalysts. *J. Mater. Chem. A* **2015,** *3*, 21451-21459.

75. An, G.-H.; Lee, E.-H.; Ahn, H.-J., Well-dispersed iron nanoparticles exposed within nitrogen-doped mesoporous carbon nanofibers by hydrogen-activation for oxygen-reduction reaction. *J. Alloys Compd.* **2016,** *682*, 746-752.

76. Chatterjee, S.; Sengupta, K.; Samanta, S.; Das, P. K.; Dey, A., Electrocatalytic O_2 reduction reaction by synthetic analogues of cytochrome P450 and myoglobin: in-situ resonance Raman and dynamic electrochemistry investigations. *Inorg. Chem.* **2013,** *52*, 9897-9907.

77. Zhang, Q.; Mamtani, K.; Jain, D.; Ozkan, U.; Asthagiri, A., CO poisoning effects on FeNC and CN_x ORR catalysts: a combined experimental–computational study. *J. Phys. Chem. C* **2016,** *120*, 15173-15184.

78. Chung, M. W.; Chon, G.; Kim, H.; Jaouen, F.; Choi, C. H., Electrochemical evidence for two sub-families of FeN_xC_y moieties with concentration-dependent cyanide poisoning. *ChemElectroChem* **2018,** *5*, 1880-1885.

79. von Deak, D.; Singh, D.; King, J. C.; Ozkan, U. S., Use of carbon monoxide and cyanide to probe the active sites on nitrogen-doped carbon catalysts for oxygen reduction. *Appl. Catal. B* **2012,** *113-114*, 126-133.

80. Singh, D.; Mamtani, K.; Bruening, C. R.; Miller, J. T.; Ozkan, U. S., Use of H_2S to probe the active sites in FeNC catalysts for the oxygen reduction reaction (ORR) in acidic media. *ACS Catal.* **2014,** *4*, 3454-3462.

81. Zhang, G.; Yang, X.; Dubois, M.; Herraiz, M.; Chenitz, R.; Lefèvre, M.; Cherif, M.; Vidal, F.; Glibin, V. P.; Sun, S.; Dodelet, J.-P., Non-PGM electrocatalysts for PEM fuel cells: effect of fluorination on the activity and stability of a highly active NC_Ar + NH_3 catalyst. *Energy Environ. Sci.* **2019,** *12*, 3015-3037.

82. Wang, W.; Jia, Q.; Mukerjee, S.; Chen, S., Recent insights into the oxygen-reduction electrocatalysis of Fe/N/C materials. *ACS Catal.* **2019,** *9*, 10126-10141.

83. Wang, X.; Fan, X.; Lin, H.; Fu, H.; Wang, T.; Zheng, J.; Li, X., An efficient Co–N–C oxygen reduction catalyst with highly dispersed Co sites derived from a ZnCo bimetallic zeolitic imidazolate framework. *RSC Adv.* **2016,** *6*, 37965-37973.

84. Yin, P.; Yao, T.; Wu, Y.; Zheng, L.; Lin, Y.; Liu, W.; Ju, H.; Zhu, J.; Hong, X.; Deng, Z.; Zhou, G.; Wei, S.; Li, Y., Single cobalt atoms with precise N-coordination as superior oxygen reduction reaction catalysts. *Angew. Chem. Int. Edit.* **2016,** *55*, 10800-10805.

85. Tang, H.; Cai, S.; Xie, S.; Wang, Z.; Tong, Y.; Pan, M.; Lu, X., Metal–organic-framework-derived dual metal- and nitrogen-doped carbon as efficient and robust oxygen reduction reaction catalysts for microbial fuel cells. *Adv. Sci.* **2016,** *3*, 1500265.

86. Li, Z.; Shao, M.; Zhou, L.; Yang, Q.; Zhang, C.; Wei, M.; Evans, D. G.; Duan, X., Carbon-based electrocatalyst derived from bimetallic metal-organic framework arrays for high performance oxygen reduction. *Nano Energy* **2016,** *25*, 100-109.

87. Kwak, D.-H.; Han, S.-B.; Lee, Y.-W.; Park, H.-S.; Choi, I.-A.; Ma, K.-B.; Kim, M.-C.; Kim, S.-J.; Kim, D.-H.; Sohn, J.-I.; Park, K.-W., Fe/N/S-doped mesoporous carbon nanostructures as electrocatalysts for oxygen reduction reaction in acid medium. *Appl. Catal. B* **2017,** *203*, 889-898.

88. Xiao, M.; Chen, Y.; Zhu, J.; Zhang, H.; Zhao, X.; Gao, L.; Wang, X.; Zhao, J.; Ge, J.; Jiang, Z.; Chen, S.; Liu, C.; Xing, W., Climbing the apex of the ORR volcano plot via binuclear site construction: electronic and geometric engineering. *J. Am. Chem. Soc.* **2019,** *141*, 17763-17770.

89. Zhao, X.; Yang, X.; Wang, M.; Hwang, S.; Karakalos, S.; Chen, M.; Qiao, Z.; Wang, L.; Liu, B.; Ma, Q.; Cullen, D. A.; Su, D.; Yang, H.; Zang, H.-Y.; Feng, Z.; Wu, G., Single-iron site catalysts with self-assembled dual-size architecture and hierarchical porosity for proton-exchange membrane fuel cells. *Appl. Catal. B* **2020,** *279*, 119400.

90. Lefèvre, M.; Proietti, E.; Jaouen, F.; Dodelet, J.-P., Iron-based catalysts with improved oxygen reduction activity in polymer electrolyte fuel cells. *Science* **2009,** *324*, 71-74.

91. Gumeci, C.; Leonard, N.; Liu, Y.; McKinney, S.; Halevi, B.; Barton, S. C., Effect of pyrolysis pressure on activity of Fe–N–C catalysts for oxygen reduction. *J. Mater. Chem. A* **2015,** *3*, 21494-21500.

92. Yu, J.; Chen, G.; Sunarso, J.; Zhu, Y.; Ran, R.; Zhu, Z.; Zhou, W.; Shao, Z., Cobalt oxide and cobalt-graphitic carbon core–shell based catalysts with remarkably high oxygen reduction reaction activity. *Adv. Sci.* **2016,** *3*, 1600060.

93. Guo, D.; Shibuya, R.; Akiba, C.; Saji, S.; Kondo, T.; Nakamura, J., Active sites of nitrogen-doped carbon materials for oxygen reduction reaction clarified using model catalysts. *Science* **2016,** *351*, 361-365.

94. Díaz-Duran, A. K.; Roncaroli, F., MOF derived mesoporous nitrogen doped carbons with high activity towards oxygen reduction. *Electrochim. Acta* **2017,** *251*, 638-650.

95. MacDiarmid, A. G.; Manohar, S. K.; Masters, J. G.; Sun, Y.; Weiss, H.; Epstein, A. J., Polyaniline: Synthesis and properties of pernigraniline base. *Synth. Met.* **1991,** *41*, 621-626.

96. Zhang, W.; Xu, X.; Zhang, C.; Yu, Z.; Zhou, Y.; Tang, Y.; Wu, P.; Guo, S., 3D space-confined pyrolysis of double-network aerogels containing In–Fe cyanogel and polyaniline: a new approach to hierarchically porous carbon with exclusive Fe–N_x active sites for oxygen reduction catalysis. *Small Methods* **2017,** *1*, 1700167.

97. Osmieri, L.; Monteverde Videla, A. H. A.; Specchia, S., Optimization of a Fe–N–C electrocatalyst supported on mesoporous carbon functionalized with polypyrrole for oxygen reduction reaction under both alkaline and acidic conditions. *Int. J. Hydrog. Energy* **2016,** *41*, 19610-19628.

98. Tran, T.-N.; Song, M. Y.; Singh, K. P.; Yang, D.-S.; Yu, J.-S., Iron–polypyrrole electrocatalyst with remarkable activity and stability for ORR in both alkaline and acidic conditions: a comprehensive assessment of catalyst preparation sequence. *J. Mater. Chem. A* **2016,** *4*, 8645-8657.

99. Wang, W.; Luo, J.; Chen, W.; Li, J.; Xing, W.; Chen, S., Synthesis of mesoporous Fe/N/C oxygen reduction catalysts through NaCl crystallite-confined pyrolysis of polyvinylpyrrolidone. *J. Mater. Chem. A* **2016,** *4*, 12768-12773.

100. Stariha, S.; Artyushkova, K.; Workman, M. J.; Serov, A.; McKinney, S.; Halevi, B.; Atanassov, P., PGM-free Fe-N-C catalysts for oxygen reduction reaction: catalyst layer design. *J. Power Sources* **2016,** *326*, 43-49.

101. Anibal, J.; Romero, H. G.; Leonard, N. D.; Gumeci, C.; Halevi, B.; Calabrese Barton, S., Effect of silica morphology on the structure of hard-templated, non-precious metal catalysts for oxygen reduction. *Appl. Catal. B* **2016,** *198*, 32-37.

102. Marzorati, S.; Longhi, M., Templating induced behavior of platinum-free carbons for oxygen reduction reaction. *J. Electroanal. Chem.* **2016,** *775*, 350-355.

103. Sa, Y. J.; Seo, D.-J.; Woo, J.; Lim, J. T.; Cheon, J. Y.; Yang, S. Y.; Lee, J. M.; Kang, D.; Shin, T. J.; Shin, H. S.; Jeong, H. Y.; Kim, C. S.; Kim, M. G.; Kim, T.-Y.; Joo, S. H., A general approach to preferential formation of active Fe–N_x sites in Fe–N/C electrocatalysts for efficient oxygen reduction reaction. *J. Am. Chem. Soc.* **2016,** *138*, 15046-15056.

104. Wang, Y.; Kong, A.; Chen, X.; Lin, Q.; Feng, P., Efficient oxygen electroreduction: Hierarchical porous Fe–N-doped hollow carbon nanoshells. *ACS Catal.* **2015,** *5*, 3887-3893.

105. Serov, A.; Artyushkova, K.; Atanassov, P., Fe-N-C oxygen reduction fuel cell catalyst derived from carbendazim: synthesis, structure, and reactivity. *Adv. Energy Mater.* **2014,** *4*, 1301735.

106. Li, J.-C.; Hou, P.-X.; Shi, C.; Zhao, S.-Y.; Tang, D.-M.; Cheng, M.; Liu, C.; Cheng, H.-M., Hierarchically porous Fe-N-doped carbon nanotubes as efficient electrocatalyst for oxygen reduction. *Carbon* **2016,** *109*, 632-639.

107. Wan, X.; Liu, X.; Li, Y.; Yu, R.; Zheng, L.; Yan, W.; Wang, H.; Xu, M.; Shui, J., Fe–N–C electrocatalyst with dense active sites and efficient mass transport for high-performance proton exchange membrane fuel cells. *Nat. Catal.* **2019,** *2*, 259-268.

108. Pylypenko, S.; Mukherjee, S.; Olson, T. S.; Atanassov, P., Non-platinum oxygen reduction electrocatalysts based on pyrolyzed transition metal macrocycles. *Electrochim. Acta* **2008,** *53*, 7875-7883.

109. Li, C.; Han, Z.; Yu, Y.; Zhang, Y.; Dong, B.; Kong, A.; Shan, Y., Efficient oxygen electroreduction over ordered mesoporous Co–N-doped carbon derived from cobalt porphyrin. *RSC Adv.* **2016,** *6*, 15167-15174.

110. Monteverde Videla, A. H. A.; Osmieri, L.; Armandi, M.; Specchia, S., Varying the morphology of Fe-N-C electrocatalysts by templating iron phthalocyanine precursor with different porous SiO_2 to promote the oxygen reduction reaction. *Electrochim. Acta* **2015,** *177*, 43-50.

111. Kong, A.; Mao, C.; Wang, Y.; Lin, Q.; Bu, X.; Feng, P., Hierarchically porous few-layer porphyrinic carbon nanosheets formed by a VO_x-templating method for high-efficiency oxygen electroreduction. *J. Mater. Chem. A* **2016,** *4*, 7305-7312.

112. Zhu, Z.; Yin, H.; Wang, Y.; Chuang, C.-H.; Xing, L.; Dong, M.; Lu, Y.-R.; Casillas-Garcia, G.; Zheng, Y.; Chen, S.; Dou, Y.; Liu, P.; Cheng, Q.; Zhao, H., Coexisting single-atomic Fe and Ni sites on hierarchically ordered porous carbon as a highly efficient ORR electrocatalyst. *Adv. Mater.* **2020,** *30*, 2004670.

113. Zhao, D.; Shui, J. L.; Grabstanowicz, L. R.; Chen, C.; Commet, S. M.; Xu, T.; Lu, J.; Liu, D. J., Highly efficient non-precious metal electrocatalysts prepared from one-pot synthesized zeolitic imidazolate frameworks. *Adv. Mater.* **2014,** *26*, 1093-1097.

114. Zhou, H. C.; Long, J. R.; Yaghi, O. M., Introduction to metal-organic frameworks. *Chem. Rev.* **2012,** *112*, 673-674.

115. Armel, V.; Hindocha, S.; Salles, F.; Bennett, S.; Jones, D.; Jaouen, F., Structural descriptors of zeolitic-imidazolate frameworks are keys to the activity of Fe-N-C catalysts. *J. Am. Chem. Soc.* **2017,** *139*, 453-464.

116. Zhan, Y.; Xie, F.; Zhang, H.; Jin, Y.; Meng, H.; Chen, J.; Sun, X., Highly dispersed nonprecious metal catalyst for oxygen reduction reaction in proton exchange membrane fuel cells. *ACS Appl. Mater. Interfaces* **2020,** *12*, 17481-17491.

117. You, C.; Zheng, R.; Shu, T.; Liu, L.; Liao, S., High porosity and surface area self-doped carbon derived from polyacrylonitrile as efficient electrocatalyst towards oxygen reduction. *J. Power Sources* **2016,** *324*, 134-141.

118. Li, X.; Zhao, Y.; Yang, Y.; Gao, S., A universal strategy for carbon–based ORR–active electrocatalyst: one porogen, two pore–creating mechanisms, three pore types. *Nano Energy* **2019,** *62*, 628-637.

119. Yakub, I.; Mohammad, M.; Yaakob, Z., Effects of zinc chloride impregnation on the characteristics of activated carbon produced from physic nut seed hull. *Adv. Mat. Res.* **2013,** *626*, 751-755.

120. Ahmadpour, A.; Do, D. D., The preparation of activated carbon from macadamia nutshell by chemical activation. *Carbon* **1997,** *35*, 1723-1732.

121. Nakagawa, Y.; Molina-Sabio, M.; Rodríguez-Reinoso, F., Modification of the porous structure along the preparation of activated carbon monoliths with H_3PO_4 and $ZnCl_2$. *Microporous Mesoporous Mater.* **2007,** *103*, 29-34.

122. Benziger, J. B.; Satterfield, M. B.; Hogarth, W. H. J.; Nehlsen, J. P.; Kevrekidis, I. G., The power performance curve for engineering analysis of fuel cells. *J. Power Sources* **2006,** *155*, 272-285.

123. Khotseng, L., Oxygen Reduction Reaction. In *Electrocatalysts for Fuel Cells and Hydrogen Evolution - Theory to Design*, 2018.

124. Treimer, S.; Tang, A.; Johnson, D. C., A consideration of the application of Koutecký-Levich plots in the diagnoses of charge-transfer mechanisms at rotated disk electrodes. *Electroanalysis* **2002,** *14*, 165-171.

125. Artyushkova, K.; Serov, A.; Rojas-Carbonell, S.; Atanassov, P., Chemistry of multitudinous active sites for oxygen reduction reaction in transition metal–nitrogen–carbon electrocatalysts. *J. Phys. Chem. C* **2015,** *119*, 25917-25928.

126. Choi, C. h.; Choi, W. S.; Kasian, O.; Mechler, A.; Sougrati, M. T.; Brüller, S.; Strickland, K.; Jia, Q.; Mukerjee, S.; Mayrhofer, K.; Jaouen, F., Unraveling the nature of sites active toward hydrogen peroxide reduction in Fe-N-C catalysts. *Angew. Chem. Int. Ed.* **2017,** *56*, 8809 –8812.

127. Kattel, S.; Wang, G., Reaction pathway for oxygen reduction on FeN_4 embedded graphene. *J. Phys. Chem. Lett.* **2014,** *5*, 452-456.

128. Kattel, S.; Atanassov, P.; Kiefer, B., A density functional theory study of oxygen reduction reaction on non-PGM Fe–N_x–C electrocatalysts. *Phys. Chem. Chem. Phys.* **2014,** *16*, 13800-13806.

129. Wang, Y.; Tang, Y.-J.; Zhou, K., Self-ajusting activity induced by intrinsic reaction intermediate in Fe–N–C single-atom catalysts. *J. Am. Chem. Soc.* **2019,** *141*, 14115-14119.

130. Han, Y.; Li, Q.-K.; Ye, K.; Luo, Y.; Jiang, J.; Zhang, G., Impact of active site density on oxygen reduction reactions using monodispersed Fe–N–C single-atom catalysts. *ACS Appl. Mater. Interfaces* **2020,** *12*, 15271-15278.

131. Zhong, L.; Li, S., Unconventional oxygen reduction reaction mechanism and scaling relation on single-atom catalysts. *ACS Catal.* **2020,** *10*, 4313-4318.

132. Xu, P.; Chen, W.; Wang, Q.; Zhu, T.; Wu, M.; Qiao, J.; Chen, Z.; Zhang, J., Effects of transition metal precursors (Co, Fe, Cu, Mn, or Ni) on pyrolyzed carbon supported metal-aminopyrine electrocatalysts for oxygen reduction reaction. *RSC Adv.* **2015,** *5*, 6195-6206.

133. Jia, Q.; Ramaswamy, N.; Hafiz, H.; Tylus, U.; Strickland, K.; Wu, G.; Barbiellini, B.; Bansil, A.; Holby, E. F.; Zelenay, P.; Mukerjee, S., Experimental observation of redox-induced Fe–N switching behavior as a determinant role for oxygen reduction activity. *ACS Nano* **2015,** *9*, 12496-12505.

134. Peng, Y.; Li, Z.; Xia, D.; Zheng, L.; Liao, Y.; Li, K.; Zuo, X., Probing the influence of the center atom coordination structure in iron phthalocyanine multi-walled carbon nanotube-based oxygen reduction reaction catalysts by X-ray absorption fine structure spectroscopy. *J. Power Sources* **2015,** *291*, 20-28.

135. Marshall-Roth, T.; Libretto, N. J.; Wrobel, A. T.; Anderton, K. J.; Pegis, M. L.; Ricke, N. D.; Voorhis, T. V.; Miller, J. T.; Surendranath, Y., A pyridinic Fe-N_4 macrocycle models the active sites in Fe/N-doped carbon electrocatalysts. *Nat. Commun.* **2020,** *11*, 5283.

136. Sougrati, M. T.; Goellner, V.; Schuppert, A. K.; Stievano, L.; Jaouen, F., Probing active sites in iron-based catalysts for oxygen electro-reduction: a temperature-dependent ^{57}Fe Mössbauer spectroscopy study. *Catal. Today* **2016,** *262*, 110-120.

137. Li, J.; Jaouen, F., Structure and activity of metal-centered coordination sites in pyrolyzed metal–nitrogen–carbon catalysts for the electrochemical reduction of O_2. *Curr. Opin. Electrochem.* **2018,** *9*, 198-206.

138. Holby, E. F.; Zelenay, P., Linking structure to function: the search for active sites in non-platinum group metal oxygen reduction reaction catalysts. *Nano Energy* **2016,** *29*, 54-64.

139. Armel, V.; Hannauer, J.; Jaouen, F., Effect of ZIF-8 crystal size on the O_2 electro-reduction performance of prolyzed Fe–N–C catalysts. *Catalysts* **2015,** *5*, 1333-1351.

140. Segall, M. D.; Lindan, P. J. D.; Probert, M. J.; Pickard, C. J.; Hasnip, P. J.; Clark, S. J.; Payne, M. C., First-principles simulation: ideas, illustrations and the CASTEP code. *J. Phys. Condens. Matter* **2002,** *14*, 2717-2744.

141. Perdew, J. P.; Burke, K.; Ernzerhof, M., Generalized gradient approximation made simple. *Phys. Rev. Lett.* **1997,** *78*, 1396-1396.

142. Cococcioni, M.; de Gironcoli, S., Linear response approach to the calculation of the effective interaction parameters in the LDA+U method. *Phys. Rev. B* **2005,** *71*, 035105.

143. Kattel, S.; Atanassov, P.; Kiefer, B., Stability, electronic and magnetic properties of in-plane defects in graphene: a first-principles study. *J. Phys. Chem. C* **2012,** *116*, 8161-8166.

144. Al-Zoubi, T.; Zhou, Y.; Yin, X.; Janicek, B.; Sun, C.; Schulz, C. E.; Zhang, X.; Gewirth, A. A.; Huang, P.; Zelenay, P.; Yang, H., Preparation of nonprecious metal electrocatalysts for the reduction of oxygen using a low-temperature sacrificial metal. *J. Am. Chem. Soc.* **2020,** *142*, 5477-5481.

145. German, R. M., 1 - Thermodynamics of sintering. In *Sintering of Advanced Materials*, Fang, Z. Z., Ed. Woodhead Publishing: 2010; pp 3-32.

146. He, Y.; Liu, S.; Priest, C.; Shi, Q.; Wu, G., Atomically dispersed metal–nitrogen–carbon catalysts for fuel cells: advances in catalyst design, electrode performance, and durability improvement. *Chem. Soc. Rev.* **2020,** *49*, 3484-3524.

147. Wang, Q.; Ina, T.; Chen, W.-T.; Shang, L.; Sun, F.; Wei, S.; Sun-Waterhouse, D.; Telfer, S. G.; Zhang, T.; Waterhouse, G. I. N., Evolution of Zn(II) single atom catalyst sites during the pyrolysis-induced transformation of ZIF-8 to N-doped carbons. *Sci. Bull.* **2020,** *65*, 1743-1751.

148. Li, A.; Tong, Y.; Song, H.; Chen, X., Compositional and structural evolutions of Zn-based metal–organic frameworks during pyrolysis. *J. Phys. Chem. C* **2018,** *122*, 17278-17286.

149. Ma, S.; Goenaga Gabriel, A.; Call Ann, V.; Liu, D. J., Cobalt imidazolate framework as precursor for oxygen reduction reaction electrocatalysts. *Chem. Eur. J.* **2011,** *17*, 2063-2067.

150. Barkholtz, H. M.; Chong, L.; Kaiser, Z. B.; Liu, D. J., Non-precious metal catalysts prepared by zeolitic imidazolate frameworks: the ligand influence to morphology and performance. *Fuel Cells* **2016,** *16*, 428-433.

151. Zhang, G.; Chenitz, R.; Lefèvre, M.; Sun, S.; Dodelet, J.-P., Is iron involved in the lack of stability of Fe/N/C electrocatalysts used to reduce oxygen at the cathode of PEM fuel cells? *Nano Energy* **2016,** *29*, 111-125.

152. Gu, W.; Hu, L.; Li, J.; Wang, E., Hybrid of g-C_3N_4 assisted metal–organic frameworks and their derived high-efficiency oxygen reduction electrocatalyst in the whole pH range. *ACS Appl. Mater. Interfaces* **2016,** *8*, 35281-35288.

153. Lai, Q.; Zheng, L.; Liang, Y.; He, J.; Zhao, J.; Chen, J., Metal–organic-framework-derived Fe-N/C electrocatalyst with five-coordinated Fe-N_x sites for advanced oxygen reduction in acid media. *ACS Catal.* **2017,** *7*, 1655-1663.

154. Wang, J.; Huang, Z.; Liu, W.; Chang, C.; Tang, H.; Li, Z.; Chen, W.; Jia, C.; Yao, T.; Wei, S.; Wu, Y.; Li, Y., Design of N-coordinated dual-metal sites: a stable and active Pt-free catalyst for acidic oxygen reduction reaction. *J. Am. Chem. Soc.* **2017,** *139*, 17281-17284.

155. Zhang, H.; Chung, H. T.; Cullen, D. A.; Wagner, S.; Kramm, U. I.; More, K. L.; Zelenay, P.; Wu, G., High-performance fuel cell cathodes exclusively containing atomically dispersed iron active sites. *Energ. Environ. Sci.* **2019,** *12*, 2548-2558.

156. Zhang, H.; Ding, S.; Hwang, S.; Zhao, X.; Su, D.; Xu, H.; Yang, H.; Wu, G., Atomically dispersed iron cathode catalysts derived from binary ligand-based zeolitic imidazolate frameworks with enhanced stability for PEM fuel cells. *J. Electrochem. Soc.* **2019,** *166*, F3116-F3122.

157. Chen, M.; Li, X.; Yang, F.; Li, B.; Stracensky, T.; Karakalos, S.; Mukerjee, S.; Jia, Q.; Su, D.; Wang, G.; Wu, G.; Xu, H., Atomically dispersed MnN_4 catalysts via environmentally benign aqueous synthesis for oxygen reduction: mechanistic understanding of activity and stability improvements. *ACS Catal.* **2020,** *10*, 10523-10534.

158. Park, K.; Jin, S.-A.; Lee, K. H.; Lee, J.; Song, I.; Lee, B.-S.; Kim, S.; Sohn, J.-S.; Pak, C.; Kim, G.; Doo, S.-G.; Kwon, K., Characterization of zeolitic imidazolate framework–derived polyhedral carbonaceous material and its application to electrocatalyst for oxygen reduction reaction. *Int. J. Electrochem. Sci.* **2016,** *11*, 9295-9306.

159. Liu, T.; Zhao, P.; Hua, X.; Luo, W.; Chen, S.; Cheng, G., An Fe–N–C hybrid electrocatalyst derived from a bimetal–organic framework for efficient oxygen reduction. *J. Mater. Chem. A* **2016,** *4*, 11357-11364.

160. Zuo, Q.; Zhao, P.; Luo, W.; Cheng, G., Hierarchically porous Fe–N–C derived from covalent-organic materials as a highly efficient electrocatalyst for oxygen reduction. *Nanoscale* **2016,** *8*, 14271-14277.

161. Chong, L.; Goenaga, G. A.; Williams, K.; Barkholtz, H. M.; Grabstanowicz, L. R.; Brooksbank, J. A.; Papandrew, A. B.; Elzein, R.; Schlaf, R.; Zawodzinski Jr., T. A.; Zou, J.; Ma, S.; Liu, D.-J., Investigation of oxygen reduction activity of catalysts derived from Co and Co/Zn methyl-imidazolate frameworks in proton exchange membrane fuel cells. *ChemElectroChem* **2016,** *3*, 1541-1545.

162. Jaouen, F.; Goellner, V.; Armel, V.; Zitolo, A.; Fonda, E., Degradation by hydrogen peroxide of metal-nitrogen-carbon catalysts for oxygen reduction. *J. Electrochem. Soc.* **2015,** *162*, H403-H414.

163. Liu, D.; Li, J.-C.; Ding, S.; Lyu, Z.; Feng, S.; Tian, H.; Huyan, C.; Xu, M.; Li, T.; Du, D.; Liu, P.; Shao, M.; Lin, Y., 2D single-atom catalyst with optimized iron sites produced by thermal melting of metal–organic frameworks for oxygen reduction reaction. *Small Methods* **2020,** *4*, 1900827.

164. Zheng, L.; Yu, S.; Lu, X.; Fan, W.; Chi, B.; Ye, Y.; Shi, X.; Zeng, J.; Li, X.; Liao, S., Two-dimensional bimetallic Zn/Fe-metal-organic framework (MOF)-derived porous carbon nanosheets with a high density of single/paired Fe atoms as high-performance oxygen reduction catalysts. *ACS Appl. Mater. Interfaces* **2020,** *12*, 13878-13887.

165. Huang, J.-W.; Cheng, Q.-Q.; Huang, Y.-C.; Yao, H.-C.; Zhu, H.-B.; Yang, H., Highly efficient Fe–N–C electrocatalyst for oxygen reduction derived from core–shell-structured $Fe(OH)_3$@zeolitic imidazolate framework. *ACS Appl. Energy Mater.* **2019,** *2*, 3194-3203.

166. Xiao, M.; Zhu, J.; Ma, L.; Jin, Z.; Ge, J.; Deng, X.; Hou, Y.; He, Q.; Li, J.; Jia, Q.; Mukerjee, S.; Yang, R.; Jiang, Z.; Su, D.; Liu, C.; Xing, W., Microporous framework induced synthesis of single-atom dispersed Fe-N-C acidic ORR catalyst and its in situ reduced Fe-N_4 active site identification revealed by X-ray absorption spectroscopy. *ACS Catal.* **2018,** *8*, 2824-2832.

167. Fujiwara, Y.-i.; Lee, J.-S. M.; Tsujimoto, M.; Kongpatpanich, K.; Pila, T.; Iimura, K.-i.; Tobori, N.; Kitagawa, S.; Horike, S., Fabrication of ε-Fe_2N catalytic sites in porous carbons derived from an iron–triazolate crystal. *Chem. Mater.* **2018,** *30*, 1830-1834.

168. Wang, X. X.; Cullen, D. A.; Pan, Y.-T.; Hwang, S.; Wang, M.; Feng, Z.; Wang, J.; Engelhard, M. H.; Zhang, H.; He, Y.; Shao, Y.; Su, D.; More, K. L.; Spendelow, J. S.; Wu, G., Nitrogen-coordinated single cobalt atom catalysts for oxygen reduction in proton exchange membrane fuel cells. *Adv. Mat.* **2018,** *30*, 1706758.

169. Wu, M.; Hu, X.; Li, C.; Li, J.; Zhou, H.; Zhang, X.; Liu, R., Encapsulation of metal precursor within ZIFs for bimetallic N-doped carbon electrocatalyst with enhanced oxygen reduction. *Int. J. Hydrog. Energy* **2018,** *43*, 14701-14709.

170. Meng, Z.; Cai, S.; Wang, R.; Tang, H.; Song, S.; Tsiakaras, P., Bimetallic−organic framework-derived hierarchically porous Co-Zn-N-C as efficient catalyst for acidic oxygen reduction reaction. *Appl. Catal. B* **2019,** *244*, 120-127.

171. Lai, S.; Xu, L.; Liu, H.; Chen, S.; Cai, R.; Zhang, L.; Theis, W.; Sun, J.; Yang, D.; Zhao, X., Controllable synthesis of CoN_3 catalysts derived from Co/Zn-ZIF-67 for electrocatalytic oxygen reduction in acidic electrolytes. *J. Mater. Chem. A* **2019,** *7*, 21884-21891.

172. Wang, H.; Yin, F.-X.; Liu, N.; Kou, R.-H.; He, X.-B.; Sun, C.-J.; Chen, B.-H.; Liu, D.-J.; Yin, H.-Q., Engineering Fe–Fe_3C@Fe–N–C active sites and hybrid structures from dual metal–organic frameworks for oxygen reduction reaction in H_2–O_2 fuel cell and Li–O_2 battery. *Adv. Funct. Mater.* **2019,** *29*, 1901531.

173. Jin, H.; Zhou, H.; He, D.; Wang, Z.; Wu, Q.; Liang, Q.; Liu, S.; Mu, S., MOF-derived 3D Fe-N-S co-doped carbon matrix/nanotube nanocomposites with advanced oxygen reduction activity and stability in both acidic and alkaline media. *Appl. Catal. B* **2019,** *250*, 143-149.

174. Choi, I.-H.; Kim, Y.; Lee, D. N.; Huh, S., Three-dimensional cobalt(II) and cadmium(II) MOFs containing 1,4-naphthalenedicarboxylate: catalytic activity of Cd-MOF. *Polyhedron* **2016,** *105*, 96-103.

175. Pachfule, P.; Banerjee, R., Porous nitrogen rich cadmium-tetrazolate based metal organic framework (MOF) for H_2 and CO_2 uptake. *Cryst. Growth Des.* **2011,** *11*, 5176-5181.

176. Yue, M.-L.; Jiang, Y.-F.; Zhang, L.; Yu, C.-Y.; Zou, K.-Y.; Li, Z.-X., Solvent-induced cadmium(II) metal-organic frameworks with adjustable guest-evacuated porosity: application in the controllable assembly of MOF-derived porous carbon materials for supercapacitors. *Chem. Eur. J.* **2017,** *23*, 15680-15693.

177. Yin, X.; Lin, L.; Chung, H. T.; Komini Babu, S.; Martinez, U.; Purdy, G. M.; Zelenay, P., Effects of MEA fabrication and ionomer composition on fuel cell performance of PGM-free ORR catalyst. *ECS Trans.* **2017,** *77*, 1273-1281.

178. Nishimaki, K.; Ohmae, S.; Yamamoto, T. A.; Katsura, M., Formation of iron-nitrides by the reaction of iron nanoparticles with a stream of ammonia. *Nanostruct. Mater.* **1999,** *12*, 527-530.

179. Martinez, U.; Komini Babu, S.; Holby, E. F.; Chung, H. T.; Yin, X.; Zelenay, P., Fe–N–C catalysts: progress in the development of Fe-based PGM-free electrocatalysts for the oxygen reduction reaction. *Adv. Mat.* **2019,** *31*, 1970224.

180. Jasinski, R., A new fuel cell cathode catalyst. *Nature* **1964,** *201*, 1212-1213.

181. Chen, M.; He, Y.; Spendelow, J. S.; Wu, G., Atomically dispersed metal catalysts for oxygen reduction. *ACS Energy Lett.* **2019,** *4*, 1619-1633.

182. Chen, Y.; Ji, S.; Chen, C.; Peng, Q.; Wang, D.; Li, Y., Single-atom catalysts: synthetic strategies and electrochemical applications. *Joule* **2018,** *2*, 1242-1264.

183. Ferrandon, M.; Wang, X.; Kropf, A. J.; Myers, D. J.; Wu, G.; Johnston, C. M.; Zelenay, P., Stability of iron species in heat-treated polyaniline–iron–carbon polymer electrolyte fuel cell cathode catalysts. *Electrochim. Acta* **2013,** *110*, 282-291.

184. Tang, X.; Li, H.; Du, Z.; Ng, H. Y., Polyaniline and iron based catalysts as air cathodes for enhanced oxygen reduction in microbial fuel cells. *RSC Adv.* **2015,** *5*, 79348-79354.

185. Han, Y.; Wang, Y.-G.; Chen, W.; Xu, R.; Zheng, L.; Zhang, J.; Luo, J.; Shen, R.-A.; Zhu, Y.; Cheong, W.-C.; Chen, C.; Peng, Q.; Wang, D.; Li, Y., Hollow N-doped carbon spheres with isolated cobalt single atomic sites: superior electrocatalysts for oxygen reduction. *J. Am. Chem. Soc.* **2017,** *139*, 17269-17272.

186. Dybtsev, D. N.; Chun, H.; Kim, K., Rigid and flexible: a highly porous metal–organic framework with unusual guest-dependent dynamic behavior. *Angew. Chem. Int. Ed.* **2004,** *43*, 5033-5036.

187. Jagadeesh, R. V.; Murugesan, K.; Alshammari, A. S.; Neumann, H.; Pohl, M.-M.; Radnik, J.; Beller, M., MOF-derived cobalt nanoparticles catalyze a general synthesis of amines. *Science* **2017,** *358*, 326-332.

188. Nixon, D., *Order-disorder transformations in graphite nitrates*. Proceedings of the Royal Society A: Mathematical, Physical and Engineering Sciences: 1966; Vol. 291.

189. Holade, Y.; Morais, C.; Servat, K.; Napporn, T. W.; Kokoh, K. B., Enhancing the available specific surface area of carbon supports to boost the electroactivity of nanostructured Pt catalysts. *Phys. Chem. Chem. Phys.* **2014,** *16*, 25609-25620.

190. Martins Ferreira, E. H.; Moutinho, M. V. O.; Stavale, F.; Lucchese, M. M.; Capaz, R. B.; Achete, C. A.; Jorio, A., Evolution of the Raman spectra from single-, few-, and many-layer graphene with increasing disorder. *Phys. Rev. B* **2010,** *82*, 125429.

191. Saito, R.; Hofmann, M.; Dresselhaus, G.; Jorio, A.; Dresselhaus, M. S., Raman spectroscopy of graphene and carbon nanotubes. *Adv. Phys.* **2011,** *60*, 413-550.

192. Yan, P.; Zhang, B.; Wu, K.-H.; Su, D.; Qi, W., Surface chemistry of nanocarbon: characterization strategies from the viewpoint of catalysis and energy conversion. *Carbon* **2019,** *143*, 915-936.

193. Weiss, J.; Zhang, H.; Zelenay, P., Recent progress in the durability of Fe-N-C oxygen reduction electrocatalysts for polymer electrolyte fuel cells. **2020**, 114696.

194. Kumar, K.; Gairola, P.; Lions, M.; Ranjbar-Sahraie, N.; Mermoux, M.; Dubau, L.; Zitolo, A.; Jaouen, F.; Maillard, F., Physical and chemical considerations for improving catalytic activity and stability of non-precious-metal oxygen reduction reaction catalysts. *ACS Catal.* **2018,** *8*, 11264-11276.

195. Kumar, K.; Dubau, L.; Mermoux, M.; Li, J.; Zitolo, A.; Nelayah, J.; Jaouen, F.; Maillard, F., On the influence of oxygen on the degradation of Fe-N-C catalysts. *Angew. Chem. Int. Ed.* **2020,** *59*, 3235-3243.

196. Yin, X.; Zelenay, P., Kinetic models for the degradation mechanisms of PGM-free ORR catalysts. *ECS Trans.* **2018,** *85*, 1239-1250.

197. Santori, P. G.; Speck, F. D.; Li, J.; Zitolo, A.; Jia, Q.; Mukerjee, S.; Cherevko, S.; Jaouen, F., Effect of pyrolysis atmosphere and electrolyte pH on the oxygen reduction activity, stability and spectroscopic signature of FeN_x moieties in Fe-N-C catalysts. *J. Electrochem. Soc.* **2019,** *166*, F3311-F3320.

198. Choi, C. H.; Baldizzone, C.; Polymeros, G.; Pizzutilo, E.; Kasian, O.; Schuppert, A. K.; Ranjbar Sahraie, N.; Sougrati, M.-T.; Mayrhofer, K. J. J.; Jaouen, F., Minimizing operando demetallation of Fe-N-C electrocatalysts in acidic medium. *ACS Catal.* **2016,** *6*, 3136-3146.

199. Chenitz, R.; Kramm, U. I.; Lefèvre, M.; Glibin, V.; Zhang, G.; Sun, S.; Dodelet, J.-P., A specific demetalation of $Fe–N_4$ catalytic sites in the micropores of NC_Ar + NH_3 is at the origin of the initial activity loss of the highly active Fe/N/C catalyst used for the reduction of oxygen in PEM fuel cells. *Energy Environ. Sci.* **2018,** *11*, 365-382.

200. Qiao, Z.; Hwang, S.; Li, X.; Wang, C.; Samarakoon, W.; Karakalos, S.; Li, D.; Chen, M.; He, Y.; Wang, M.; Liu, Z.; Wang, G.; Zhou, H.; Feng, Z.; Su, D.; Spendelow, J. S.; Wu, G., 3D porous graphitic nanocarbon for enhancing the performance and durability of Pt catalysts: a balance between graphitization and hierarchical porosity. *Energy Environ. Sci.* **2019,** *12*, 2830-2841.

201. Domínguez, C.; Pérez-Alonso, F. J.; Salam, M. A.; Al-Thabaiti, S. A.; Peña, M. A.; García-García, F. J.; Barrio, L.; Rojas, S., Repercussion of the carbon matrix for the activity and stability of Fe/N/C electrocatalysts for the oxygen reduction reaction. *Appl. Catal. B* **2016,** *183*, 185-196.

APPENDIX A

Fe-C-N_T electrocatalysts derived from Zn-Fe-DABCO-TPA

In this section, the work on using the MOF Zn-Fe-DABCO-TPA as the precursor for the synthesis of non-PGM ORR electrocatalysts labeled as ZnDT/Fe_T is presented. This work provided an additional avenue through which to compare the effect of cadmium and zinc as sacrificial metals within MOF structures on the structure-property understanding of non-PGM ORR electrocatalysts.

The catalyst materials were synthesized according to the same protocol outlined in Chapter 3 under the "Material synthesis" subsection; however, zinc was used instead of cadmium in the making of the MOF precursor; the precursor used was $Zn(NO_3)_2 \cdot 6H_2O$ (0.480 g). The catalyst inks for electrochemical measurements were prepared according to the protocol outlined in Chapter 3 in the "Electrochemical analysis" subsection.

As shown below, **Figure A.1** shows the TEM micrograph of ZnDT/Fe_{950} depicting the porous carbon structure characteristic of MOF-derived non-PGM ORR electrocatalysts. The ICP results in **Table A.1** indicate that ZnDT/Fe_{750} contained near 7.06 wt. % of zinc most likely due to the low pyrolysis temperature of 750 °C; at a pyrolysis temperature of 950 °C, the remaining zinc in the sample was 0.03 wt. % which was negligible, indicating near removal of the sacrificial metal in the material. **Figure A.2** shows the LSV polarization curves of both ZnDT/Fe_{750} and ZnDT/Fe_{950} electrocatalysts. While, ZnDT/Fe_{750} was shown to be inactive, ZnDT/Fe_{950} exhibited an onset-potential of 0.88 V vs RHE and a half-wave potential of 0.79 V vs the RHE which was similar to the cadmium MOF-derived electrocatalyst synthesized at a similar temperature. The nitrogen 1s XPS results in **Figure A.3** portray that ZnDT/Fe_{950} contained similar structures of pyridinic and metal-nitrogen structures which can contribute to the high activity observed in these materials.

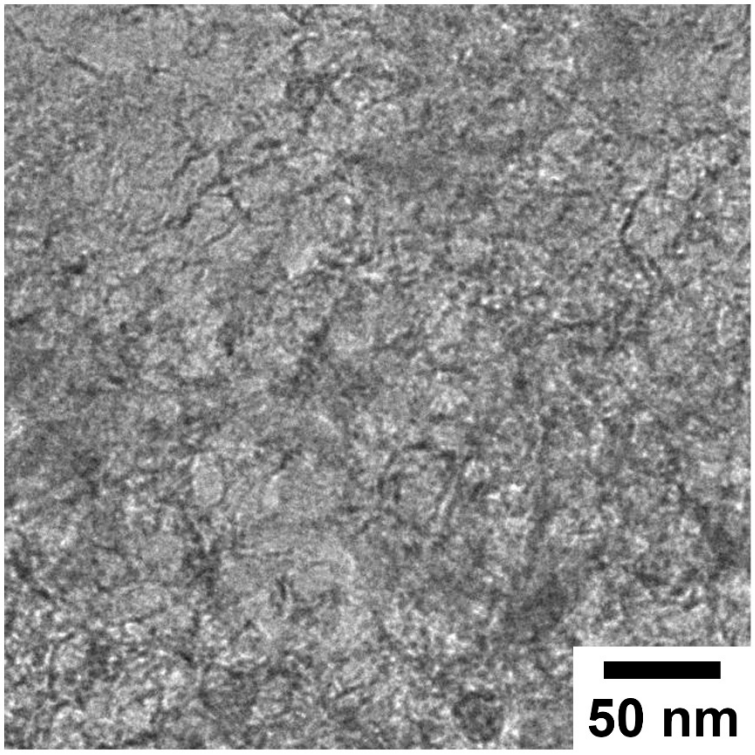

Figure A.1 TEM micrograph of ZnDT/Fe_{950}.

Table A.1 ICP-MS results of the Zn and Fe weight percentages of ZnDT/Fe_{750} and ZnDT/Fe_{950}.

	Zn (wt. %)	**Fe (wt. %)**
ZnDT/Fe_{750}	7.06	3.62
ZnDT/Fe_{950}	0.03	2.3

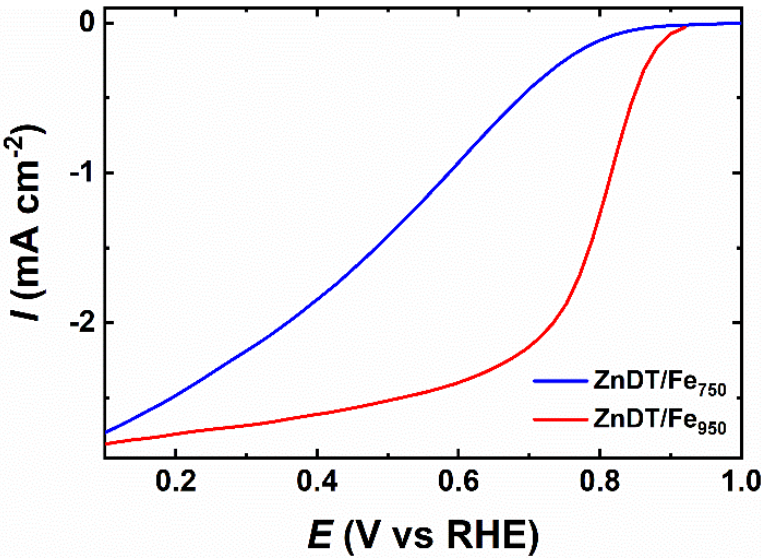

Figure A.2 Staircase voltammograms of ZnDT/Fe_{750} and ZnDT/Fe_{950}.

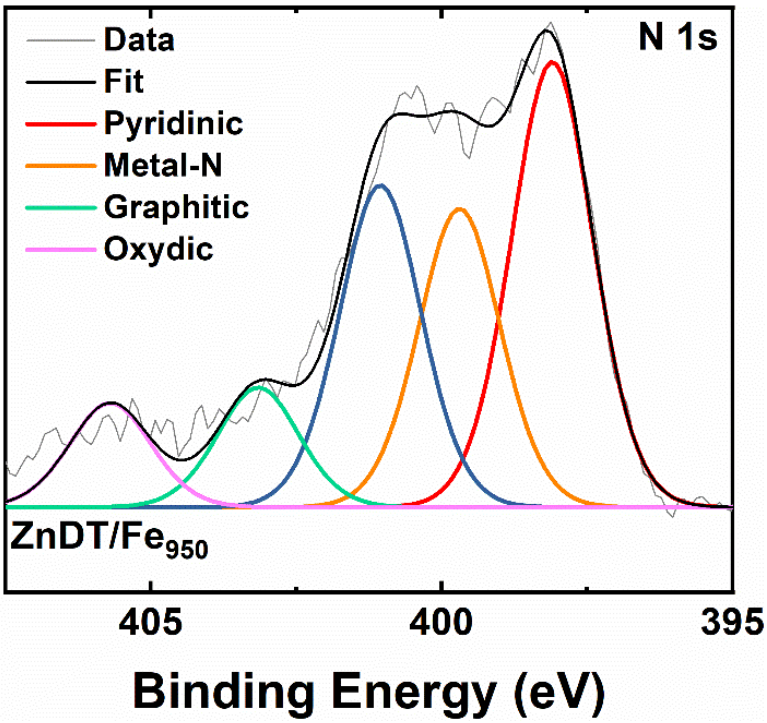

Figure A.3 Staircase voltammograms of ZnDT/Fe_{750} and ZnDT/Fe_{950}.

APPENDIX B

Study of alternative active metals in non-PGM ORR electrocatalysts

Alternative metals to iron such as cobalt and manganese have been shown to be active towards the ORR and are typically used in the synthesis of non-PGM electrocatalysts. The catalyst materials were synthesized using a similar protocol outlined in Chapter 3 under the "Material synthesis" subsection; in this case, zinc was used instead of cadmium as the sacrificial metal while cobalt and copper were used to as alternatives to iron as the active metals. The precursors used were $Co(NO_3)_2 \cdot 6H_2O$ (0.0058 g) and $Cu(NO_3)_2 \cdot 2.5H_2O$ (0.0047 g) respectively. The catalyst inks for electrochemical measurements were prepared according to the protocol outlined in Chapter 3 in the "Electrochemical analysis" subsection. As shown in **Figure C.1**, ZnDT/Fe_{950} exhibited the highest activity followed by ZnDT/Co_{950} while ZnDT/Cu_{950} appeared to be inactive.

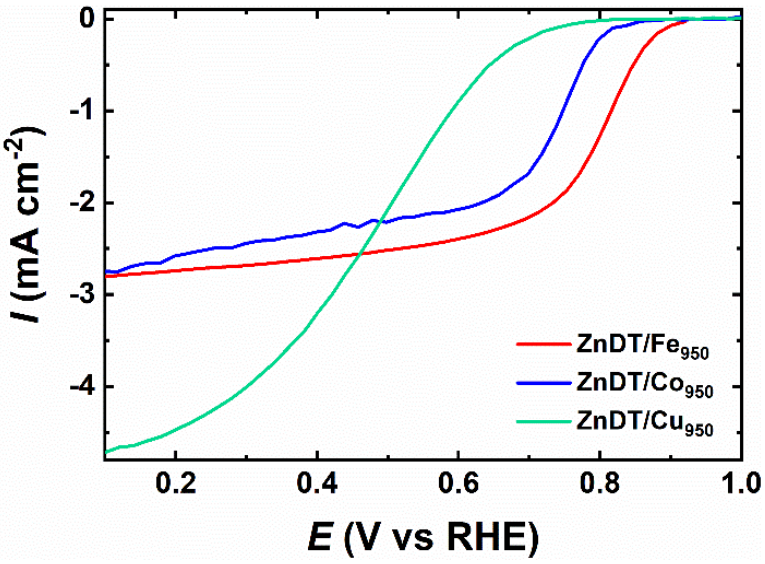

Figure B.1 Staircase voltammograms of ZnDT/Fe_{950}, ZnDT/Co_{950}, and ZnDT/Cu_{950}.

The effect of pyrolysis temperature was investigated on cobalt-based electrocatalysts derived from the MOF Cd-Co-DABCO-TPA. The MOF precursor was synthesized in accordance with a similar procedure outlined in Chapter 3 under the "Materials synthesis" subsection with the substitution of iron with cobalt. Below, **Figure B.2** depicts the SEM image of Cd-Co-DABCO-TPA showing an overall orthorhombic structure with an edge length of approximately 5 μm. The cobalt-based electrocatalysts labeled as Co-C-N_T, where T = pyrolysis temperature was synthesized according to a procedure outlined in Chapter 3 under the "Materials synthesis" subsection. The TEM micrograph of the resultant structure for Co-C-N_{950} is shown in **Figure B.3** which shows the highly porous structure of the carbon support. The PXRD data shown in **Figure B.4** which portrays the Co-C-N_{950} exhibited higher activity than Co-C-N_{750} as shown in **Figure B.5** with an onset potential of 0.80 V vs the RHE and a half-wave potential of 0.69 V vs the RHE compared to an onset potential for the low temperature sample of 0.78 V vs the RHE and a half-wave potential of 0.64 V vs the RHE.

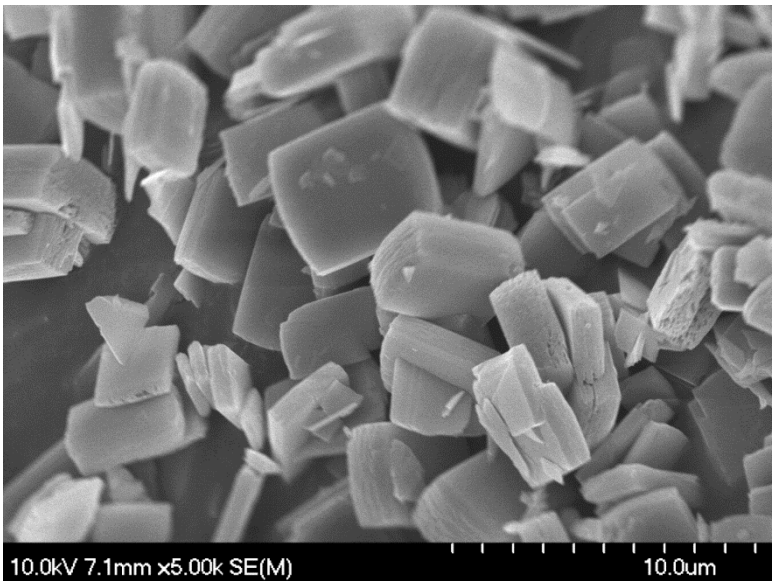

Figure B.2 SEM image of the Cd-Co-DABCO-TPA MOF.

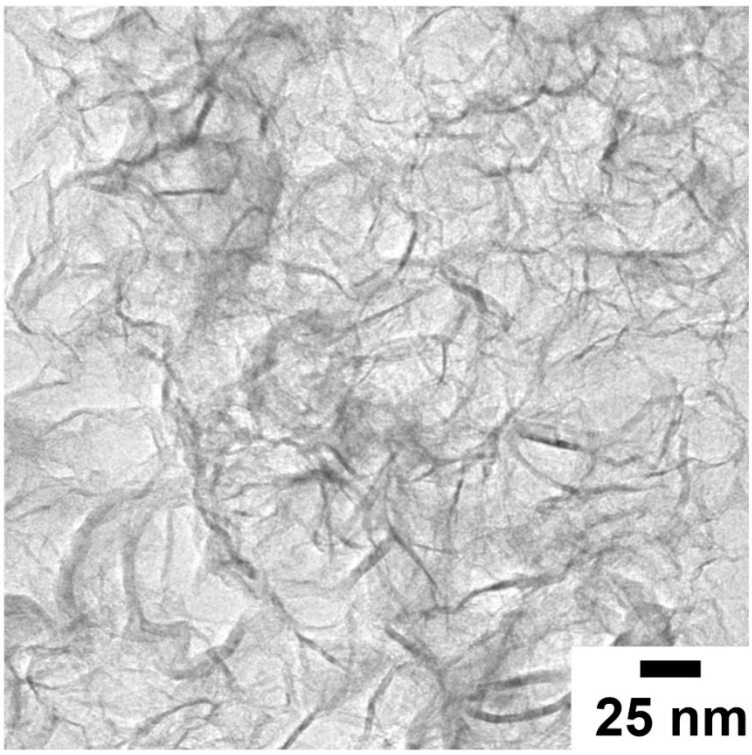

Figure B.3 TEM micrograph of the MOF-derived carbon structure in Co-C-N_{950}.

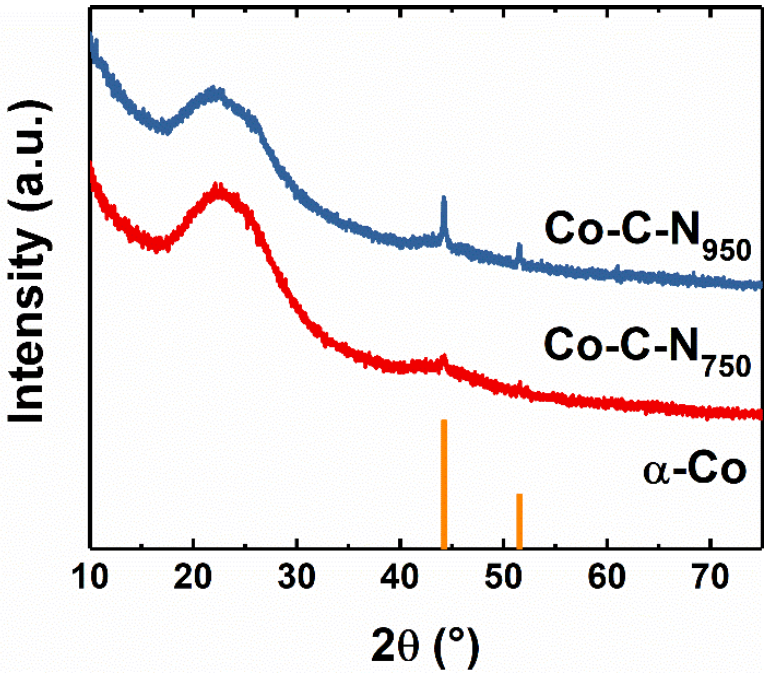

Figure B.4 PXRD of the Co-C-N_{750} and Co-C-N_{950} showing the formation of reduced cobalt structures.

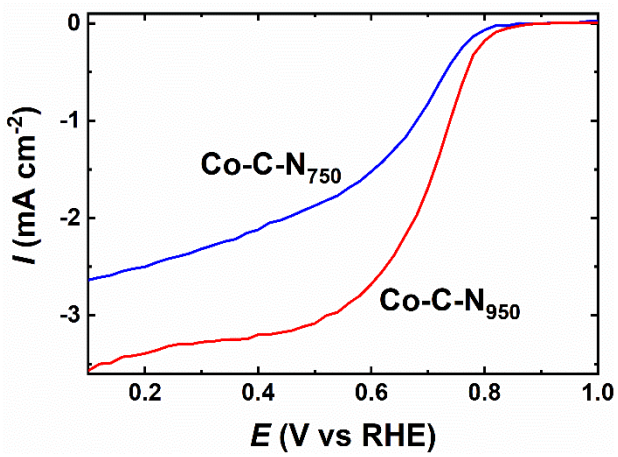

Figure B.5 Staircase voltammograms of Co-C-N_{750} and Co-C-N_{950}.

APPENDIX C

MOF-derived carbon as a support for the synthesis of non-PGM ORR electrocatalysts

As mentioned, there are multiple processes that take place during pyrolysis of MOFs in the synthesis of non-PGM ORR electrocatalysts. These include but are not limited to the removal of the sacrificial metal, the diffusion of metal species for the formation of active structures, formation of carbon during the breakdown of the MOF structure. Attempting to isolate and understand each of these phenomena can assist in understanding the impact of these processes on the structure-activity relationship of these materials.

In this work, a nitrogen-doped carbon support labeled as MDC_T (T = temperature of pyrolysis) is synthesized through the pyrolysis of the MOF precursor following a similar procedure described in Chapter 3 under the "Material synthesis" subsection without the use of the active metal (e.g. Fe). This procedure is outlined in **Scheme C.1**.

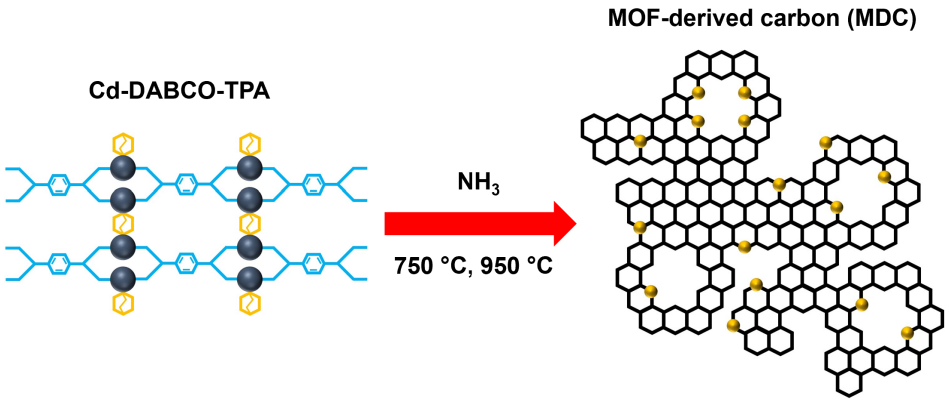

Scheme C.1 Synthetic process towards MOF-derived carbon (MDC) support

In the next phase, an active metal is added, and a second thermal treatment is applied to obtain the final catalyst material. The procedure is follows:

(1) A measured amount of MDC_T was dissolved in a centrifuge tube along with a measured amount of iron nitrate nonahydrate ($Fe(NO_3)_2 \cdot 9H_2O$) in 50 mL of ethanol as the solvent. The amount of $Fe(NO_3)_2 \cdot 9H_2O$ was fixed so that Fe constituted 3 wt. % of the entire mixture.

(2) The mixture was sonicated for a period of 2 hours followed by centrifugation at 9000 rpm for 10 minutes. The solute was then dried at 60 °C under vacuum.

(3) The dried material was then placed within an alumina boat and pyrolyzed at 250 °C under a 5% H_2/Ar gas environment. The temperature ramp was 5 °C min^{-1} and held at 250 °C for 2 hours. The final material was labeled as MDC-Fe_T where T refers to the temperature at which the MDC was synthesized.

Through this process, the formation of metal structures is independent of the formation of carbon from a MOF precursor. **Figure C.1** depict the Raman spectra of both MOF-derived carbon support structures with fittings of the characteristic D and G bands. As shown in **Figure C.2**, the TEM micrographs depict a flaky, carbon for both MDC_{950} (a) and MDC-Fe_{950} (b) following the addition of iron. The PXRD patterns shown in **Figure C.3** indicate a lack of crystalline iron formation. The activity of the MDC-Fe_{950} was shown to be higher than MDC-Fe_{750} (**Figure C.4**) which suggested there are additional phenomena at play unrelated to the metal-centered structures which influence activity.

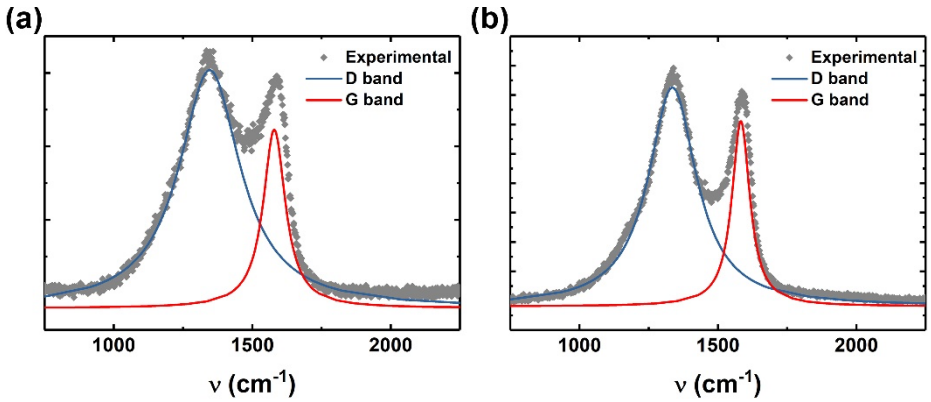

Figure C.1 Raman spectra for (a) MDC-Fe_{750} and (b) MDC-Fe_{950} depicting the D and G bands.

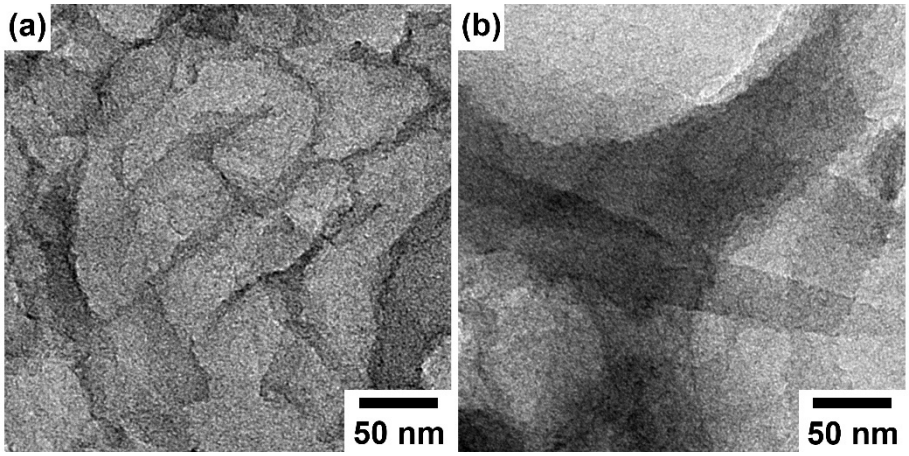

Figure C.2 TEM micrographs of (a) MDC_{950} and (b) MDC-Fe_{950} catalysts.

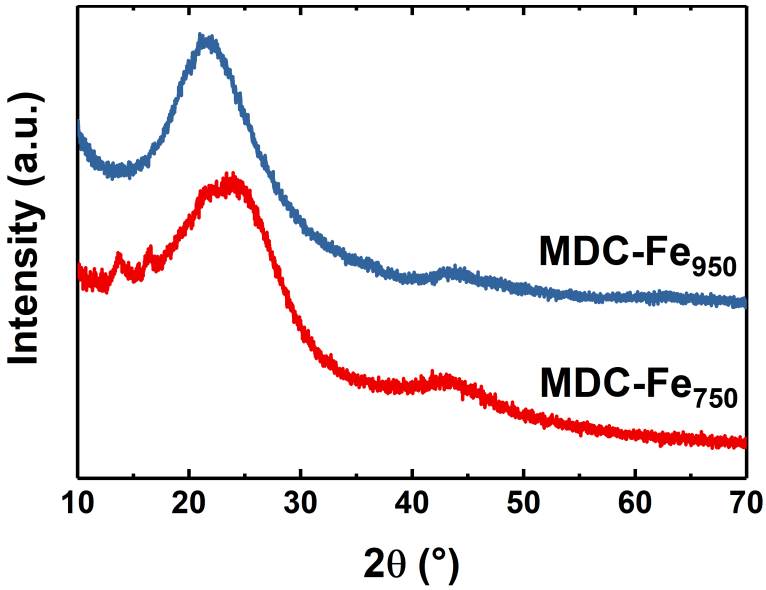

Figure C.3 PXRD patterns of MDC-Fe_{750} and MDC-Fe_{950} showing a lack of crystalline iron structures.

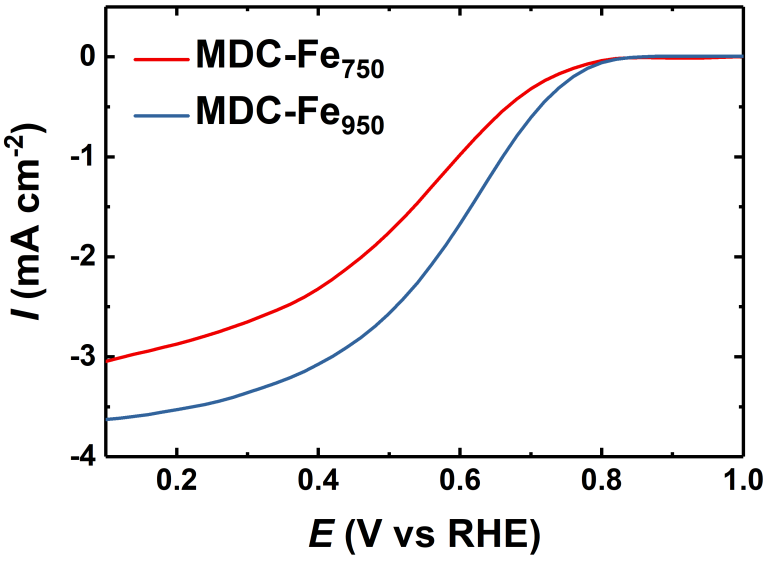

Figure C.4 Staircase voltammograms of MDC-Fe_{750} and MDC-Fe_{950}.

APPENDIX D

Effect of different nitrogen-containing compounds in activity of non-PGM catalysts

One particular strategy which has been shown to increase the activity of non-PGM catalysts is the inclusion of N-containing additives which are hypothesized to increase the quantity of N-coordinated single-atomic transition metal sites. N-heavy compounds including polyvinylpyrrolidone (PVP), phenanthroline, and melamine will be used to further increase the activity of Zn-DABCO-TPA doped with Fe.

Two methods were employed in the addition of N-containing compounds to the MOF structure prior to pyrolysis. The first, known as the ball-milling method involves the physical incorporation of the N-containing compound throughout the MOF framework by the repeated pummeling in a planetary ball-mill followed by flash pyrolysis at 950 °C. The second, referred to as the solvent-method, relies on the use of DMF as a dispersing agent. Both the MOF and N-containing compound are mixed in a 4:1 ratio by mass within 35 mL of DMF and sonicated for 1 hour followed by centrifugation, drying under vacuum at 80 °C then flash pyrolysis at 950 °C. This method differs from the conventional ball-milling method in that it minimizes any damage to the MOF structure that may be incurred through ball-milling; however, this comes at a cost of limiting the surface area coverage of the MOF by the N-containing compound.

Table D.1 Half-wave and onset potentials of non-PGM ORR electrocatalysts made from different N-containing compounds.

MOF precursor	N-containing compound	Structure	Method of addition	$E_{1/2}$ (V vs RHE)	E_{Onset} (V vs RHE)
Zn-Fe-DABCO-TPA	1,10-phenanthroline	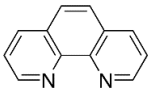	Ball-mill	0.75	0.84
			Solvent	0.75	0.86
Zn-Fe-DABCO-TPA	Polyvinylpyrrolidone	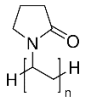	Ball-mill	0.74	0.84
			Solvent	0.64	0.78
Zn-Fe-DABCO-TPA	Melamine	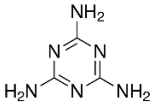	Ball-mill	-	-
			Solvent	0.69	0.84
Zn-Fe-DABCO-TPA	Cyanamide	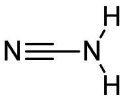	Ball-mill	0.75	0.88
			Solvent	-	-